CHARACTERIZATION OF DAMPING OF MATERIALS AND STRUCTURES AT NANOSTRAIN LEVELS

by

JOSEPH MING-SHIH TING

S.B. Massachusetts Institute of Technology
(1988)

SUBMITTED IN PARTIAL FULFILLMENT OF
THE REQUIREMENTS FOR THE DEGREE OF

MASTER OF SCIENCE
IN AERONAUTICS AND ASTRONAUTICS

at the

MASSACHUSETTS INSTITUTE OF TECHNOLOGY

May 24, 1990

Signature of Author_____
Department of Aeronautics and Astronautics
May 24, 1990

Certified by_____
Professor Edward F. Crawley
Thesis Supervisor

Accepted by_____
Professor Harold Y. Wachman
Chairman, Departmental Graduate Comittee

Aero

CHARACTERIZATION OF DAMPING OF MATERIALS AND STRUCTURES AT NANOSTRAIN LEVELS

by

JOSEPH MING-SHIH TING

Submitted to the Department of Aeronautics and Astronautics on
May 24, 1990
in partial fulfillment of the requirements for the
Degree of Master of Science in Aeronautics and Astonautics

ABSTRACT

An experimental study was performed to characterize material and structural damping over a strain range from 1 nanostrain (nε) to 1000 microstrain (με). Material damping was measured in aluminum rectangular bars and tubes and graphite/epoxy [0] laminated bars and [±15] laminated bars and tubes. Structural damping was measured in a precision three dimensional tetrahedral truss constructed of aluminum struts and joints. Tests to determine critical damping ratios were performed in air at strains from 1 nε to 100 με and in vacuum at strains in the range from 1 με to 1000 με. Damping ratios were obtained from test specimens with a sine sweep approach using piezoceramic strain sensors and piezoceramic proof mass actuators. Results show that material damping is independent of strain at strains below 10 με. Experimental damping measured at small strain levels compared well with thermoelastic models for the aluminum bars and matrix and shear damping models for the [0] graphite/epoxy bars. Material damping shows a dependence on strain at strains above 100 με and can be modeled for metals by the movement of dislocations. Joint dominated structural damping is independent of strain below 1 με and increases with strain above 1 με.

Thesis Supervisor: Dr. Edward F. Crawley

Title: Associate Professor of Aeronautics and Astronautics

ACKNOWLEDGEMENTS

I would like to thank my parents for their love and support. I would also like to thank my advisor, Prof. Crawley, for all of the opportunities he has given me. Finally, I would like to thank a long list of people for not letting me become a totally grump: Carina Hofer, George Pappas (for matching me flame for flame), Paul McGowan (for making my summers at Langley so enjoyable), Alice Lin, the students and faculty of SERC, and my niece Kelley. Well, that wasn't so long after all.

TABLE OF CONTENTS

LIST OF FIGURES

CHAPTER 1

INTRODUCTION

In the quest to learn more about the origin and structure of the universe, an array of increasingly large, precise space based astronomical instruments are envisioned in low earth orbit. In the U.S. program, the current instrument in the optical spectrum is the Hubble Space Telescope (HST). The Hubble Space Telescope and other successor instruments are to be placed in earth orbit to eliminate the light path fluctuations which occur in the atmosphere, and therefore, increase the astronomical capabilities in resolution and imagery.

There are several different types of astronomical instruments being proposed for launch into earth orbit as the successor to the HST -- filled aperture devices, partially filled aperture devices, and interferometric devices. At one end of the spectrum are telescopes such as the HST, filled aperture instruments with a single, continuous collecting surface. At the other end of the spectrum are interferometers. Interferometers can be thought of as discrete telescopes with only a few, sparsely located detectors. The advantage of the interferometer is that the collectors can be located at great distances, bypassing the size limitations of a single optical surface.

There are two major types of interferometers under consideration -- the two collector interferometer and the multiple collector array [Traub and Gursky, 1980]. The two collector instrument measures stellar diameters or stellar separation. The light from the two collectors are combined at a third point where the interference pattern from the two beams is recorded [Hecht, 1987]. The multiple collector array, or correlation interferometer uses the correlation function from the combined signals from several collectors to create an image of a source [Traub and Gursky, 1980].

The basic structure of almost all currently proposed interferometers is essentially the same. Several collectors are connected by a truss structure. An optical delay line, a set of movable mirrors in the light path, is used to compensate for any difference in the arrival time of light at the collectors. The beams from the separate collectors are then brought to a

single focal point using a combining telescope [Traub and Gursky, 1980]. The problem is that the positions of the optical elements must be held stable relative to each other to fractions of a wavelength of light -- on the order of 10 nm.

There are two technical approaches to the achievement of this precise alignment and positioning. One is to reduce and isolate the sources of mechanical disturbance as much as possible and to rely on passive mechanical damping to limit response. Passive damping is due to material damping [Mohr, 1982], structural damping at joints [Crawley et al, 1988], and inclusion of struts and members which include viscous, viscoelastic, or passively tuned piezoelectric elements [Hagood and von Flotow, 1989]. The second approach is to actively control the position of the optical elements [Fanson et al, 1989]. In the active approach, measurements of position are made through metrology optics and distributed strain sensors and fed back to active members and mirror positioning actuators [Morgan et al, 1982]. In both approaches a knowledge of damping establishes limits on the achievable performance. The precise nature of these instruments implies that the amplitudes at which this damping is important is very small -- orders of magnitude smaller than the amplitude at which structural dynamic characterization commonly occurs.

Currently, there is much uncertainty in the aerospace community about the damping of structures at such small vibration levels [Garba, 1988]. One school of thought says that these structures will behave linearly by design and the properties will be constant with strain level. The other school of thought espouses the idea that the mechanisms that normally provide structural damping -- atomic and thermal diffusion, plane slippage, joint friction, etc., will no longer necessarily behave the same at very small strains. This uncertainty has led to an effort to study the behavior of structures at nanometer levels of motion.

Normally, experimental measurement of damping is done at moderate strain levels. The range from 10 to 1000 microstrain ($\mu\varepsilon$), is typical of structural dynamic testing, the lower limit being set by the noise floor of conventional instrumentation and the upper limit being set by concern for buckling or plastic deformation. However, for the problem of optical interferometry, the strains at which damping will be important are

down to the order of one nanostrain (nε). The need to understand structural damping, combined with the uncertainty in the previous knowledge of damping at extremely small strain levels, creates the need for a test program to examine damping over a wide range of strains.

The objective of the research presented here is to characterize the damping of materials and structures from nanostrain levels to hundreds of microstrain. To do this, specimens of typical spacecraft materials and prototypical space structural truss hardware were tested. The test results are used to determine whether there are any changes in material and structural damping over this strain range. A study of a third source of damping, due to supplementary damping enhancement treatments, was beyond the scope of this study.

Previous measurements of damping have been made using several approaches. Some of the earliest measurements of the internal damping of brass, aluminum, iron, and other metals, by Ke and other researchers, were made using a free decay technique [Zener, 1948]. Damping was obtained from the logarithmic decrement of the free decay of vibrations of wires or bars. Since then there have been many studies of the damping of materials using this free decay approach. One notable one was a study performed by Mohr, who measured the damping of aluminum and graphite epoxy. Damping was obtained by studying the decay of vibrations of bars in free-fall by lofting bars in a vacuum chamber [Crawley et al, 1983].

Another technique used to measure damping is the sine sweep or half-power bandwidth technique. The sine sweep technique involves the excitation of a specimen over a range of frequencies around resonance to determine the points at which the energy in the structure is one half of the peak energy at resonance. The damping of a mode of the structure can then be determined from the spacing of the half power points. This approach has been used by many researchers. Zener studied the damping of body and face centered cubic metals and developed a thermoelastic model of for the damping of metals [Zener, 1948]. Granick and Stern measured the internal damping of aluminum bars [Granick and Stern, 1965]. Lesieutre [1989] and also VanSchoor [Crawley and van Schoor, 1987] made measurements of the damping of metal matrix composites. In the area of

non-material damping, Sigler [Crawley et al, 1988] measured the structural damping of truss structures due to the presence of erectable joints.

All of the measurements of damping discussed above were made at strain levels above 10 με. Characterizing damping at nanostrain levels presented the challenge of measuring nanostrain vibrations. Techniques for doing this have been developed in the field of gravity wave detection [Michelson et al, 1987]. Gravity wave detection involves the use of a large, supercooled aluminum bar which acts as an extremely sensitive antenna. The very weak gravity waves excite structural modes of the bar at exceedingly low, strain amplitude levels.

One of the oldest methods of measuring strains in gravity wave antennas involves the use of a piezoelectric crystal, which produces a voltage proportional to the strain in the crystal [Braginsky et al, 1985]. The signal from the crystal, which is attached to the antenna, is then amplified and measured. This method was adapted for use in the current study for the measurement of strains in the material damping and structural damping test articles.

Using these measurement techniques, values of material damping were obtained for bars and tubes fabricated from aluminum and graphite/epoxy. The material damping specimens, discussed in Chapter 2, were constructed with different lengths to permit the study of damping over a wide range of frequencies. Values of structural damping were obtained by testing a tetrahedral space truss. The truss, part of a testbed in the Space Engineering Research Center (SERC) was designed to model the behavior of an optical interferometric telescope. Three and one half meters on a side, the six arm tetrahedral truss was constructed from aluminum tubes with tight joints.

Testing, discussed in Chapter 3 was performed in two stages -- one to study damping behavior of the material damping specimens and a second to study structural damping behavior of the truss. A sine sweep method was used to obtain damping -- test articles were shaken and their responses were obtained at different frequencies and different amplitudes from 1 nε to 1000 με using piezoelectric sensors.

Results, discussed in Chapter 4 were compared with analytical models where available. In particular, the process was verified by comparing the damping of aluminum bars with the thermoelastic predictions for metal bars [Nowick and Berry, 1972]. Once validated, the measurements on the aluminum tubes and graphite/epoxy specimens were made by repeating the test procedure used for the aluminum bars.

Next, the jointed interferometer testbed truss was tested. The damping of several modes of the truss was obtained. By comparing the results with those from the material damping specimens, the damping due to the joints could be determined.

Of particular interest were changes in damping as a function of strain level. Losses at very low strain levels were compared with results at higher levels. Observations of any of dependence of damping on amplitude, either gradual or abrupt changes, were noted. Conclusions, discussed in Chapter 5, were drawn from these observations.

CHAPTER 2

TEST SPECIMENS

Testing was performed in two phases to identify and separate the contributions of material damping and structural damping. Accordingly, there were two sets of test specimens -- first a set of simple bars and tubes to examine material damping characteristics, and secondly the interferometer testbed to examine structural damping characteristics. In this chapter, the design and construction of both sets of test specimens is discussed.

2.1 Material Damping Test Specimens

There were two requirements in the design of the material damping test specimens. First, the test articles had to reflect materials and geometries of realistic aerospace hardware. Second, the specimens had to be designed to allow a parametric study of damping. The materials used were 6061-T6 aluminum and AS4/3501-6 graphite/epoxy. To study pure material damping in a simple geometry, rectangular cross section bars were constructed of aluminum and graphite epoxy. To study material damping in a slightly more complex form, tubes of aluminum and graphite/epoxy were also constructed. The measured dimensions and frequencies of the material damping test specimens are given in Table 2.1.

Table 2.1 Material Damping Test Specimens

Material/ Geometry	Length (m)	Width/Diameter (mm)	Thickness/Wall Thickness (mm)	Freqs. Tested (Hz)
Al/bar	1.7	26	3.2	6.17, 17.1
Al/bar	1.3	26	3.2	9.34, 25.8, 50.6
Al/bar	0.9	25	3.3	19.4
Al/bar	0.5	23	3.2	58.1, 174
Al/tube	0.9	25	1.7	185, 510
Al/tube	0.7	25	1.7	302, 837
Gr/Ep $[\pm 15]_{6s}$/bar	0.9	25	3.2	33.2, 90.8, 288
Gr/Ep $[\pm 15]_{6s}$/bar	0.7	26	3.1	53.1, 145
Gr/Ep $[0]_{24}$/bar	0.9	30	2.7	30.9, 83.5
Gr/Ep $[0]_{24}$/bar	0.7	25	3.0	56.9, 157
Gr/Ep $[\pm 15]_{3s}$/tube	0.9	25	1.7	275
Gr/Ep $[\pm 15]_{3s}$/tube	0.68	25	1.8	503

The simplest articles studied were the set of aluminum bars, designed with a 25 mm x 3.2 mm rectangular cross section. This simple geometry was chosen because thermoelastic models of the damping of a simple rectangular bar existed, and a comparison could be made between the predictions from these models and previous experimental results [Crawley et al, 1983]. The models were based on work done by Zener to model the damping of body-centered cubic and face-centered cubic metals [Zener, 1948]. A 25 mm x 3.2 mm cross section was chosen for several reasons -- availability of aluminum stock in that size and previous work with bars of similar size [Sarver and Crawley, 1987]. Bars of aluminum from the same lot with a 25 mm x 3.2 mm cross section were cut into four different length bars -- 0.5 m, 0.9 m, 1.3 m, and 1.7 m long. The dimensions of the bars were picked so that tests could be performed over a range of frequencies below and above the Zener relaxation frequency given by,

$$\omega_r = \frac{h^2 C \rho}{\pi^2 k}$$

where h is the thickness of the specimen, C the specific heat per mass, ρ the material density, and k the thermal conductivity [Zener, 1948].

This expression holds only for bars with simple rectangular geometries. The reason for this is partially revealed by the dependence of the relaxation frequency on the thermal coefficients and thickness of the material. When one surface of a bar is in compression and the opposite surface is in tension, as is the case in transverse vibration, thermal gradients arise [Braginsky et al, 1985]. In aluminum, this condition causes the conversion of vibrational energy to heat. For simple rectangular bars, the gradients are linear and heat flows from one face to the other. The thicker the bar, the longer the time for heat to move from face to face. By matching the period of mechanical vibration to the characteristic time of heat flow, the energy loss can be maximized. For more complicated geometries, the heat no longer flows simply across the structure and the Zener model is no longer applicable.

In order to study the damping of a well documented material, but in a more typical geometry, aluminum tubes were tested. The damping in tubes in flexure is less well understood than the damping in bars. Two tubes, 0.7 m and 0.9 m long with 25 mm outer diameters (O.D.) and 1.6 mm

wall thicknesses (W.T.) were cut from a single piece of aluminum tubing to minimize the differences in the material properties in the construction of the aluminum tubes. The dimensions of the tubes were chosen to match those of the bars -- the 25 mm O.D. and 1.6 mm W.T. gave the same width and total wall thickness as the aluminum bars.

The other material included in the study was AS4/3501-6 graphite/epoxy, an advanced composite material commonly used in the aerospace industry. Graphite/epoxy (Gr/Ep) was chosen because it is a material being considered in the construction of space based astronomical structures [Morgan et al, 1982]. In addition to its high strength to weight ratio, Gr/Ep structures can be constructed to have a coefficient of thermal expansion of zero by changing the angle of the layup [Jones, 1975]. Because of the range of temperatures over which space structures operate, minimizing thermal distortion can be critical to the performance of optical instruments with precision pointing requirements.

To test the graphite/epoxy material in a layup which might be used in such astronomical devices, the graphite/epoxy specimens were designed to have a coefficient of thermal expansion, α, close to zero. Rectangular cross section bars were constructed first. Twenty four plies of AS4/3501-6 prepreg were laid up in a $[\pm 15]_{6s}$ layup to form a plate 3.2 mm thick, the same thickness as the aluminum bars, but with an α of 3.71×10^{-8}. The laminate was then processed using a standard AS4/3501-6 graphite/epoxy cure and postcure cycle [Lagace et al, 1988]. After being cured, the plate was cut into several 25 mm x 3.2 mm bars, 0.9 m and 0.7 m long. The length of the bars was limited by the size of the composite autoclave facilities. The nominal dimensions of the bars were chosen to overlap the dimensions and frequencies of the aluminum bars as much as possible.

To determine the effect on damping of the change in the angle of the plies, several rectangular cross section bars with a uniply layup, $[0]_{24}$ were also fabricated. The uniply plate from which the bars were cut was laid up and cured at the same time as the $[\pm 15]_{6s}$ plate. The uniply plate was then cut into several bars, 0.9 m and 0.7 m long, each with the same nominal cross section as the zero CTE bars -- 25 mm x 3.2 mm. Any differences in damping behavior between the zero CTE bars and the uniply bars could then be attributed to layup only.

The next step in the study was to construct and test two graphite/epoxy tubes which were designed to reflect more closely, the requirements of a possible space based optical instrument. The two tubes, 0.9 m and 0.68 m long with a 25 mm nominal O.D. and 1.6 mm wall, were designed to have a zero CTE. To achieve this, the tubes were constructed using a zero CTE layup, $[\pm 15]_{3S}$, similar to that used in the zero CTE bars. Each tube was laid up by wrapping strips of AS4/3501-6 prepreg tape around an aluminum mandrel. A layer of shrink tape was used to squeeze excess epoxy out of the tube during the cure. The shrink tape left slight indentations in the surface of the tubes 0.1 mm deep. After a standard cure, the tubes were removed from the mandrels and cut to 0.9 m and 0.68 m lengths.

2.2 Structural Damping Test Specimen

The second part of the testing involved structural damping tests of a model of an interferometric truss, part of a testbed developed at M.I.T. in the Space Engineering Research Center (SERC). Designed and constructed by a team of M.I.T. faculty and students, the testbed was the culmination of a year of work. The goal of this testbed was to model the behavior of a space based interferometer for the development of schemes and hardware for control of the shape of the structure to nanostrain levels.

As the result of an initial study, several major constraints were imposed on the design of the testbed. First, available space in the lab, a room 3.8 m high, imposed size constraints. Second, computation speed of commercially available control and data acquisition hardware presented an upper limit on the global frequencies of the testbed. In addition, the frequencies of the first global modes to be controlled had to be ten times higher than the local strut modes. This spacing allowed control of the well separated global modes, while avoiding the local modes of the struts. Third, the struts had to be easily removable to allow insertion of struts with sensors, passive dampers, or actuators.

The essential form of the testbed was the tetrahedral truss, 3.5 m on a side as shown in Figure 2.1. In order to reflect the dynamics of a realistic space-based interferometer, the truss was designed not to have joint dominated dynamics [Garba, 1988], that is, to have tight, linear joints. The

six legs of the truss were identical, consisting of 14 bays of truss, each 0.25 m long (Fig. 2.2). Because of the geometry of the truss layup, two different strut lengths were required: 0.25 m and 0.16 m. Each strut had an outer diameter of 9.5 mm or 3/8 inch and a wall thickness of 1.5 mm. Each node had a 30 mm diameter and had 18 10/32 threaded holes. Both the nodes and the struts were constructed of 6061-T6 aluminum. To connect the nodes to the struts, B nuts were added to the 3/8-24 threaded ends of the struts (Fig. 2.3). The B nuts were hollow caps with female 3/8-24 threads and clearance holes in the ends for 10/32 bolts. The purpose of the B nuts was to allow quick and easy connection to the 18 hole, 30 mm O.D. nodes.

To set a strut into a bay, a 1/2" 10/32 Allen Cap bolt was screwed into a node after having been inserted through the clearance hole in a B nut. The free end of the cap bolt was secured to the node with two 10/32 nuts and "Loctite". After repeating this on an opposing node, the strut was inserted between the nodes and the two B nuts were screwed to the ends of the strut.

Due to the symmetric geometry of the truss, the lowest global modes are clustered in two frequency ranges. A list of the frequencies of the first six bending modes, modes 7 through 12 of the truss, from a normal modes finite element analysis [Lublin, 1990] of a continuum beam ADINA model, is given in Table 2.2. Figure 2.4 shows the the corresponding mode shapes. The first bending modes, dominated by the first bending modes of the legs of the truss are clustered between 38 and 58 Hz and the second bending modes, dominated by second bending modes of the legs, are clustered between 94 and 195 Hz. Placing an upper limit on the control bandwidth, the first bending mode of the longest struts is around 370 Hz. The first six modes, not shown, are rigid body modes with no bending of the arms.

Table 2.2 First Six Global Bending Modes From ADINA Continuum Beam Finite Element Model

Mode	Frequency (Hz)
7	38.070
8	38.070
9	39.520
10	39.520
11	40.940
12	47.240

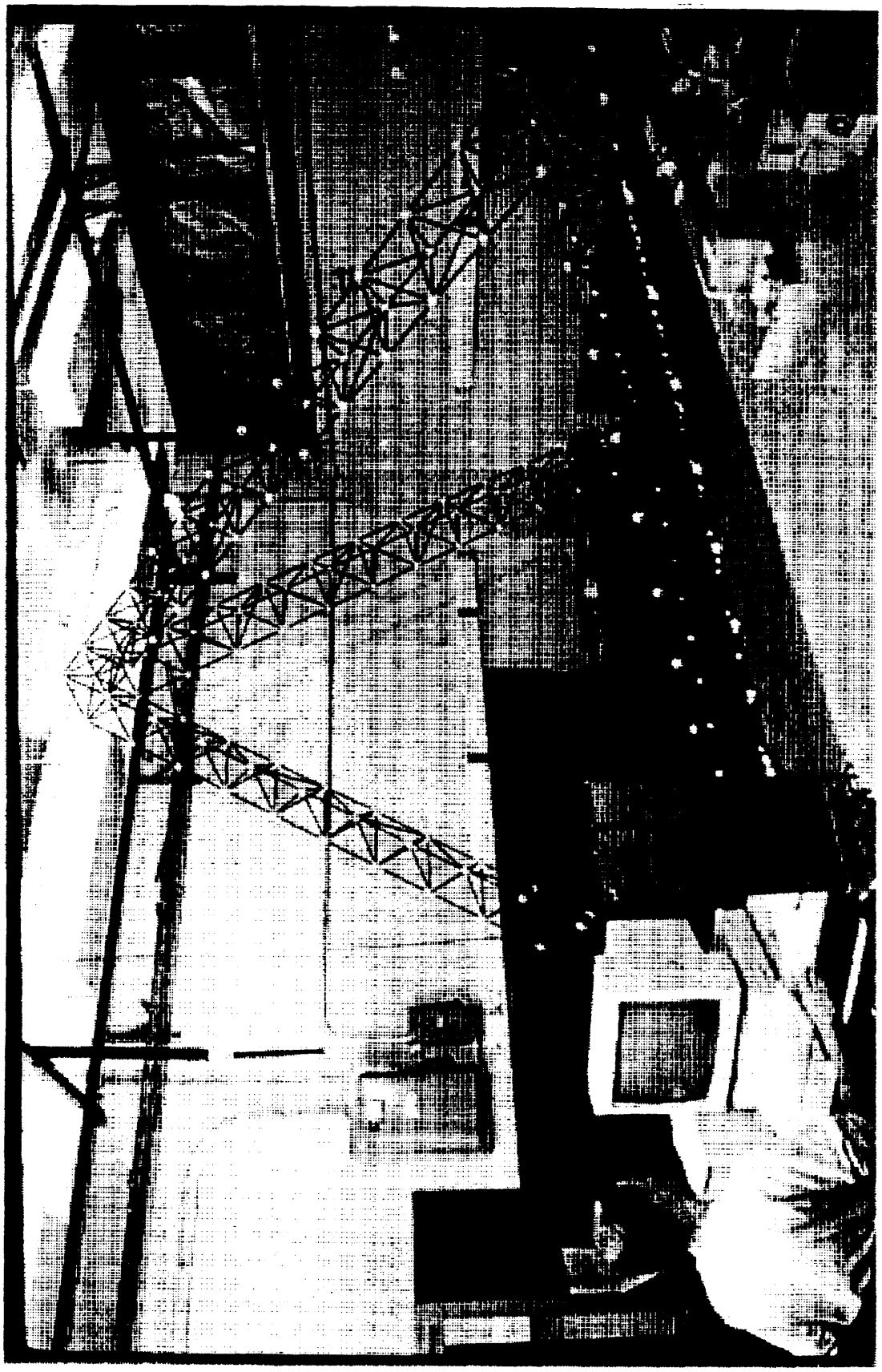

Figure 2.1 Interferometer Testbed

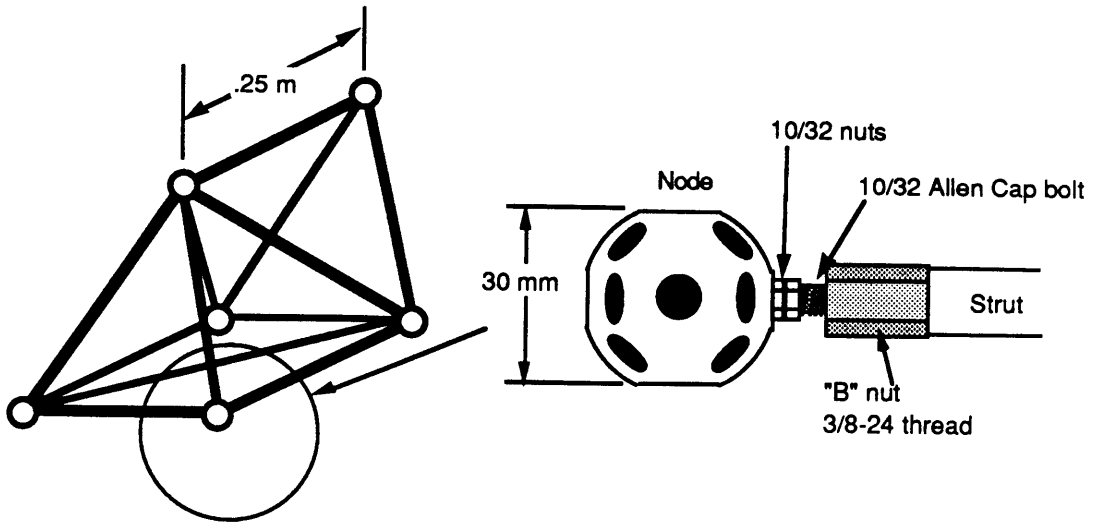

Figure 2.2 One Bay of Tetrahedral Truss With a Closeup of a Joint

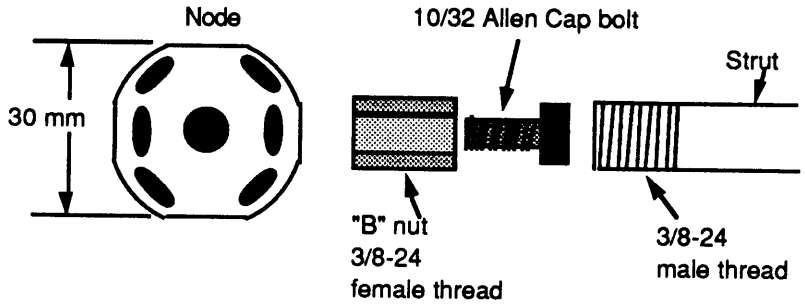

Figure 2.3 Connection of a Truss Strut to a Node

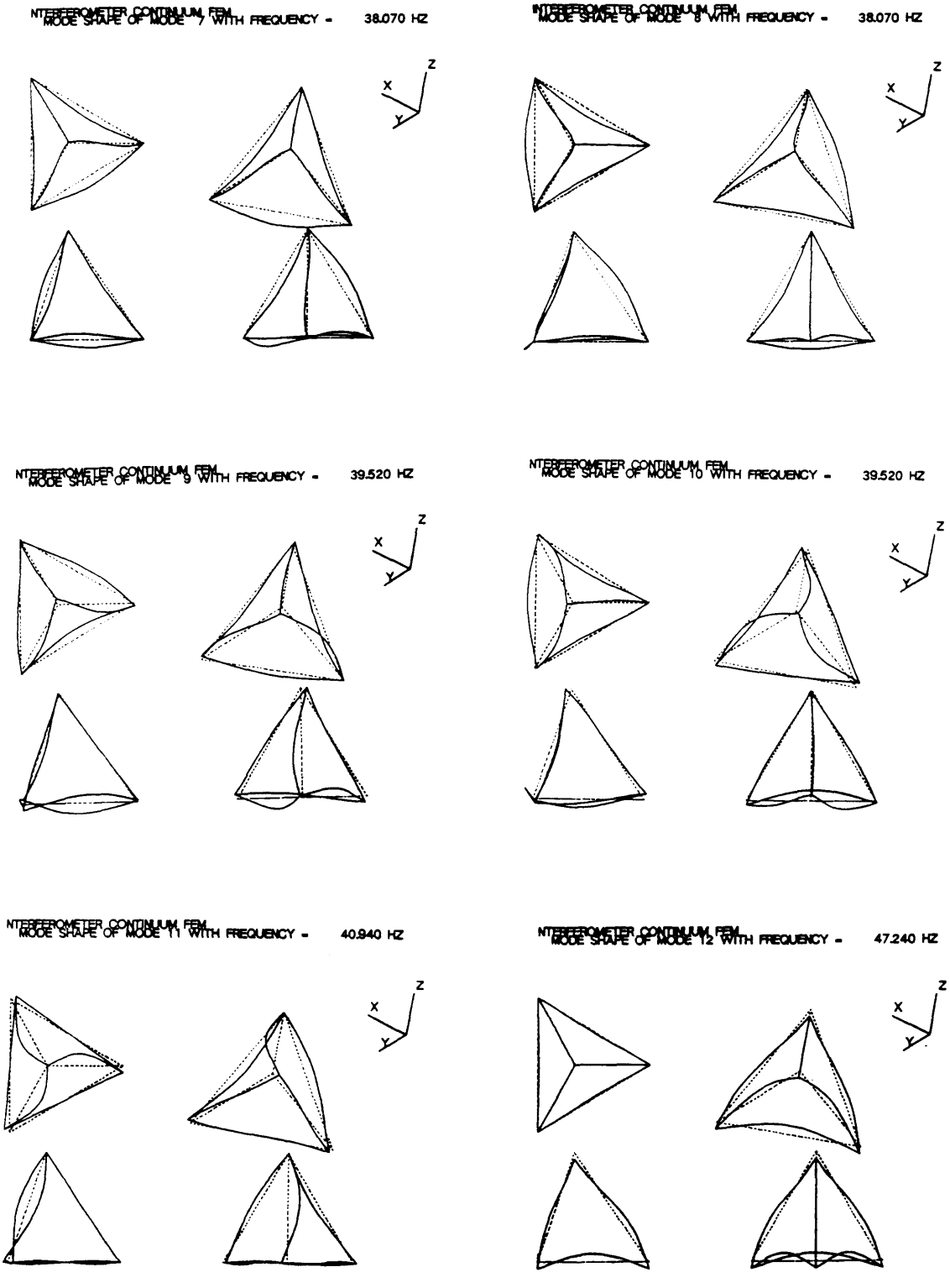

Figure 2.4 First Six Global Bending Modes From ADINA Continuum Finite Element Model

CHAPTER 3

INSTRUMENTATION AND TEST PROCEDURE

An identical procedure was used in the testing of the material damping specimens and the interferometer testbed. First, the test specimens were instrumented with piezoceramic strain gauges to sense vibrations, and with piezoceramic bending motors to actuate vibrations. A block diagram of the apparatus and instrumentation is shown in Figure 3.1. The material damping specimens were then hung inside the ASTROVAC vacuum chamber. After calibrating the piezoceramic strain gauges against adjacent resistive strain gauges, the specimens were tested to obtain damping using a sine sweep approach.

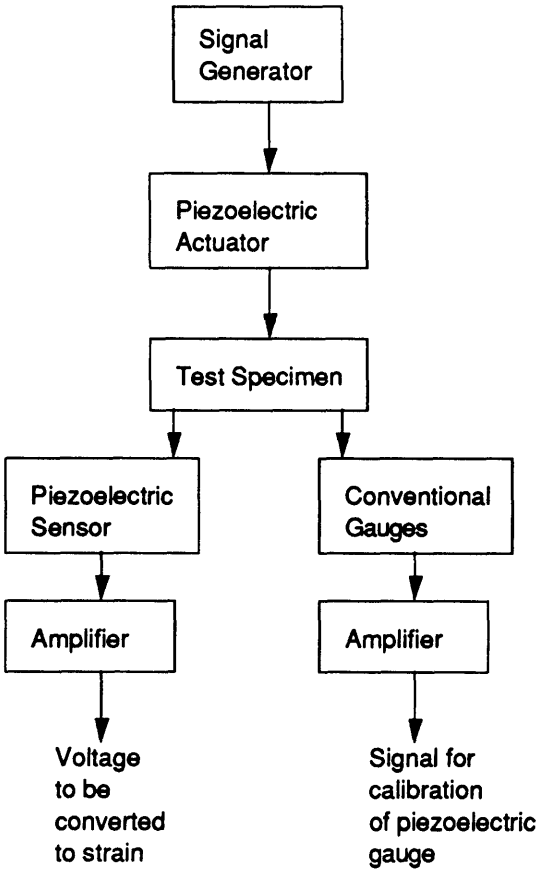

Figure 3.1 Block Diagram of Test Instrumentation

In this chapter, the development of the piezoceramic sensors and actuators used to measure nanostrain vibrations as well as the testing procedure is discussed. Section 3.1 contains the details of the development, calibration, and use of the piezoceramic strain sensors. In Section 3.2, the development and use of the piezoceramic actuators is presented. Finally, in Section 3.3, the procedure and methodology used to obtain damping is discussed.

3.1 Sensors

As discussed in Chapter 1, one of the objectives of the interferometer testbed was control of relative positions of points on the structure to 10 nm in the presence of the ambient mechanical, acoustical, and electrical noise in the laboratory. For a 3.5 m structure such as the testbed, a 10 nm displacement corresponds roughly to a strain of 3 nε. This control objective was used to define the minimum resolution requirement for the strain sensors used in this study -- the sensors had to be able to resolve strains or provide measurements from which strains could be inferred down to 1 nε. In addition, because of the small damping ratios characteristic of material damping, the sensors had to have a minimal effect on the dynamics of the material damping test specimens. With these requirements, several types of sensors, listed in Table 3.1, were considered.

Several sensors met the resolution requirement, but were eliminated from consideration for other reasons. Of the optical devices, the laser interferometer, used to measure displacements of the interferometer testbed, had sufficient resolution, but could not be used on the material damping specimens because of the size of the optical elements which had to placed on each measurement point. The laser Doppler velocimeter, whose output had to be integrated to obtain strain had sufficient resolution down to 10 nε, was found to be too sensitive to residual rigid body motions. Conventional resistive strain gauges measured strain directly, but were found in tests to be limited to strains above 100 nε because of amplifier noise. Semi-conductor strain gauges had resolution to only 10 nε, and were sensitive to temperature fluctuations. Small piezoelectric accelerometers were found to be limited to inferred strains above 100 nε. More sensitive servo accelerometers had sufficient resolution, but only over a narrow

bandwidth and were too massive to be mounted on the material damping test specimens. The only sensors found to meet the minimum requirements were the gauges constructed from piezoelectric ceramic and polymer materials. Because of their higher d31 electro-mechanical coupling coefficient, the gauges constructed from the piezoelectric ceramic material were chosen over the piezoelectric polymer gauges.

Table 3.1 List of Sensors Considered

Sensor	Advantage	Disadvantage
Laser interferometer	Resolution to ~ 1 nε	Size of required optical components
Laser Doppler velocimeter	Non-contacting, resolution inferred to 10 nε by integrating velocity	Sensitivity to rigid body motion
Piezoelectric accelerometer	Ease of placement and use	Resolution inferred to .1 με by integrating acceleration, limited by amplifier noise
Servo accelerometer	High resolution	Bandwidth limited to below 100 Hz, large size
Resistive strain gauge	Strain measured directly	Resolution to 100 nε, limited by amplifier noise
Semi-conductive strain gauge	Resolution to 10 nε	High temperature sensitivity
Piezoelectric polymer film strain gauge	High sensitivity, $d31=21 \times 10^{-12}$ m/V	Need for calibration of gauge
Piezoelectric ceramic strain gauge	High sensitivity, $d31=120 \times 10^{-12}$ m/V, resolution to 10 pε	Need for calibration of gauge

Unlike the gauge element of a resistive or foil strain gauge, which experiences a change in resistance with strain [Measurements Group, Inc., 1988], piezoceramics produce a voltage proportional to strain [Braginsky, 1985]. The sensitivity of a typical piezoceramic material is at least one thousand times greater than that of a foil strain gauge [Forward, 1980]. A typical piezoceramic gauge used in this investigation was the 0.25 mm x 6.5 mm x 12.7 mm gauge constructed with a G-1195 piezoceramic produced by Piezo Systems. G-1195, a common piezoelectric material was chosen because of its high voltage-strain constant. This piezoelectric gauge produced an unamplified signal of 105.2 mV/με. This sensitivity can be compared with the sensitivity of the two calibrating foil strain gauges on the same bar. The CEA-13-125UN-120 resistive gauges from Measurements Group, Inc., with a gauge factor of 2.11, were wired in a half bridge arrangement and were driven with a 4 V excitation. The

output voltage was amplified using a Measurements Group, Inc. strain gauge amplifier with a gain setting of 2000, the maximum possible setting on the amplifier. For this gauge factor and gain, the equivalent sensitivity of the resistive gauges was 6.42 mV/με. Thus, the ratio of sensitivities of the piezoelectric gauge to the resistive foil gauge is 32000 before amplification and 16 at maximum strain gauge amplification.

One of the disadvantages of the piezoceramic gauges was the need to determine the exact value of the electro-mechanical strain coefficient, or calibration factor, for each strain gauge. To find the calibration factors, the piezoceramic gauges were calibrated against standard resistive strain gauges at moderately large strain levels, in the range 0.1 με to 100 με. The voltage output to strain relation was then extrapolated down to 1 nε. Previous work has shown that the strain-voltage relation for piezoceramic materials is linear to at least 10 pε [Forward, 1980].

A summary of the dimensions and placement of the gauges is given in Table 3.2. To instrument the aluminum bars, a sheet of G-1195 piezoceramic material, 0.25 mm thick coated with a nickel electrode was cut into a set of 12.7 mm x 6.4 mm gauges. As shown in Figures 3.2 and 3.3, the gauges were bonded directly to the aluminum bars, arbitrarily placed 6.4 mm from the edge of the bar and 0.038 m off-center -- with the resulting x/l ranging from 0.424 to 0.478. This placement off-center in x allowed for detection of both odd and even modes. The resistive foil strain gauges used for calibration were placed opposite the piezoelectric gauges (Fig 3.2). In order to achieve good point to point contact, cyanoacrylate epoxy was used to bond the piezoelectric gauges to the test specimens. Bonding directly to each aluminum specimen allowed electrical access to the bottom electrode of each piezoceramic gauge so that grounding the structure also grounded the bottom face of the piezoceramic. To minimize the physical effects on the structure, electrical connections were made using a pair of 36 gauge twisted copper magnet wire.

Table 3.2 Summary of Dimensions and Placement of Sensors

Specimen	Nominal gauge dimensions (mm)	Position of gauge from end, x (m)	Normalized position of gauge, x/l
1.7 m Al bar	6.4 x 12.7	0.812	0.478
1.3 m Al bar	6.4 x 12.7	0.612	0.471
0.9 m Al bar	6.4 x 12.7	0.412	0.458
0.5 m Al bar	6.4 x 12.7	0.212	0.424
0.9 m Al tube	3.2 x 12.7	0.279	0.310
0.7 m Al tube	3.2 x 12.7	0.217	0.310
0.9 m Uniply Gr/Ep bar	6.4 x 12.7	0.279	0.310
0.7 m Uniply Gr/Ep bar	6.4 x 12.7	0.217	0.310
0.9 m [±15]6s Gr/Ep bar	6.4 x 12.7	0.279	0.310
0.7 m [±15]6s Gr/Ep bar	6.4 x 12.7	0.217	0.310
0.9 m Gr/Ep tube	3.2 x 12.7	0.45	0.500
0.68 m Gr/Ep tube	3.2 x 12.7	0.34	0.500
Interferometer testbed	3.2 x 12.7	------	-------

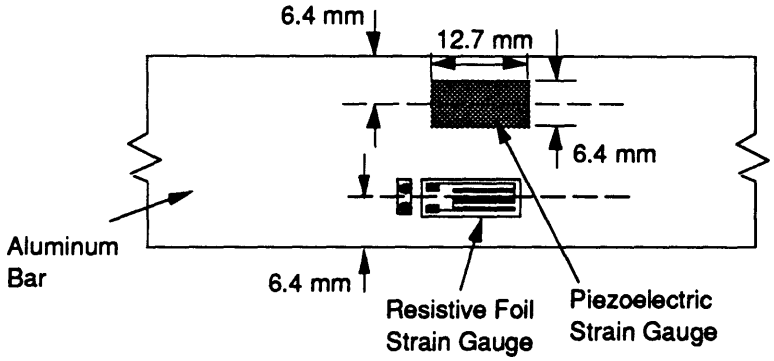

Figure 3.2 Instrumentation of the Aluminum Bars

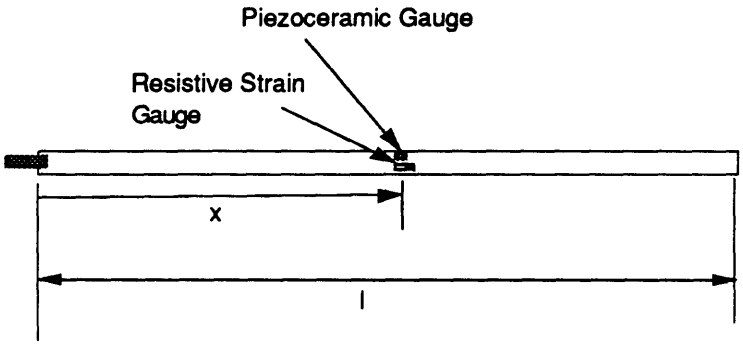

Figure 3.3 Placement of Piezoceramic Gauges on Aluminum Bars

Instrumentation of the graphite/epoxy bars was performed in a slightly different manner, as shown in Figure 3.4. The gauges used were the same size as those used on the aluminum bars, 12.7 mm x 6.4 mm. However, as shown in Table 3.2, the gauges were placed at the point of maximum second mode strain, x/l = 0.310. Since the graphite/epoxy material was non-conducting, a piece of 0.025 mm brass shim was bonded between the gauge and the bars. Contact with the bottom electrode of the gauge was made with the small tab on the shim.

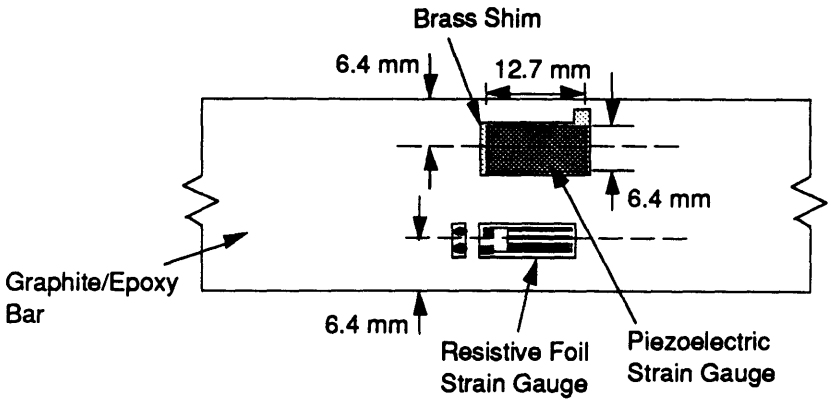

Figure 3.4 Instrumentation of the Gr/Ep Bars

Because the piezoceramic material used for the gauges was flat and brittle, the gauges could not be bonded to the curved surface of the aluminum tubes. In order to attach the gauges, a flat area, shown in Figure 3.5, which measured 64 mm long, 6.4 mm wide, and 0.41 mm deep, centered at x/l = 0.310 was milled into the surface of each aluminum tube. To reduce the modifications to the tubes, a smaller, 12.7 mm x 3.2 mm piezoelectric gauge was used. Each piezoelectric gauge was bonded to each flat with cyanoacrylate epoxy. Two calibrating resistive strain gauges were placed on either side of the piezoceramic on the flat. The foil gauges were wired in two half-bridges with two strain gauges placed on the opposite side of the tube. Because of defects of asymmetry in the circular geometry, the direction of the bending axes of the modes of the tubes could not be determined *a priori* and there was no guarantee that the piezoelectric gauges were placed at the point of circumferential maximum strain. As shown in Figure 3.5, in the event of possible misplacement of the piezoelectric gauges, a second set of resistive gauges was placed 90° away. The information from the two sets of gauges 90° apart could be combined to find the orientation of the bending axis of each mode of each tube. Corrections could then be made in the measurements from each piezoelectric gauge to infer the maximum strain in the tube as a function of the strain measured at the piezoelectric gauge.

Instrumentation of the $[\pm 15]_{3S}$ graphite/epoxy tubes was performed in a similar way, with two changes due to the nature of the graphite/epoxy laminate (Fig. 3.6). Damage to the load carrying graphite fibers was reduced by milling a smaller flat, only 16 mm x 4.8 mm x 0.23 mm. As with the Gr/Ep bars, a piece of 0.025 mm thick brass shim was placed

beneath each piezoelectric gauge. Because of the smaller flat, the two adjacent calibrating gauge bridges were placed on the surface of the tube instead of on the flat. A second set of gauges were placed at 90° from the flat.

Instrumentation of the testbed was also performed with piezoceramic gauges (Fig. 3.7). One strut was modified using the same approach used to instrument the tube specimens. A flat, 16 mm x 4.8 mm was milled into the surface of the strut. A piece of piezoceramic material, 12.7 mm x 3.2 mm was bonded to the flat using cyanoacrylate epoxy. To calibrate the piezoceramic gauge, four foil strain gauges were bonded next to the flat and wired in a full bridge arrangement. The instrumented strut was then placed in one leg of the testbed (Fig. 3.8). In order to measure the damping in the first family of global modes of the structure, the strut was placed in a bay near the point of assumed maximum strain for this family of modes.

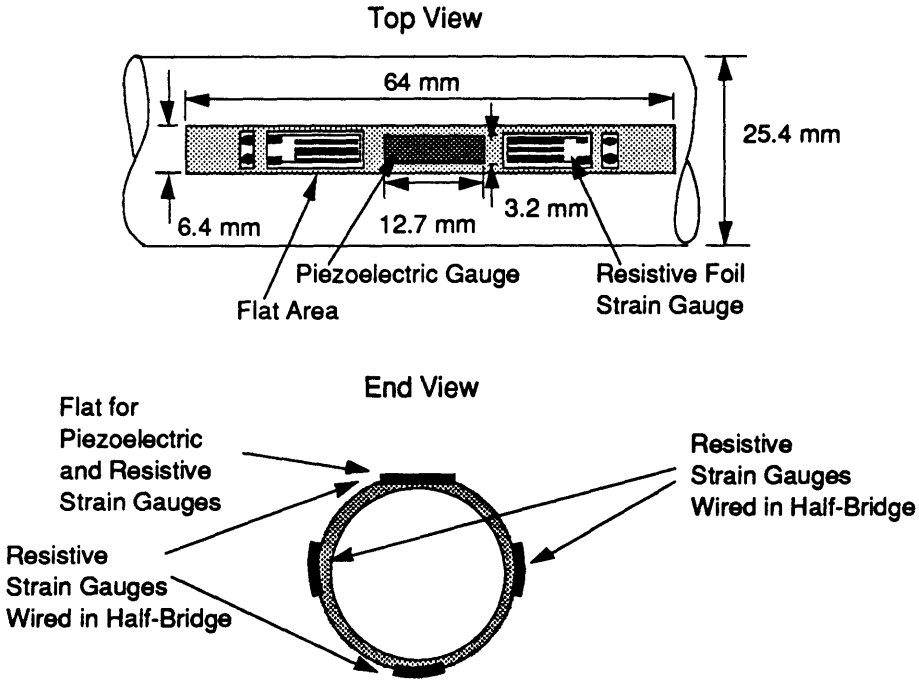

Figure 3.5 Instrumentation of the Aluminum Tubes

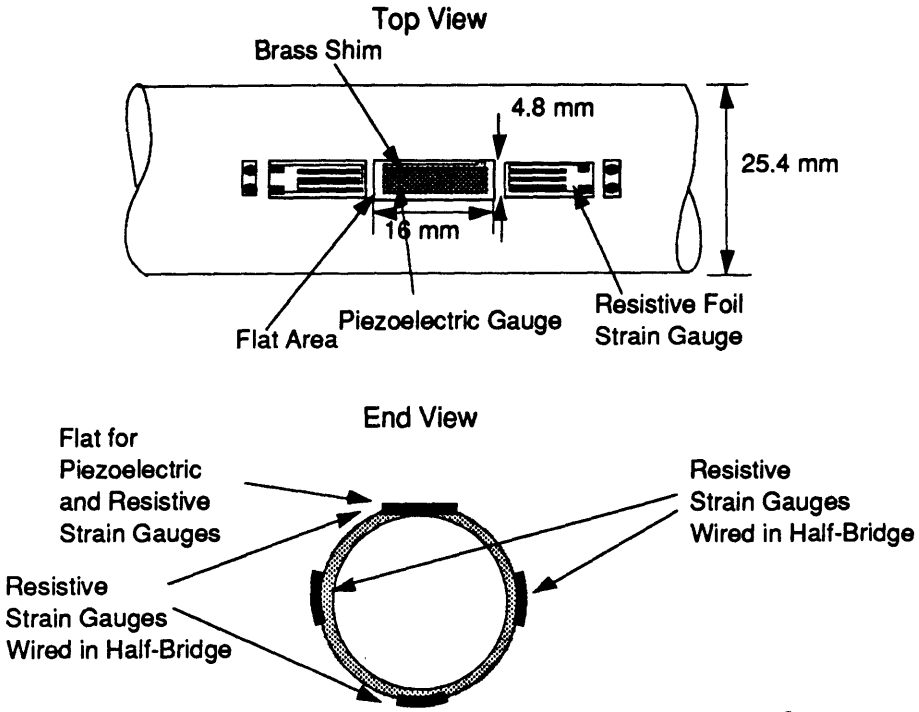

Figure 3.6 Instrumentation of the Graphite/Epoxy Tubes

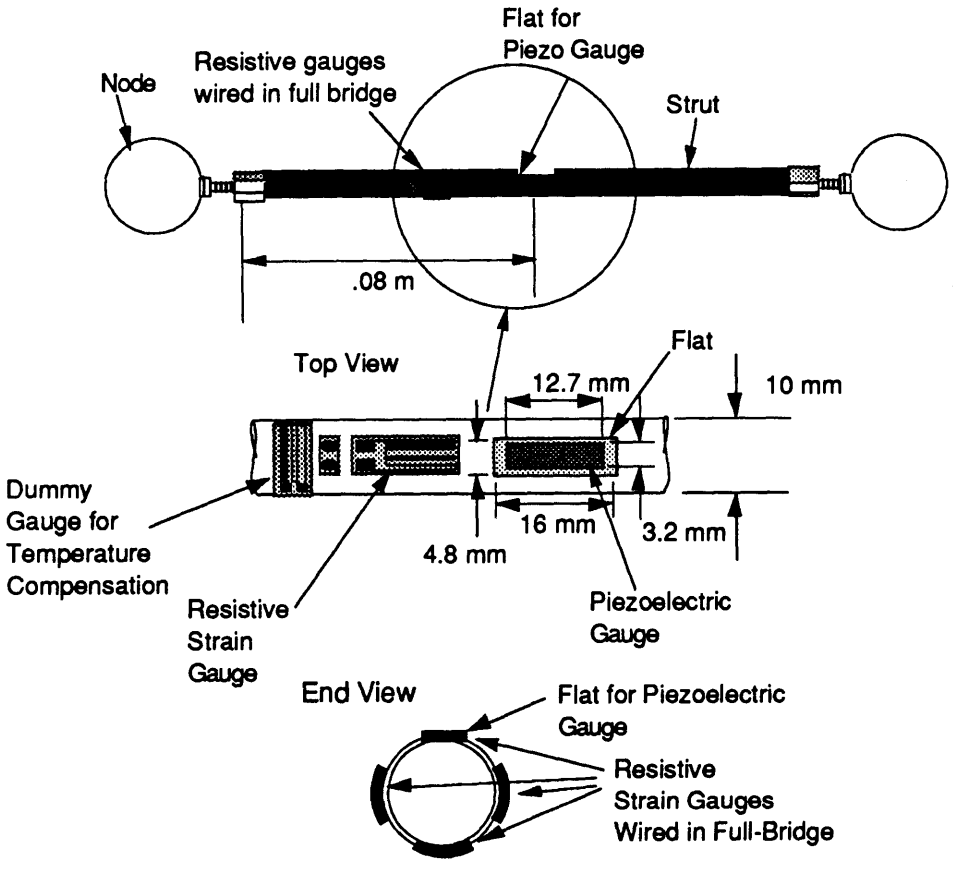

Figure 3.7 Instrumentation of Truss Strut

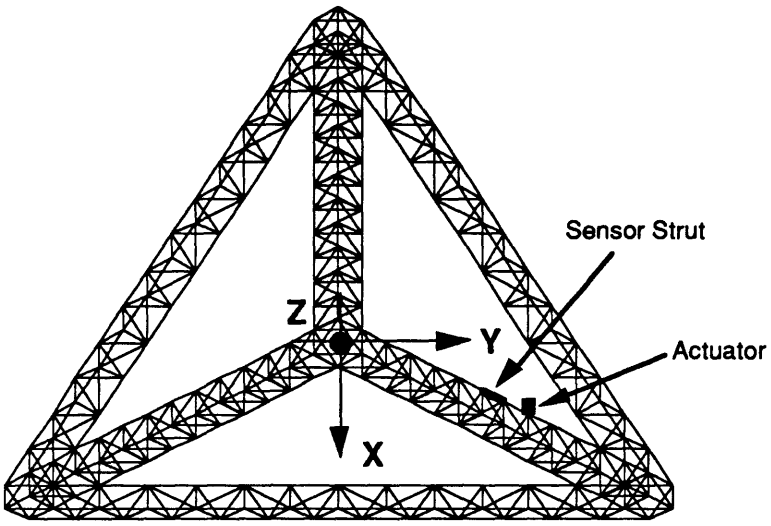

Figure 3.8 Placement of Interferometer Testbed Sensor Strut and Actuator (Center Vertex of Testbed Out of Plane)

Figure 3.9 presents a schematic of the signal conditioning used during the calibration of the strain gauges. The signal from each piezoceramic gauge was amplified using a 5210 Princeton Applied Research (PAR) two phase lock-in amplifier. This lock-in amplifier effectively amplified the signal with an adjustable gain over a narrow notch around a reference frequency set by a reference signal. The reference signal was taken from the synchronous TTL output of the signal generator used to drive the test specimens.

The piezoceramic gauges on the bar specimens were calibrated against conventional CEA-13-125UN-120 resistive gauges from Measurements Group, Inc., placed in a half-bridge arrangement next to each gauge, as shown in Figures 3.2 and 3.4. Using a fixed frequency, the specimens were driven at different peak strain levels in the range from 0.1 $\mu\varepsilon$ to 100 $\mu\varepsilon$, the range in which the foil gauges could be effectively used. After amplification by Measurements Group Inc. strain gauge amplifiers, a PAR 186 lock-in amplifier was used to further filter and amplify the strain gauge signals (Fig. 3.9). An RMS voltmeter was then used to measure the output of the lock-in amplifier. This voltage was then converted to strain with a knowledge of the amplifier gains and gauge factors from the manufacturer specifications. The resulting piezoceramic output voltage was then plotted against strain and a calibration factor, the slope of the curve, was obtained by performing a least squares fit, as shown

in Figure 3.10. This process was repeated for each bar specimen due to the uncertainty in the piezoceramic material's electro-mechanical coupling coefficient. On the tubes, each piezoceramic gauge was first calibrated separately against two sets of foil gauges, placed on either side of each piezoceramic gauge (Fig. 3.5 - 3.6). Then, the results from each calibration were averaged to obtain a calibration factor relating the output voltage from the piezoceramic gauge, to the average strain from the two sets of gauges.

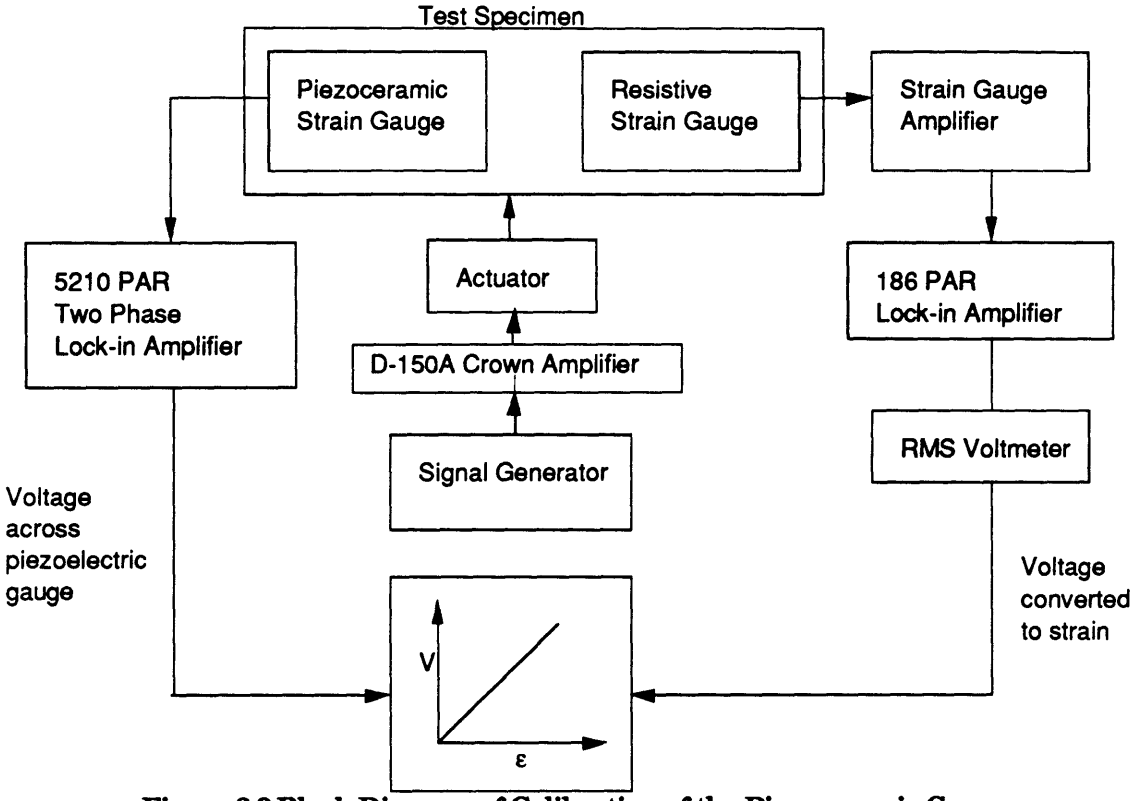

Figure 3.9 Block Diagram of Calibration of the Piezoceramic Gauges

To calibrate the interferometer testbed sensor, the truss was driven at different strain levels and the output from the piezoceramic gauge on the instrumented strut was plotted vs the strain from the adjacent resistive strain gauges. The resistive gauges on the structural sensor strut were placed in a full bridge arrangement for the purpose of temperature compensation. A separate calibration was performed for the piezoceramic gauge at the frequency of each mode that was tested.

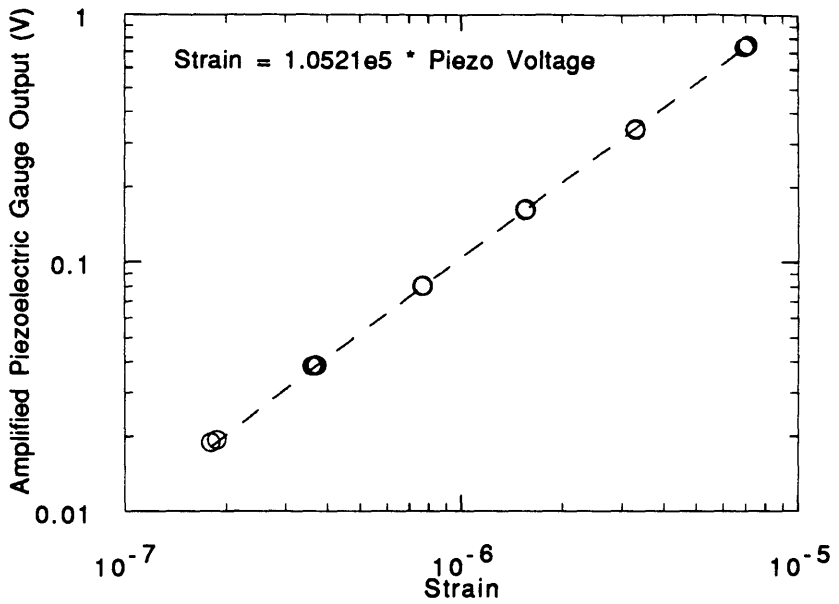

Figure 3.10 Typical Calibration Results for Piezoceramic Gauge on the 1.3 m Aluminum Bar Driven at 9.23 Hz

3.2 Actuators

There were two possible approaches to the problem of strain actuation in the material and structural test specimens -- through the application of force or moment actuation or through the application of strain actuation. The approach used to actuate strains in this study involved a shaker or proof mass actuator. Due to the low mass and damping of the material damping test specimens, the actuators used to excite nanostrain vibrations had to meet several requirements. The one major requirement was that the actuators had to exhibit a linear, non-hysteretic force response down to the levels necessary to induce nanostrain vibrations. Implied in the minimum hysteresis requirement was the argument that the actuators had to have a minimal effect on the damping of the test specimens, minimal being less than the inherent material or structural damping. An estimate of the tip force required to produce a maximum bending strain of 1 $\mu\varepsilon$ using a static cantilevered bar with a 25.4 mm x 3.2 mm cross sections was on the order of 1 μN.

Direct strain actuation [Forward, 1980] was ruled out due to a concern that the passive mechanical properties of the bonded actuator might influence the material damping of the specimen. Several force actuator options were considered for use in this study. Conventional shakers were found to be too massive, and ineffective at low vibration levels because of amplifier noise and hysteretic behavior. Another possibility was an accelerometer driven as a force actuator, using the proof mass inside the accelerometer normally used to measure accelerations as a proof mass actuator. This option was found possibly to be destructive to the accelerometers. Finally, an actuator using a piezoelectric ceramic bending motor was developed which met the linearity requirement.

The bending motor, purchased from Piezo Systems, consisted of two 0.25 mm thick sheets of oppositely polarized G-1195 piezoceramic material attached to either side of a 0.025 mm thick piece of metal shim (Fig. 3.11). When a voltage was applied across the motor, the material on one side of the shim contracted while the material on the other side extended causing the motor to bend [Piezo Systems, 1988]. When mounted as a cantilevered beam, the accelerating mass of the bending motor induced a reaction at its root. An estimate of the blocked force, the force at the root of a cantilevered motor [Piezo Systems, 1988] produced by a typical size bending motor, 38.1 mm x 12.7 mm x 0.53 mm showed that a DC voltage of 1 mV across the motor produced a force of 1 μN. Available signal generators were capable of producing a noise free sine wave excitation with an amplitude of 1 mV RMS. The combination of these sine wave generators and piezoelectric motors indicated that a force of 1 μN was obtainable without special equipment.

As shown in Table 3.3 and Figure 3.11, the piezoceramic actuator used to actuate the bar specimens was a 12.7 mm x 38 mm x 0.53 mm rectangular bending motor weighing 1.54 g. The dimensions were chosen to place the frequency of the first bending mode of the bending motors away from the modes of the material damping test specimens. With a total cantilevered length of 29 mm, the frequency of the first bending motor was 309 Hz. 3M Company 2215 structural adhesive was used to bond the bending motors to the end of each bar. Electrical connections were made with a pair of 36 gauge twisted magnet wire.

Table 3.3 Summary of Actuators Used on the Material and Structural Damping Specimens

Actuator	Application	Dimensions (mm)	Length (mm)	Total mass (g)	First bending frequency (Hz)
Bending motor	Material test specimens	12.7 x 38	28.8	1.54	309
Bending motor + tip mass	Large strain actuation of material test specimens	12.7 x 38	28.8	3.35	125
Bending motor + tip mass	Testbed actuation	12.7 x 38	28.8	3.95	111
D.C. motor	Large strain actuation of testbed	----------	------	332	-----

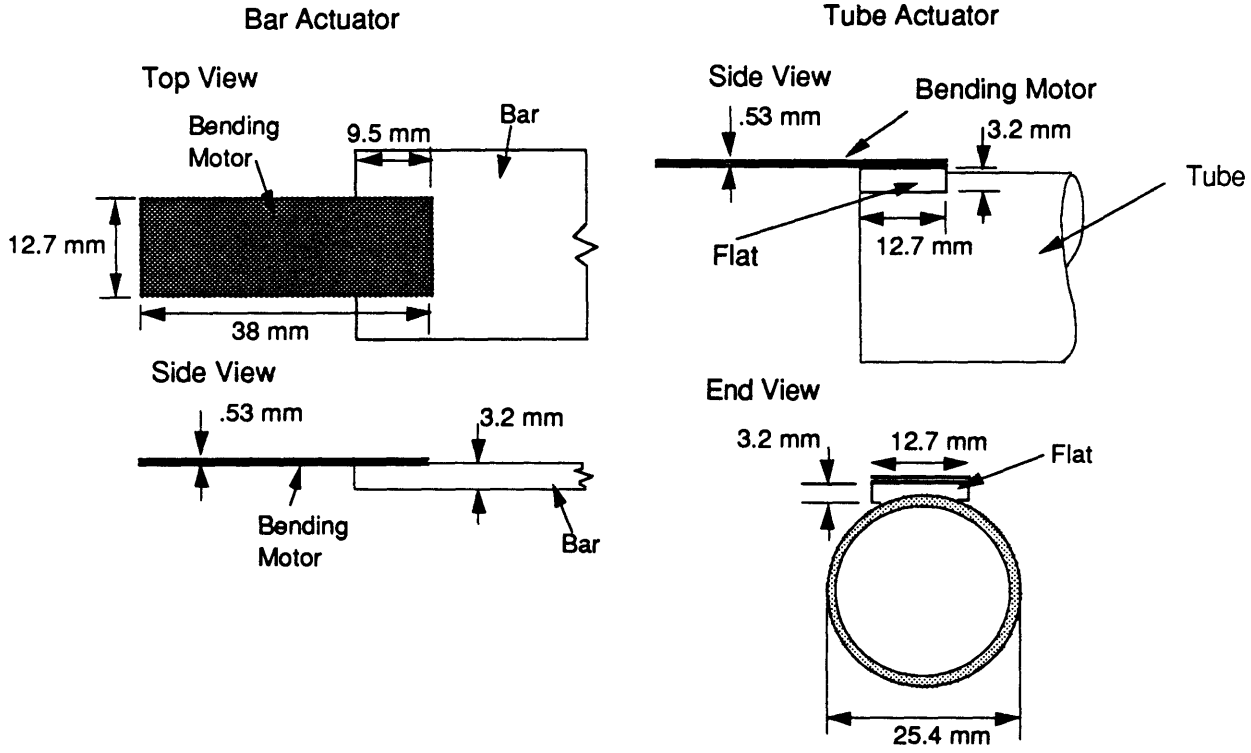

Figure 3.11 Typical Actuator Configuration

Because the piezoceramic bending motors were so stiff and brittle, they could not be bonded to the curved surface of the tube specimens. As shown in Figure 3.11, to attach the bending motors, separate flats, 12.7 mm long by 12.7 mm wide were machined out of 6061-T6 aluminum to fit the outer radii of the tubes. The motors were then bonded to the flats and the flats to the tubes with 3M 2215 epoxy.

The bending motors produced enough force to actuate strains up to 10 με in the material damping test specimens. Since it was desirable to test at higher strains, up to 1000 με, two steps were taken to produce larger strains. First, as shown in Figure 3.12, extra mass was added to the tips of

the actuators. The total mass that could be added to the tip of the bending motors was limited by the effect of the added mass of lowering the lowest modes of the actuators. Four 4/40 nuts, weighing a total of 1.81 g, were bonded to the ends of the cantilevered benders using five minute epoxy. Second, the input signal was amplified with a D-150A Crown amplifier to increase the maximum bending motor deflection. These steps cause the peak induced strain to increase to the order of 1000 με.

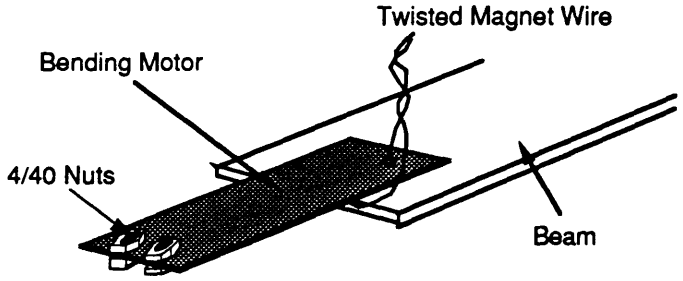

Figure 3.12 Addition of Mass to Material Damping Actuators

Two different actuators were used to drive the testbed -- a piezoceramic bending motor and a DC servo motor. At strain levels up to 1 με, the piezoceramic actuator shown in Figure 3.13 was used. A bending motor, identical in size to the material specimen actuators, was attached to a 25 mm x 81 mm x 3.2 mm aluminum base with 2215 epoxy. To increase the output force, a 10 mm x 12.7 mm x 3.2 mm block of aluminum, weighing 2.41 g was attached to the tip of the bending motor. The actuator was fastened to a node of the interferometer structure with a 10/32 Allen cap bolt. Placement of the actuator, shown in Figure 3.8, was chosen to maximize the first mode strain. Twisted magnet wire, the same wire used for the sensors, was used to connect each of the piezoelectric actuators on the material damping specimens to the amplifiers. For strains from 1 με to 100 με, the piezoceramic actuator was replaced with a brush type, Pittman D.C. servo motor shown in Figure 3.13. The motor drove a set of four circular aluminum masses, each weighing 21.8 g.

Two different signal generators were used to drive the material damping and structural damping specimen actuators. A Model 132 Wavetek signal generator was used to drive the bending motors on the aluminum bars and tubes and also the Gr/Ep bars. For increased frequency resolution, a Phillips PM5191 programmable

synthesizer/function generator was obtained to drive the motors on the Gr/Ep tubes and the testbed, and the modified bending motors used for large strain actuators.

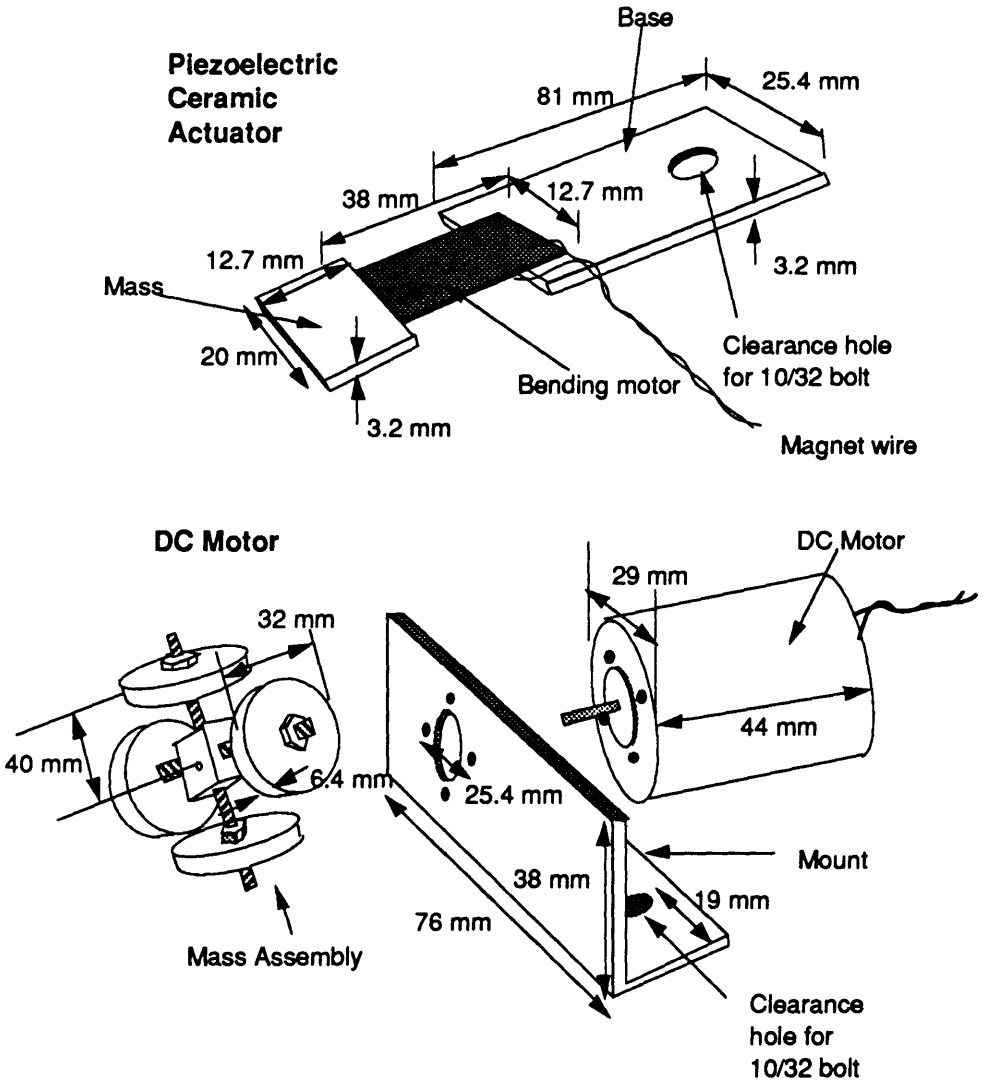

Figure 3.13 Testbed Actuators

3.3 Measurement of Damping

After instrumenting the material and structural damping specimens, and calibrating the piezoceramic strain sensors, testing was performed to obtain damping. In order to make correlation of the results from the tests of material and structural damping easier, and to reduce uncertainties in the comparisons, similar procedures were followed in all tests. In this section, the procedure for the testing of the material and structural damping specimens is presented.

The goal of the material and structural damping tests, was to obtain an accurate and precise measurement of the critical damping ratios, ζ, for each of the specimens. In making the measurements to find the damping ratios, there were several sources of error and noise which reduced the accuracy of the resulting damping ratios. There was error due to the effects of air on the vibrating structures and the influence of mechanical and electrical noise from various sources. Many steps were taken to eliminate or reduce these sources of error and noise. These steps are described in Sections 3.3.1 and 3.3.2.

3.3.1 Reducing the Effects of Air Damping

One of the major potential sources of error was damping caused by aerodynamic effects. The two different models for air damping are based on friction in the viscous boundary layer which is independent of amplitude [Batchelor, 1977], and damping due to quasi-steady drag, which is amplitude dependent [Blevins, 1977]. These effects are discussed in more detail in Chapter 4. Theoretical models of both these effects showed that at strain levels below 10 $\mu\varepsilon$, the damping due to air, ζ_{air}, was on the order of 10^{-5}, an order of magnitude below the inherent damping of a majority of the test specimens. At strain levels above 10 $\mu\varepsilon$, the damping was on the order of 10^{-4}, a significant effect. To avoid the aerodynamic effects at strain levels above 10 $\mu\varepsilon$, the large strain material damping tests were performed in vacuum. To simplify the testing procedure, low strain material damping tests were performed in air. Since the interferometer testbed actuators were only capable of actuating maximum strains on the order of 10 $\mu\varepsilon$, structural damping tests performed on the interferometer structure were performed only in air.

3.3.2 Mechanical and Electrical Isolation

A number of steps were taken to minimize the mechanical and electrical noise affecting the material and structural damping specimens. The material damping specimens were tested while suspended inside the 4.27 m high, 3.05 m diameter vacuum chamber of the ASTROVAC, a space simulation facility at M.I.T. (Fig. 3.14). Performing all testing in the chamber made experiments in vacuum possible with minimal changes in the test arrangement. Testing in the large metal chamber also reduced noise from other air effects and electrical noise sources. It was believed that the closed metal chamber reduced disturbance from air currents by limiting air circulation, provided some acoustical isolation, and reduced electrical noise by acting as a Faraday cage.

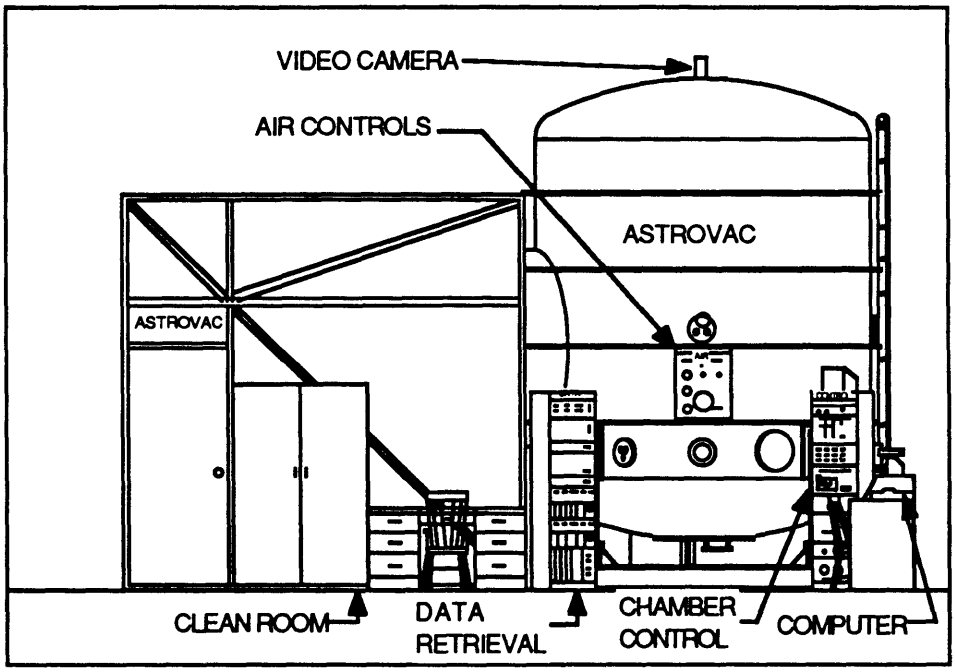

Figure 3.14 MIT ASTROVAC Facility [Sarver and Crawley, 1987]

Electrical connections between the inside and the outside of the vacuum chamber, shown in Figure 3.15, followed two separate routes for the tests in air and vacuum. For the tests at small strain levels performed in air, an attempt was made to minimize electrical noise. The RG-58 coaxial cable used to connect the piezoceramic sensors and actuators to the instrumentation was run through the chamber doorway and was kept as short as possible. For tests in vacuum, the chamber door was closed and latched so that electrical connections had to be made through the

ASTROVAC vacuum connectors [Sarver and Crawley, 1987]. A separate calibration of each piezoceramic gauge was performed for each of the two different connection configurations.

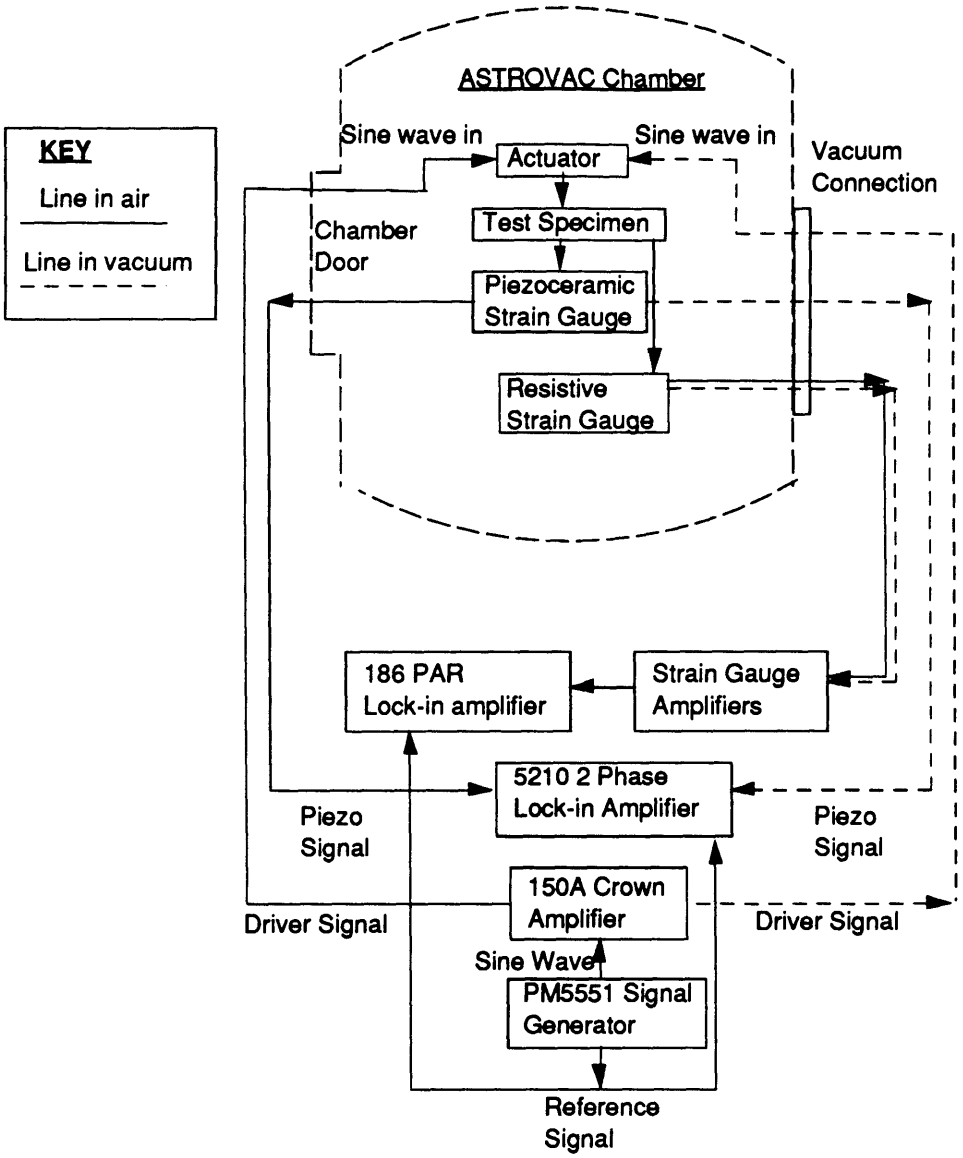

3.15 Electrical Connection of Test Equipment in the ASTROVAC

Another major source of noise was noise from mechanical vibrations in the laboratory caused by air compressors, turbines, and other machinery. The material damping specimens were suspended from a Dexion frame inside the vacuum chamber. Isolation from external mechanical noise was provided by a suspension system, shown in Figure 3.16. The suspension consisted of two sets of three springs with stiffnesses of 6.65 N/m and two sets of 0.18 kg lead cubes with eyehooks for attachment

to the springs. In an attempt to achieve additional isolation, small pads made of foam rubber were placed between the attachment point of the suspension to the Dexion frame. The frequency of the highest mode of the suspension system was 0.9 Hz. The transfer function of a model of the suspension system, given in Figure 3.17, showed that the suspension had a transmission roll-off of around 40 dB at the lowest frequency tested, 6.17 Hz. A series of tests comparing the noise floor of the 1.7 m aluminum bar hung with and without the isolation system showed an actual reduction of roughly 12 dB. With the isolation system, the measured baseline noise was on the order of 0.1 nε.

Mechanical noise isolation of the testbed was performed by suspending the structure with three springs with a stiffness of 1670 N/m, giving the 31.8 kg testbed structure a bounce mode of 2 Hz. Further reduction in mechanical and electrical noise was achieved by performing the tests at the lowest strain levels after 10:00 P.M., when most of the machinery and electrical devices in the building were turned off.

Another source of error was due to the interaction between the specimens and the suspension. To minimize the losses due to the interaction between the specimens and the suspension, the test specimens were suspended at their nodes using a wire cradle, shown in Figure 3.16 [Braginsky et al, 1985]. The cradle consisted of a loop of magnet wire held together with a clamp. Friction losses at the cradle/specimen interface were reduced by applying a thin coating of grease in the vicinity of the suspension points [Braginsky et al, 1985]. Further external mechanical effects, due to interaction between the electrical wires and the specimens, were reduced by running the very light magnet wire leads to the nodes.

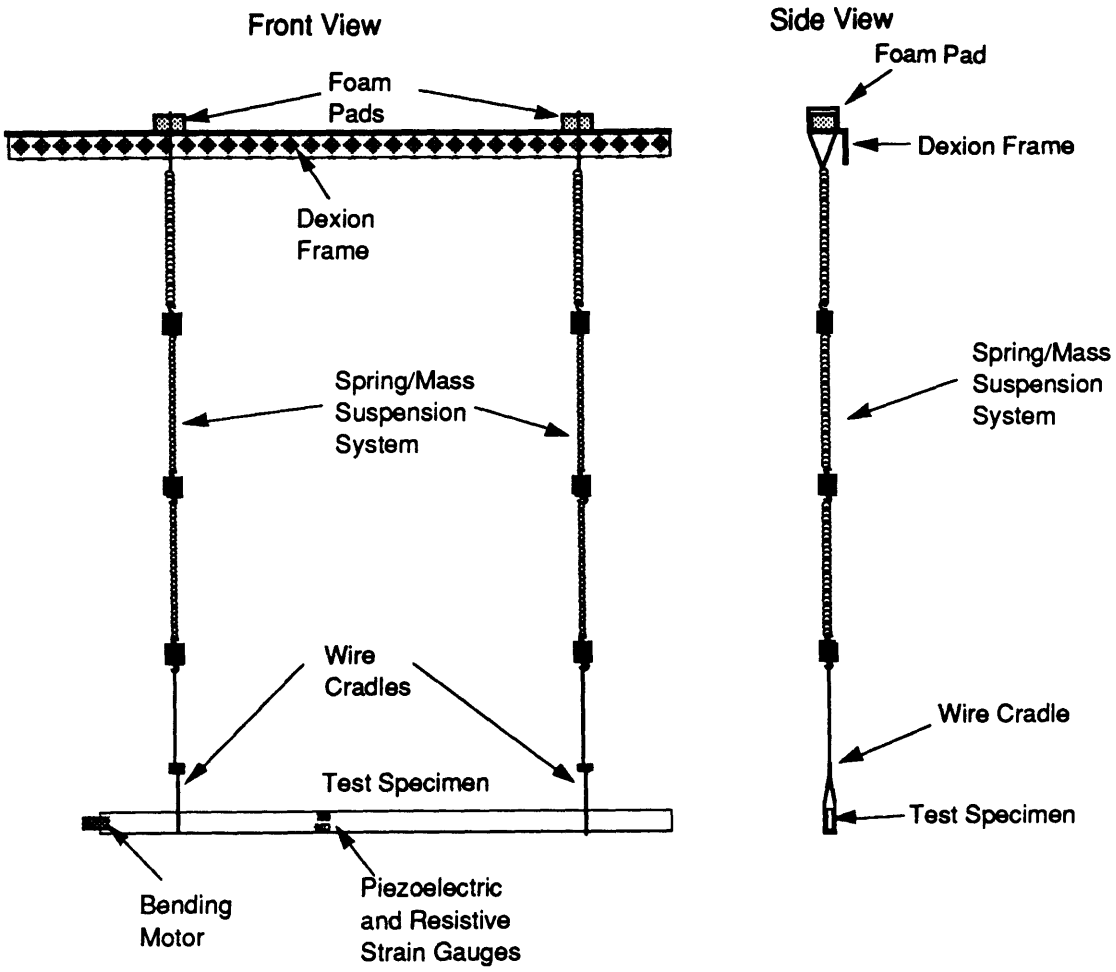

Figure 3.16 Suspension of Material Test Specimens in the ASTROVAC

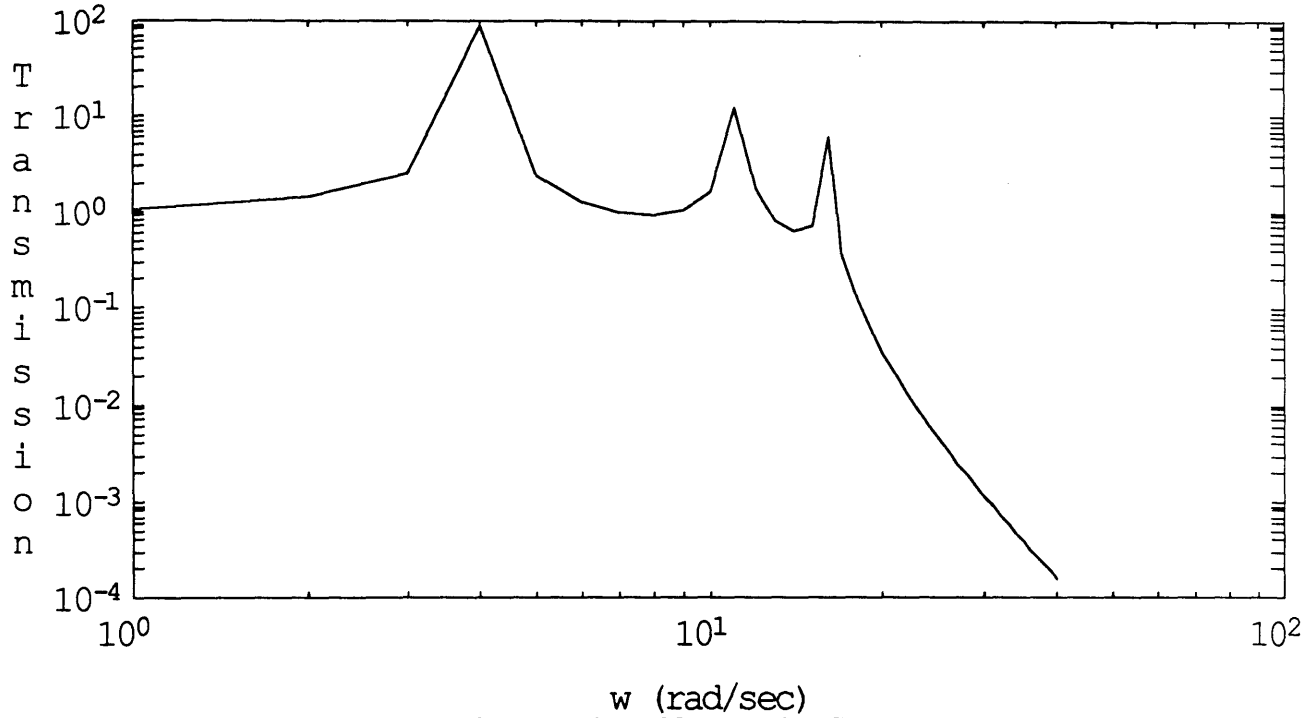

Figure 3.17 Transfer Function of Suspension System From MATLAB Model

3.3.3 Sine Sweep Procedure

After suspension of each specimen and connection of the sensors and actuators, a frequency sweep was performed to determine the frequencies of the first two to four modes of the material and structural damping specimens. Then the piezoceramic strain gauges were calibrated at or near each of the resonant frequencies using the procedure discussed in Section 3.1. After the calibration factors were obtained for the material damping specimens, the wires used to hook up the resistive strain gauges on the material damping specimens were removed to reduce any damping which they might have introduced. However, since the effects of the resistive strain gauge wires were small on the 31.8 Kg interferometer truss, the strain gauge wires connecting the sensor strut were not removed.

With as many sources of noise as possible reduced, tests were performed to determine damping. The quantity used as a measure of the damping was the critical damping ratio, defined as one half of the fractional decrease in energy of a system in one cycle [Meirovitch, 1986],

$$\zeta = \frac{\Delta U}{4\pi U} \qquad [3.1]$$

and in terms of frequency,

$$\zeta = \frac{\Delta f}{2f_n} \qquad [3.2]$$

where Δf is the difference in the frequencies of the half-power points. The half power points are the points at which the response is reduced to 0.7071 of the peak response and f_n is the resonance frequency.

To find material and structural damping in air using the sine sweep or half-power bandwidth method, the following steps were taken. First, the amplitude of the sine wave input to the piezoceramic actuator or shaker was set. Second, a frequency sweep of the material damping test specimen was performed. The strain response was measured at many different frequencies around the peak and the half power points (Fig. 3.18). Measurements around the peak and half power points were more closely spaced then elsewhere, as closely spaced as 0.1 mHz, the maximum frequency resolution of the PM5191 frequency generator. The peak strain was then calculated from the piezoceramic gauge output by multiplying by the calibration factor for that gauge. Damping was computed using Equation 3.2. After six to ten consecutive sweeps were performed at the same strain level, the input voltage was raised or lowered and the procedure was repeated. Measurements were taken at peak strain levels from 1 nε to 100 με. To find the peak strains from the measured strains, correction factors were computed. These factors were found by relating the strain at the position of the strain gauge to the strain at the antinode, calculated from the theoretical mode shape [Blevins, 1984].

After evacuating the ASTROVAC chamber, testing of the material damping specimens in vacuum was performed using the same procedure as for the tests in air. First, a specimen was suspended inside the chamber and all electrical connections were made. Next, the chamber door was closed and latched to maintain a good O-ring seal. Two to three sine sweeps were performed in air at a single strain level so that the results could be compared with the data taken in vacuum. Then the ASTROVAC mechanical roughing pump was used to pump out the air in the chamber. Approximately one hour after the beginning of the pumpdown, at a vacuum of 3.00×10^{-5} Pa, sine sweep tests were performed to determine the material

damping of the test specimens. The temperature of the specimens were monitored using two solid state temperature transducers attached to similar size control pieces of aluminum and Gr/Ep in the chamber. It was assumed that the temperature of the control pieces in the chamber was the same as the temperature of the test specimens. Tests were performed in vacuum when the test specimens were at nearly the same temperature as the specimens tested in air, around 20° C.

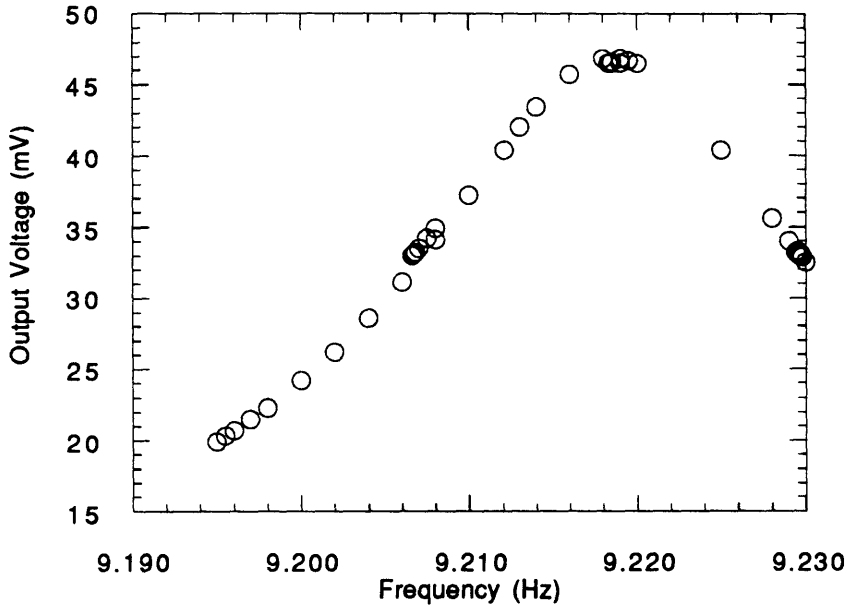

Figure 3.18 Sample Output From Sine Sweep of 1.3 m Aluminum Bar

CHAPTER 4

RESULTS AND CORRELATION

In this chapter, results from the tests measuring both material and structural damping are presented. In Section 4.1, the theoretical as well as the experimental aspects of the accuracy and precision of the damping measurements is discussed. In Section.4.2, the results from the material damping tests performed in both air and vacuum are presented as well as comparisons with theoretical models where appropriate. In Section 4.3, the results from the structural damping of the precision truss are presented.

4.1 Precision and Accuracy of Measurements

As with any set of experiments, there were limitations placed on the precision and accuracy of the measured quantities. Limitations on the precision of the measurement of the damping ratios were imposed by the noise in the measurement and other miscellaneous factors, as indicated by the scatter in the data. Limitations on the accuracy of the measurement of the damping ratios were imposed by two sources -- the effects of the air and of the suspension of the specimens. These bounds on precision and accuracy are discussed sequentially below.

One of the quantifiable measures of the precision of the damping ratios was the uncertainty caused by electrical and mechanical noise in the strain measurement. As discussed in Section 3.2, the baseline noise level was on the order of 0.1 nε. This uncertainty propagated a possible error into the damping ratios which were derived using the procedure presented in Section 3.3. The expression describing the uncertainty in damping ratio, Equation A3.2 in Appendix 3, depends on the measured value of damping ratio and the resonant frequency as well as the uncertainty in the strain measurements. These uncertainties for all of the material and structural damping tests are given in Appendix 1 in the column marked "Error from Noise". In the worst case, the noise caused an uncertainty as high as 7.12×10^{-4} in the value of the damping ratio of the second mode of the 1.7 m long aluminum bar measured with a peak strain of 1.18 nε. In the best case, the noise caused an uncertainty as low as 1.46×10^{-10} in the value of the damping ratio of the first mode of the 0.9 m $[\pm 15]_{6s}$ Gr/Ep bar with a

peak strain of 3.63 με. The results from the damping tests are summarized comprehensively in Sections 4.2 and 4.3 by figures such as Figures 4.1 - 4.3. In these figures, the error bars represent the range of possible error due to noise. In cases such as that presented in Figure 4.2, the range at low strain is significant, but diminishes as the strain increases. In other cases such as Figure 4.3, the error range is never significant.

Another indication of the precision of the damping ratios was the scatter in the data. Measurement of each damping ratio, obtained by six to ten sequential sine sweeps at one strain level, showed some scatter in the data. The maximum and minimum of the sequential sine sweeps are listed in the Tables of Appendix 1 as, "Minimum Damping Ratio", and "Maximum Damping Ratio," and the arithmetic mean as "Average Damping Ratio." The average, minimum, and maximum are also shown in the data plots. Between the minimum and maximum, the measurements were approximately uniformly distributed, indicating that the minimum and maximum represented bounds on the scatter in the data, as opposed to representing the measured limits on a Gaussian process. This scatter was due to several factors. One possible source of scatter was the variation in the temperature of the laboratory over the time needed to complete the tests of each specimen. A small change in temperature causes a change in the modulus of a material which, in turn causes a shift in frequency, and in material damping. This temperature shift was illustrated by the shift in the resonant frequencies of all the material damping test specimens, up to 5 mHz over each set of tests. Other possible causes of scatter, which were not quantified, were noise in the acoustic range, micro-slippage of the suspension, and uncertainty in the human interpretation of the data.

The other factor affecting the quality of the damping ratios was the accuracy of the measurements. Limits on the accuracy of the measurements were imposed by two main sources -- the effects of aerodynamic damping and suspension on the specimens. The modeling and determination of the severity of these two effects are discussed below.

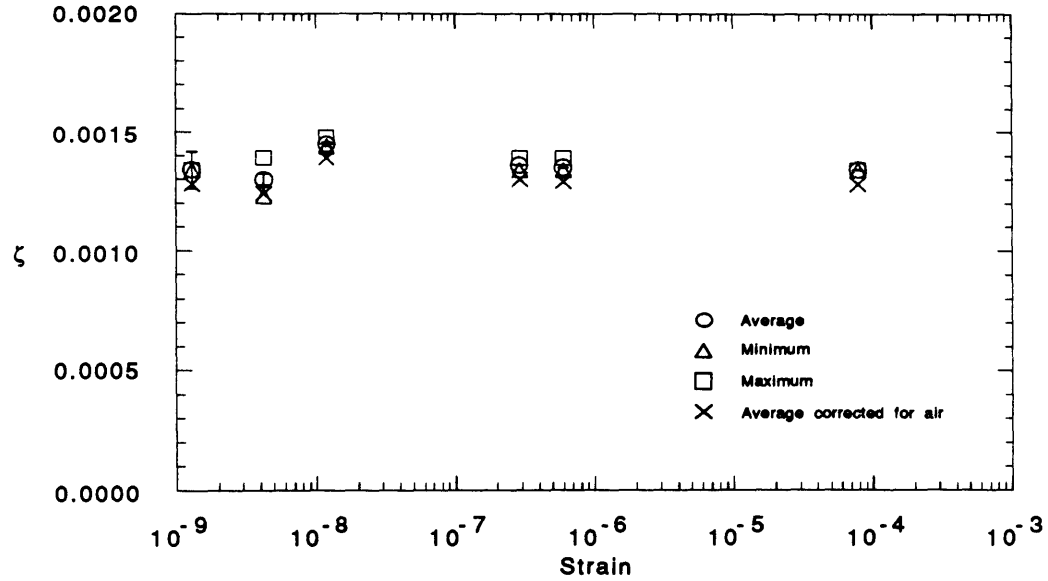

Figure 4.1 Damping Ratio vs. Strain: First Mode of 1.3 m Aluminum Bar in Air , f= 9.35 Hz

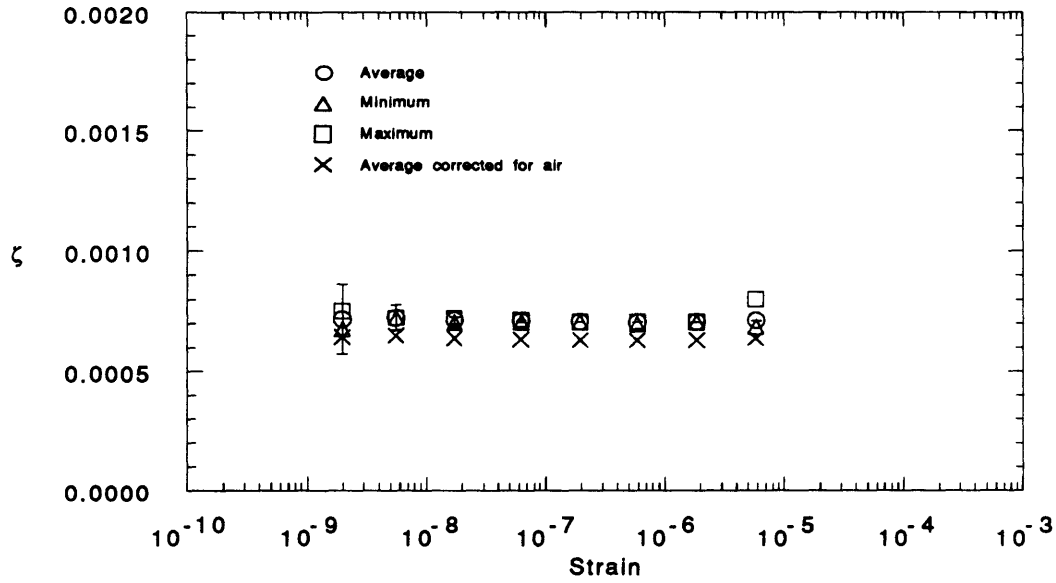

Figure 4.2 Damping Ratio vs. Strain: First Mode of 0.7 m $[\pm 15]_{6s}$ Gr/Ep Bar in Air, f = 53.1 Hz

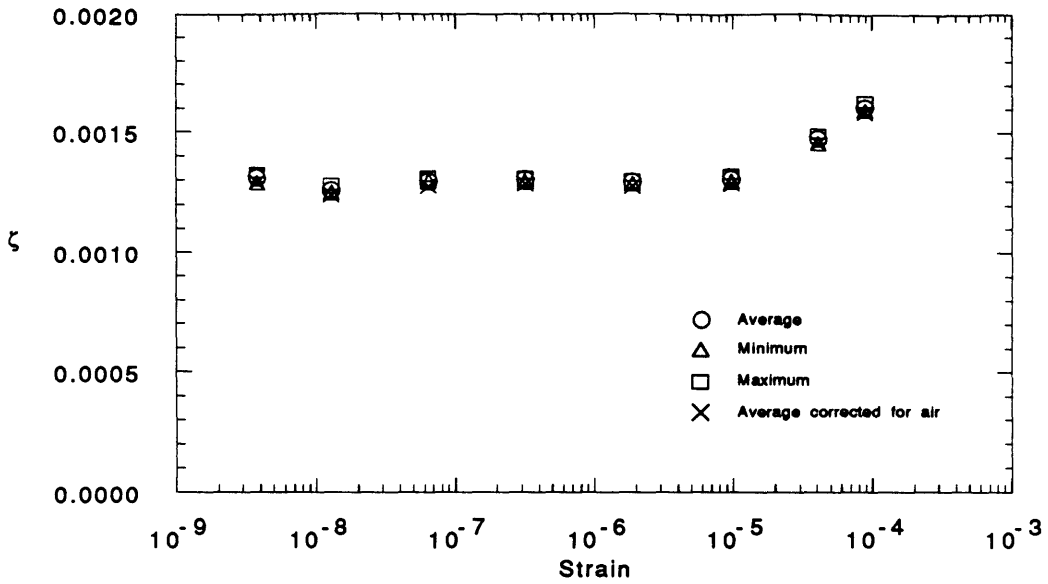

Figure 4.3 Damping Ratio vs. Strain: First Mode of 0.7 m $[\pm 15]_{3s}$ Gr/Ep Tube in Air, f=503.0 Hz

Aerodynamic damping effects can be modeled in at least two different ways. First, by the viscous friction in the boundary layer of the oscillating test specimens. Second, as a quasi-steady drag force on the specimens. Depending on the amplitude and frequency, both phenomena make a contribution to the damping of the specimens.

Viscous damping on an oscillating structure arises from the work done by the structure against the fluid flow in the viscous boundary layer. The expression for this damping is derived assuming that the far field flow is irrotational, and that the associated boundary layer thickness is much smaller than the width of the structure. The damping is independent of the amplitude of vibration [Batchelor, 1977]. For a cylinder oscillating in air, this damping, ζ_o, is given by,

$$\zeta_o = 2\left(\frac{\rho}{\rho_s}\right)\sqrt{\frac{2\nu}{\omega D^2}} \qquad [4.1]$$

where ρ is the density of the air, ρ_S the density of the cylinder, ν the kinematic viscosity of the air, ω the frequency of vibration, and D is the diameter of the cylinder [Batchelor, 1977]. The equivalent expression for a rectangular bar is difficult to evaluate due to singularities in the flow at the

sharp edges. However, if the rectangular cross section is approximated with an elliptical section of approximately the same aspect ratio and the constants are evaluated for the dimensions of the rectangular bar specimens used in this investigation, then the damping is given by,

$$\zeta_o = 9.13\left(\frac{\rho}{\rho_s}\right)\sqrt{\frac{2\nu}{\omega D^2}} \qquad [4.2]$$

where D is now the the width of the bar. A derivation of Equation 4.2 is given in Appendix 2.

The second model of aerodynamic damping of a vibrating structure is based on drag, as postulated by Blevins [1977]. The derivation of the expression describing this damping assumes a quasi-static solution, with a nearly constant Reynolds number over the period of one cycle. The damping due to quasi-steady drag, ζ_S is derived assuming a spatially sinusoidal mode shape, and is given by,

$$\zeta_s = \frac{16C_D a}{3\pi^3 n^2}\left(\frac{\rho}{\rho_s}\right)\left(\frac{L^2}{Dt}\right)\varepsilon \qquad [4.3]$$

where C_d is the drag coefficient, a is a shape coefficient which can be taken to be approximately one, n the mode number, L the length, t the thickness, D the width, and ε is the maximum strain in the structure [Blevins, 1977]. From Equation 4.3, it can be seen that the damping ratio based on drag, ζ_S depends on the strain amplitude, unlike the damping based on oscillatory viscous boundary flow.

To investigate the relevancy of these models, the air damping predicted by the models of Equations 4.1 - 4.3, were compared with the experimentally obtained values of air damping, ζ_{air}. The contribution due to air was found experimentally by comparing the results from the tests of the material damping specimens in vacuum and air at roughly the same strain level. These results are presented in the fifth column of Table 4.1 along with the strain amplitudes at which the damping ratios were measured in air. Predictions based on the oscillatory models of Equations 4.1 and 4.2, in the third column of Table 4.1, are much closer to the experimentally measured values than those from the quasi-steady model of Equation 4.3, in the fourth column. The oscillatory viscous damping

predictions are within a factor of three of the experimental values compared to the closest predicted value from the quasi-steady model, which is off by a factor of fifty-one. These results show that the oscillatory viscous model is the more relevent model at strain levels up to 10 με. Predictions from Equations 4.1 and 4.2 are used to correct the values of ζ found from tests of the material damping in air. The corrections are listed in the Tables of Appendix 1 as "Damping Ratio Due to Air," and the average measured value is shown corrected for air damping in the column marked "Average Corrected for Air." On the data figures, the average corrected for air is also shown.

At strain levels measured above 10 με, the amplitude dependent quasi-steady damping may dominate the damping. In order to avoid larger inaccuracies, tests on specimens in the large strain range, above 1 με, were performed in vacuum, and no corrections were made in the experimental results for damping due to drag.

Table 4.1 Comparison of Predicted and Experimental ζ_{air}

Specimen Tested	ε in air	Predicted ζ_o	Predicted ζ_s	Experimental ζair
0.5 m Al bar	.461 με	2.31×10^{-5}	8.40×10^{-8}	1.28×10^{-4}
1.3 m Al bar	2.79 με	5.80×10^{-5}	5.68×10^{-7}	1.90×10^{-4}
0.7 m Al tube	1.11με	1.87×10^{-5}	1.76×10^{-7}	9×10^{-6}
0.9 m Uniply Gr/Ep bar	.635 με	9.77×10^{-5}	4.20×10^{-6}	1.70×10^{-4}
0.9 m $[\pm 15]_{6s}$ Gr/Ep bar	4.55 με	9.61×10^{-5}	4.20×10^{-7}	1.44×10^{-4}
0.7 m Gr/Ep tube	1.08 με	2.25×10^{-5}	2.96×10^{-7}	2.7×10^{-5}

The other major source of inaccuracy in the material damping measurements was due to dissipation through the suspension of the specimens. One indicator of this was the reproducibility of results. Over the course of one set of consecutive tests -- each test consisted of six to ten measurements of damping ratio at a single peak strain level, damping ratio values showed little variation. However, when a specimen was removed from the suspension system and then rehung, and six to ten sequential sine sweeps were repeated, the average damping ratio was

slightly higher or lower than the results measured before the rehanging. A series of tests were performed to measure the reproducibility of the damping measurements of the 0.9 m uniply Gr/Ep bar. Results from these tests are shown in Table 4.2. First, measurements of the damping ratios of the 0.9 m Gr/Ep bar with uniply layup were made using the procedure described in Section 3.3.3. The bar was then taken down from the suspension system, rehung, and damping measurements were made at roughly the same strain level as the previous tests. This process was repeated five times. Presented in Table 4.2, the results show a variation in damping ratio up to 4.3×10^{-5}. It can be inferred that this establishes an upper bound on the accuracy of all of the measured damping values.

Table 4.2 Damping Measurements From Repeated Tests of 0.9 m $[0]_{24}$ Gr/Ep Bar

Test Number	Peak Strain ($\mu\varepsilon$)	Average measured ζ
1	.635	3.83×10^{-4}
2	.210	4.25×10^{-4}
3	9.03	3.88×10^{-4}
4	7.94	4.31×10^{-4}
5	.944	3.89×10^{-4}

In summary, the indicators of the varying degrees of precision and accuracy of the material damping data are shown in Figures 4.1 to 4.3. Each damping ratio measurement represents the results from six to ten consecutive tests at a single strain levels. The strain levels reported are the peak strains in each test specimen at resonance. The damping ratio values presented in Figure 4.1 - 4.3, are the averages from each set of tests, plotted with open circles. As an indicator of the range over which measurements were made, minimum and maximum values from each set are plotted with open triangles and boxes respectively. In addition, error bars are plotted around the average values using values of damping ratio uncertainty due to noise calculated from Equation A3.2. In order to indicate the inaccuracy, the average material damping corrected for air damping, is plotted with an x. The difference between the average and the corrected average is an indicator of the possible inaccuracy and the corrected average is a better estimate of the actual material damping. Finally, there is an implicit limit on accuracy on the order of 4×10^{-5} due to the suspension.

In Figures 4.1 - 4.3, the general behavior of the material damping measurements can be used to summarize the limits on the precision and accuracy of the measured damping ratios. In general, precision increases with increasing frequency, increasing damping ratio, and increasing strain. Of the three sets of results, the damping ratios from the 0.7 m $[\pm 15]_{3s}$ Gr/Ep tube, shown in Figure 4.3, shows the least amount of scatter and inaccuracy. This 0.7 m Gr/Ep tube also has the highest natural frequency and among the largest average damping ratios of all the material damping specimens. The specimen showing the greatest amount of damping ratio scatter and noise at small strains, the 0.7 m $[\pm 15]_{6s}$ Gr/Ep bar shown in Figure 4.2, has a lower natural frequency than the tube and the lowest average damping ratio of the three. The precision of the results from the 1.3 m aluminum bar, with the largest average damping ratio, but lowest natural frequency, shown in Figure 4.1, lies somewhere in between the two other cases.

The accuracy of the measurements can be quantified using the results presented in the discussion of the air damping and the damping due to changes in the suspension. The effect of the air damping, shown in Figures 4.1 -4.3, have values ranging from 2.70×10^{-5} to 1.90×10^{-4}. This possible error can be combined with the inaccuracy due to the suspension, found earlier to be roughly 4×10^{-5}, to create a limit on the accuracy of the measured damping ratios ranging from 6.7×10^{-5} for the 0.7 m Gr/Ep tube to 2.3×10^{-4} for the 1.3 m aluminum bar.

The precision of the structural damping ratio measurements from the interferometer testbed were analyzed using the same methods used to analyze the material damping results. Like the material damping results, uncertainty was measured by calculating the error due to noise using Equation A3.2 and by observing the scatter in the data. As shown in Figure 4.4 by the set of typical test results from a mode of the testbed, the noise limited precision increased with increasing strain, with little scatter in the damping ratios.

The accuracy of the structural damping results could not be analyzed with the methods used for the material damping results. Because of the complicated geometry of the interferometer testbed, an estimate of the accuracy of the damping measurements due to air damping was not made

and results were not corrected for inaccuracies due to air. Also, because the testbed was never removed from its suspension, the quantification due to the loss throught the suspension system was not estimated. However, due to the large mass of the testbed, it is estimated that the inaccuracy in the measurements due to the suspension is no greater for the testbed than for the material damping specimens.

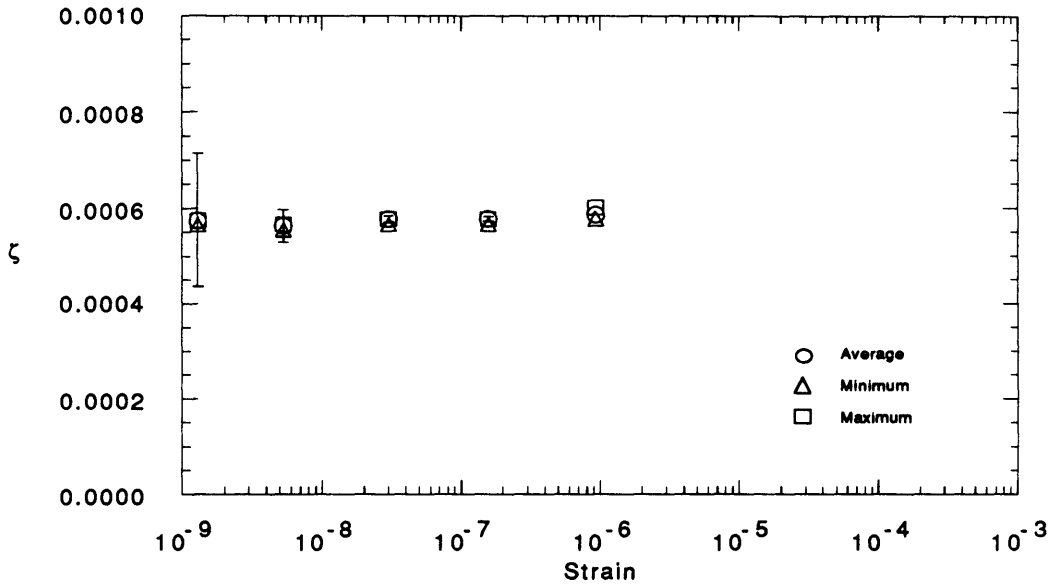

Figure 4.4 Damping Ratio vs. Strain: Testbed Mode #1, f=44.1 Hz, Small Strain Range

4.2 Material Damping Results

Having established the sources affecting accuracy and precision as well as their magnitudes, the actual measurements can now be discussed. In Sections 4.2.1 - 4.2.5, the damping results from the tests of the material damping specimens are presented, discussed, and correlated with theory where possible. In Section 4.3, the structural damping results from the tests of the interferometer testbed are presented.

4.2.1 Aluminum Bars

The simplest set of material damping specimens tested were the aluminum bars, whose damping is relatively well understood. A total of seven modes of the four rectangular aluminum bar specimens were tested over the lower strain range in air. The average values of damping

corrected for air obtained from these tests, as well as the range of strain over which the average values are calculated, are tabulated in Table 4.3. The strain range over which the damping ratios are averaged, in the third column, is the range over which damping appears to be independent of strain. A complete list of the test results is given in Appendix 1. In Figures 4.5 - 4.11, the damping ratios obtained from each aluminum bar specimen are plotted as a function of peak specimen strain

Table 4.3 Summary of Average Small Strain Damping From Al Bars Corrected For Air

Test Specimen	Frequency (Hz)	Strain Independent Range	Corrected Average Damping Ratio, ζ
1.7 m Al bar	6.17	1.42 nε - .968 με	1.17×10^{-3}
1.7 m Al bar	17.1	1.18 nε - 1.62 με	1.23×10^{-3}
1.3 m Al bar	9.35	1.30 nε - 78.1 με	1.30×10^{-3}
1.3 m Al bar	25.8	2.22 nε - 3.82 με	9.16×10^{-4}
1.3 m Al bar	50.6	2.02 nε - 12.4 με	5.62×10^{-4}
0.9 m Al bar	19.5	92.6 nε - 5.88 με	1.12×10^{-3}
0.5 m Al bar	173.6	8.25 nε - 13.3 με	2.50×10^{-4}

The measured damping ratios of the first and second modes of the 1.7 m long aluminum bar are shown in Figures 4.5 - 4.6. Because the frequencies are so low, the uncertainty in the damping ratio at the smallest strain level is large, sixty-one percent of the average damping of the second mode. However, within the bounds of the maximum and minimum damping ratios and the accuracy of the measurements, the results for both modes appear to be independent of strain down to at least 10 nε, with an average value given in Table 4.3. Like all of the aluminum bars, the contribution to the damping ratios due to air is small.

In Figures 4.7 - 4.9, the damping ratios of the first three modes of the 1.3 m long aluminum bar are shown. The damping exhibits little variation with strain with average values given in Table 4.3. Both the error due to noise and scatter are within the accuracy of the experiments.

In Figure 4.10, the damping ratios of the 0.9 m aluminum bar are shown. The 0.9 m aluminum bar was tested over a limited strain range for the damping of one mode, with an average value given in Table 4.3. Since

the strain range is limited to relatively large strains, the inaccuracy and uncertainty in the data are small.

In Figure 4.11, the results of the tests determining the damping of the second mode of the 0.5 m aluminum bar are shown. Because of the high frequency of the mode, the quality of the measurements is high. In the range of strain up to 13.3 με, the damping is independent of strain with an average value given in Table 4.3. After that point, the damping appears to increase -- at 27.9 με, the damping shows an increase in the corrected value of ζ of 3.67×10^{-4}. At a strain level of 10 με, the quasi-steady drag damping ratio, given by Equation 4.3, has a value of only 2×10^{-7} compared to the measured increase on the order of 1×10^{-4}. So, the increase in damping cannot be attributed to aerodynamic drag. A more likely cause is the hysteretic motion of dislocations at large strains [Boser, 1983] which is discussed in detail below in the discussion of the tests performed in vacuum.

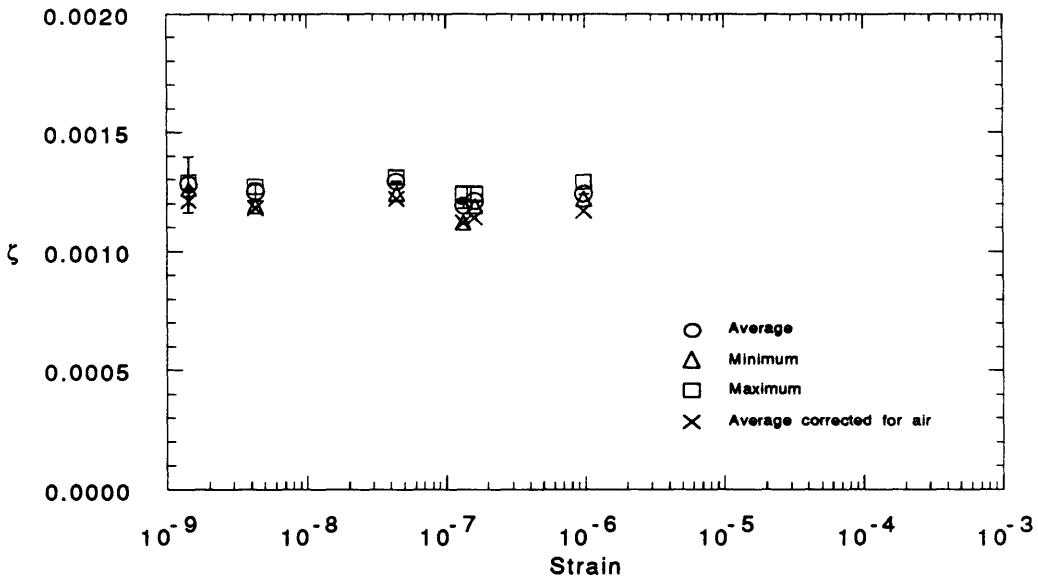

Figure 4.5 Damping in First Mode of 1.7 m Al Bar in Air, f=6.17 Hz

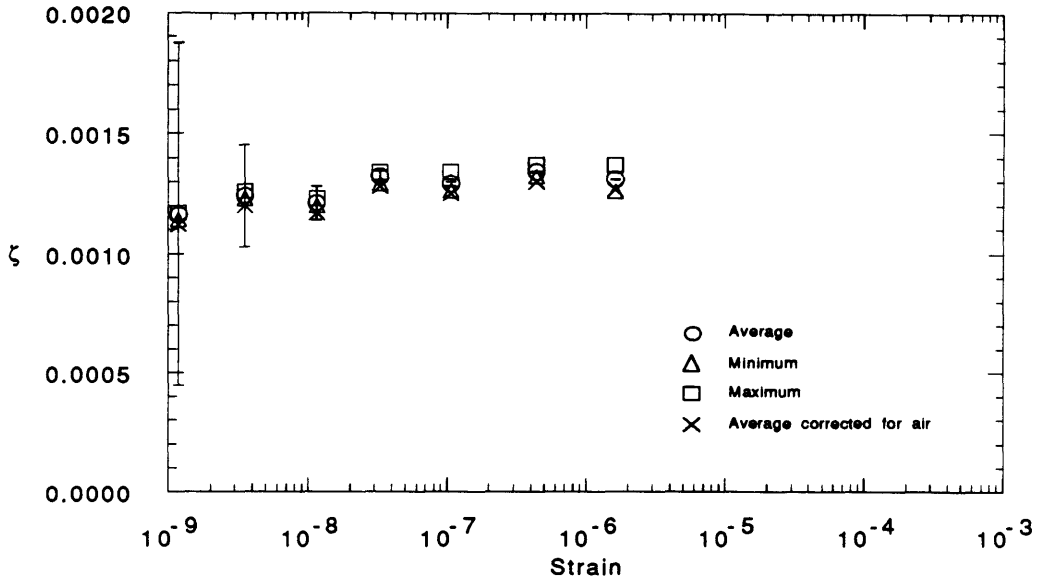

Figure 4.6 Damping in Second Mode of 1.7 m Al Bar in Air, f=17.2 Hz

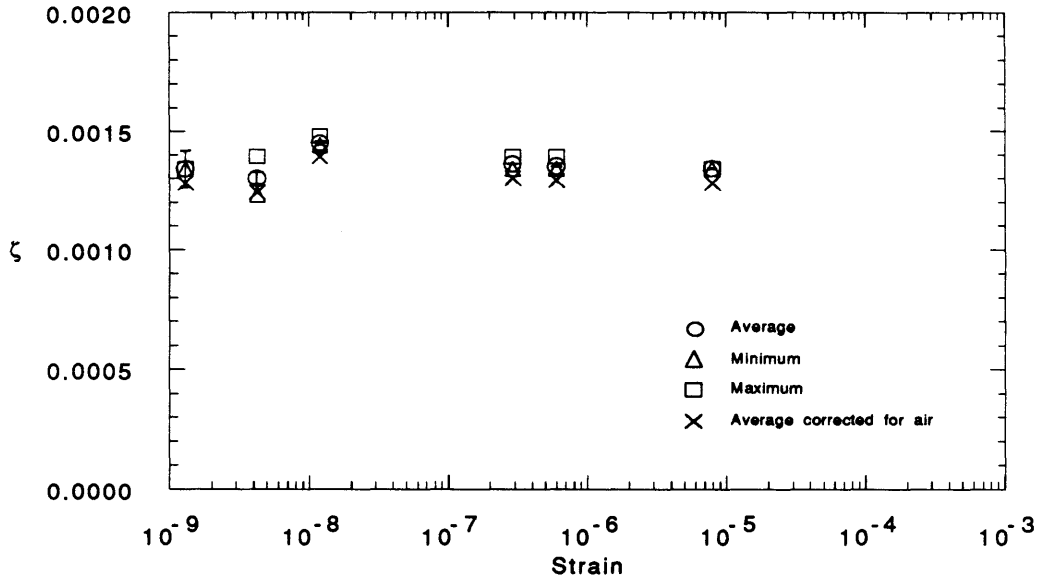

Figure 4.7 Damping in First Mode of 1.3 m Al Bar in Air, f=9.35 Hz

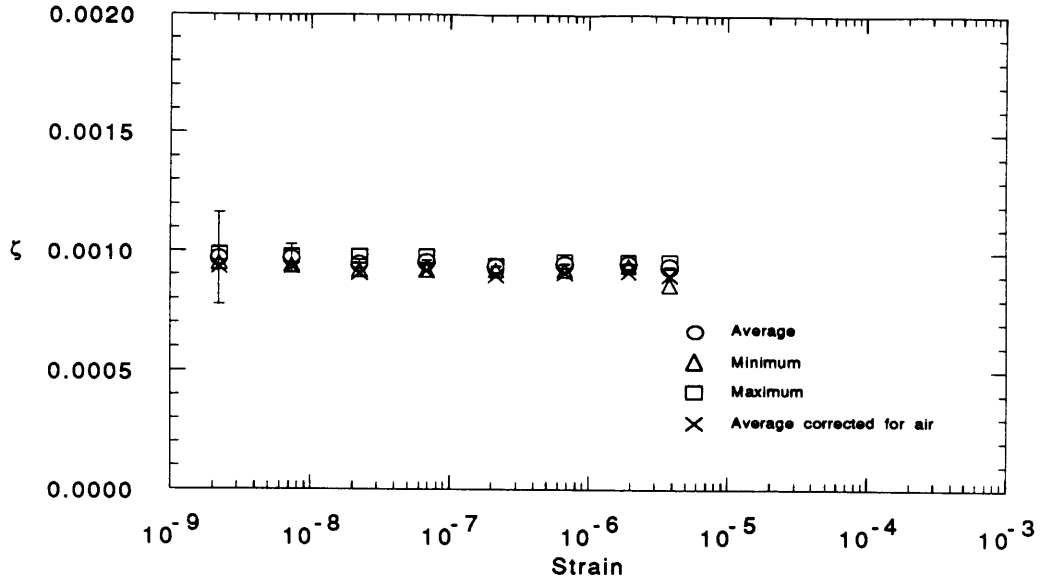

Figure 4.8 Damping in Second Mode of 1.3 m Al Bar in Air, f=25.8 Hz

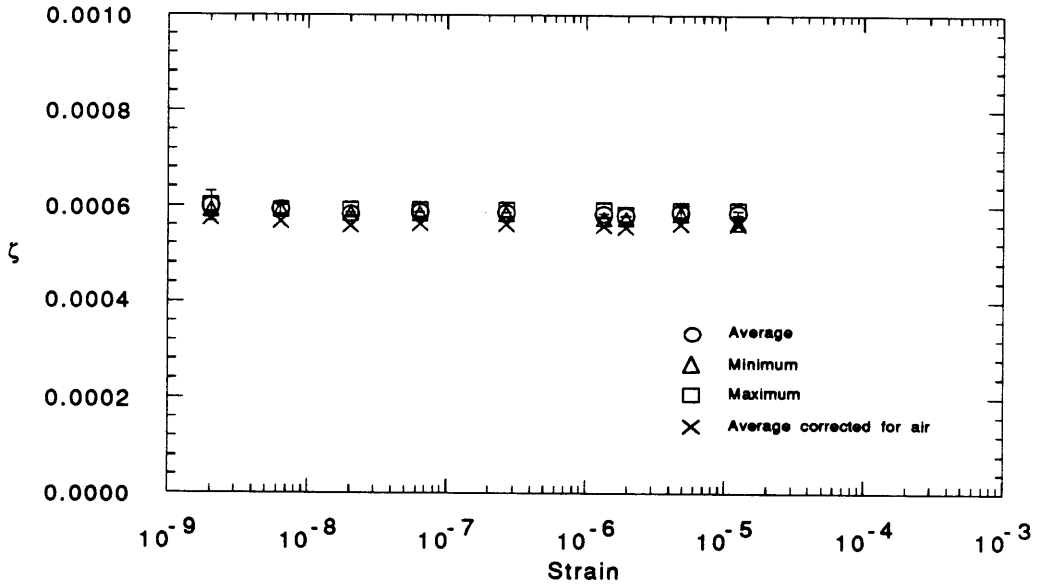

Figure 4.9 Damping in Third Mode of 1.3 m Al Bar in Air, f=50.6 Hz

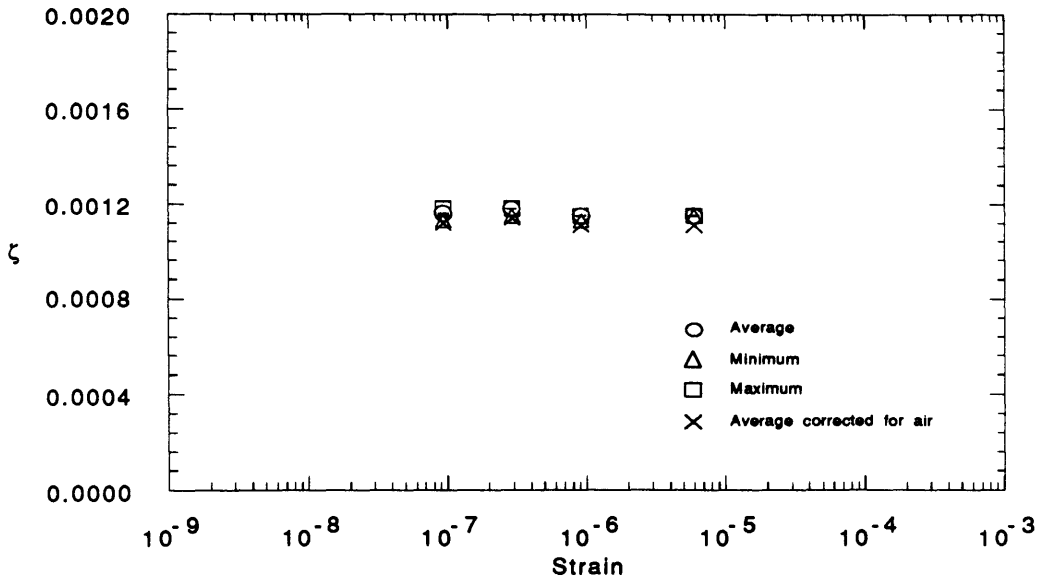

Figure 4.10 Damping in First Mode of 0.9 m Al Bar in Air, f=19.5 Hz

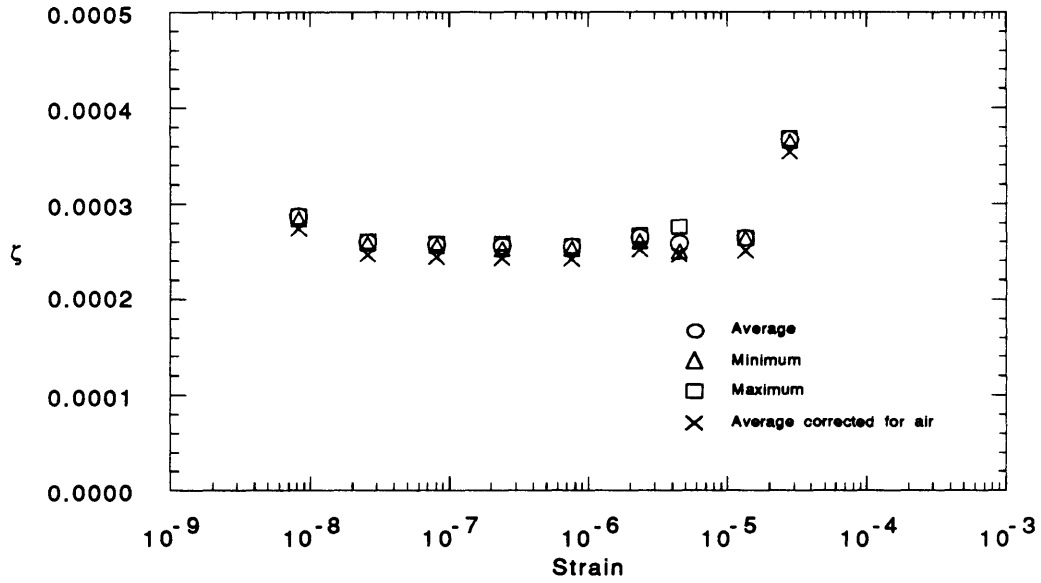

Figure 4.11 Damping in Second Mode of 0.5 m Al Bar in Air, f=173.6 Hz

Because of the simple rectangular geometry of the aluminum bars, the small strain experimental results can be compared to the damping from the thermoelastic model of metals derived by Zener [1948]. As discussed in Section 2.1, the model relates the internal damping of a structure to the heat flow arising from stress gradients in the structure. The damping ratio due to the anelastic effect is given by,

$$\zeta = \frac{\alpha^2 ET}{2C\rho}\left[\frac{\omega\tau}{1+\omega^2\tau^2}\right] \qquad [4.4]$$

where α is the coeffient of thermal expansion, E is the modulus of elasticity, T the absolute temperature, C the specific heat per mass, and ρ the density. From Equation 4.4, one can see that the frequency dependence of the damping has a peak at ω_r. The thermal relaxation time constant, τ, is the inverse of the Zener relaxation frequency,

$$\frac{1}{\omega_r} = \tau = \frac{h^2 C}{\pi^2 k}$$

which depends on the thickness, h, and the thermal conductivity, k. Using the thermal properties for a 3.2 mm thick 6061-T6 aluminum bar, Equation 4.4 is plotted against frequency in Figure 4.13. The constants used to plot Equation 4.4 are given in Appendix 4. The frequency is non-dimensionalized by the Zener relaxation frequency which, for a 3.2 mm bar is 9.91 Hz. Also shown in Figure 4.12 are the average values of experimental, low strain damping ratios corrected for air, as tabulated in Table 4.3.

The curve of the experimentally determined damping ratios measured at small strains shows a peak around 10 Hz, close to the peak of the Zener curve. Experimental values of ζ, measured above and slightly below this peak closely follow the Zener curve. This correlation is within the limits found from previous measurements [Mohr, 1982].

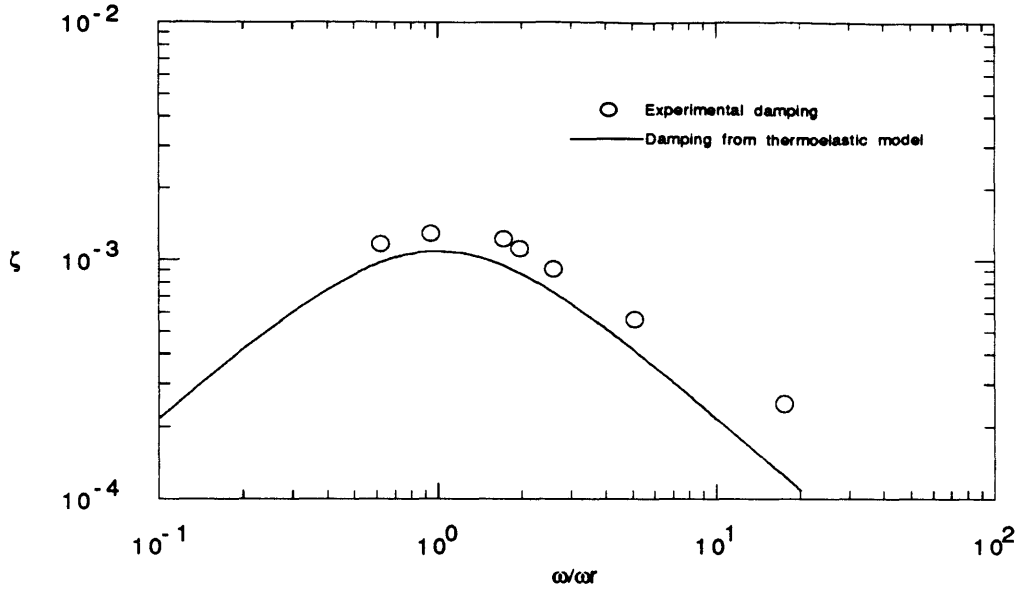

Figure 4.12 Theoretical and Experimental Damping Ratios Plotted vs. Non-Dimensional Frequency

Observation of the behavior of damping in aluminum bars at large strain levels was performed in vacuum to avoid damping due to aerodynamic drag at large amplitudes (Figs. 4.13 - 4.14). In Figure 4.13, the results from the tests of the first mode of the 0.5 m aluminum bar performed over a strain range from 0.707 με to 607 με are shown. An increase in damping with strain can be seen at strain levels above 10 με. This behavior can be correlated with a model developed for damping at large strains developed by Boser [1983].

Boser postulates that the dependence of damping on strain amplitude is caused by friction due to the motion of dislocations occuring during plastic deformation. At large strains, from about 100 με up, the damping of a structure is described by,

$$\zeta = \frac{4}{\pi}\frac{n_d b L}{F^2}\varepsilon \qquad [4.5]$$

where n_d is the mobile dislocation density, b is the Burgers vector for the given lattice structure, L is the dislocation segment, ε is the strain. F is given by,

$$F = \left[c\sqrt{1-c}\left(|A|(1+|Q|)/32\pi\right)\right]$$

where c is the solute concentration of the material and the quantity $|A|(1+|Q|)$ is a measure of the strength of the solute atoms, ranging from one to five [Boser, 1983]. The unknown quantity is the mobile dislocation density, which cannot be exactly determined *a priori*. The dislocation density, n_d, can be found using Equation 4.5, which can be used to validate the damping vs. strain relation. The slope of the strain dependent portion of Figure 4.13, on a linear scale starting from 10 με, found by performing a linear fit, is 3.78. Using this slope and the lattice properties for the face-centered cubic metal, 6061-T6 aluminum, Equation 4.5 yields a dislocation density of 1.74×10^6 cm^{-2}. This n_d is within the range 10^5 to 10^7 which is typical of metals [Ralls et al, 1976]. Constants used to calculate n_d are given in Appendix 4.

The second set of large strain measurements taken in vacuum from the 1.3 m long aluminum bar are presented in Figure 4.14. For the first mode, the measured damping ratios have an average value of 1.06×10^{-3} over the strain range from 0.608 με to 319 με. Because the average damping ratios are so large to begin with, no increase in damping with strain, which is on the order of 1×10^{-4} for the 0.5 m aluminum bar, can be seen.

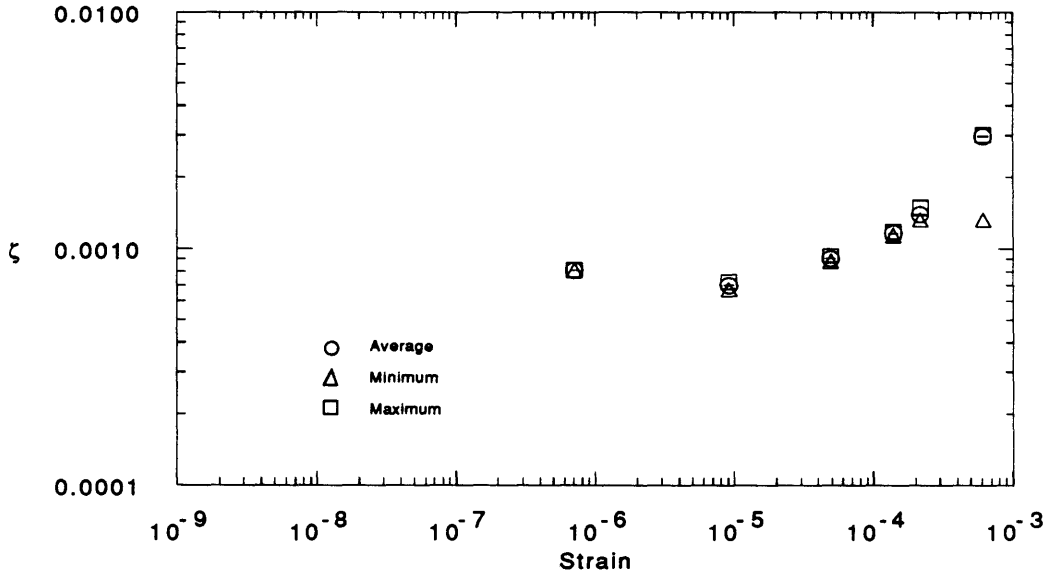

Figure 4.13 Damping in First Mode of 0.5 m Al Bar in Vacuum, f=58.1 Hz

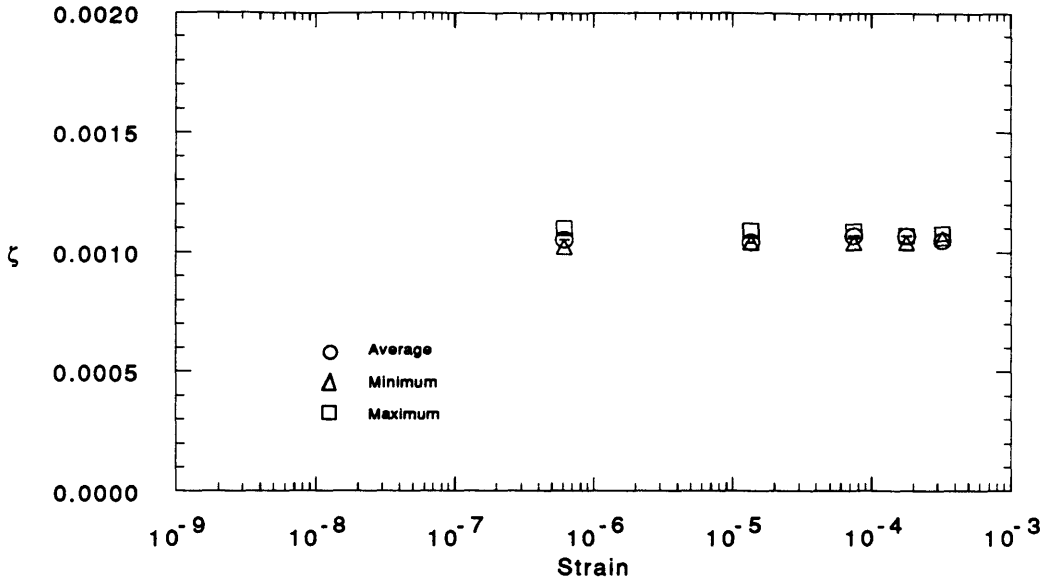

Figure 4.14 Damping in First Mode of 1.3 m Al Bar in Vacuum, f=9.23 Hz

4.2.2 Aluminum Tubes

Tests of the aluminum tubes, which were constructed from the same material as the aluminum bars, 6061-T6, were performed to show the effects of a change in the test specimen geometry on damping. A total of four modes of the two tubes were tested in air, but only one mode from each tube was tested down to nanostrain levels. The lowest strain levels achieved were slightly higher than the levels reached with the other material damping specimens, about 10 nε. Average small strain damping ratios measured in, and corrected for air are given in Table 4.4 and plotted against frequency in Figure 4.15. Results from each of these tests are plotted against strain in Figures 4.16 - 4.17. Results of tests at larger strains performed in vacuum are displayed in Figure 4.18.

Table 4.4 Summary of Average Small Strain Damping From Al Tubes Corrected For Air

Test Specimen	Frequency (Hz)	Strain Independent Range	Corrected Average Damping Ratio, ζ
0.9 m Al tube	185.2	10.8 nε - 78.9 με	5.46×10^{-5}
0.9 m Al tube	510.3	1.10 με - 11.1 με	1.17×10^{-4}
0.7 m Al tube	308.1	20.9 nε - 19.6 με	1.11×10^{-4}
0.7 m Al tube	829.5	.487 με	5.89×10^{-5}

Generally, the damping ratios of the aluminum tubes, shown in Figure 4.15, are much lower than the damping ratios of the aluminum bars. Unlike the aluminum bar results, the damping ratios display only a small dependence on frequency. One possible explanation is that the natural frequencies of the tubes are so high that the damping results are far higher than the frequency of any thermoelastic effects. Another possibility is that the origin of the slight peak in the damping curve is from higher order thermoelastic effects. However, the damping mechanism of metal tubes is not well understood and it is possible that the damping of the aluminum tubes is not due to thermoelastic effects at all. Rather, it may be due to some more underlying effect in the range of $\zeta = 10^{-4}$. Postulating such an underlying effect would also explain the slight disparity between the aluminum bar damping and the Zener model at higher frequencies as shown in Figure 4.12.

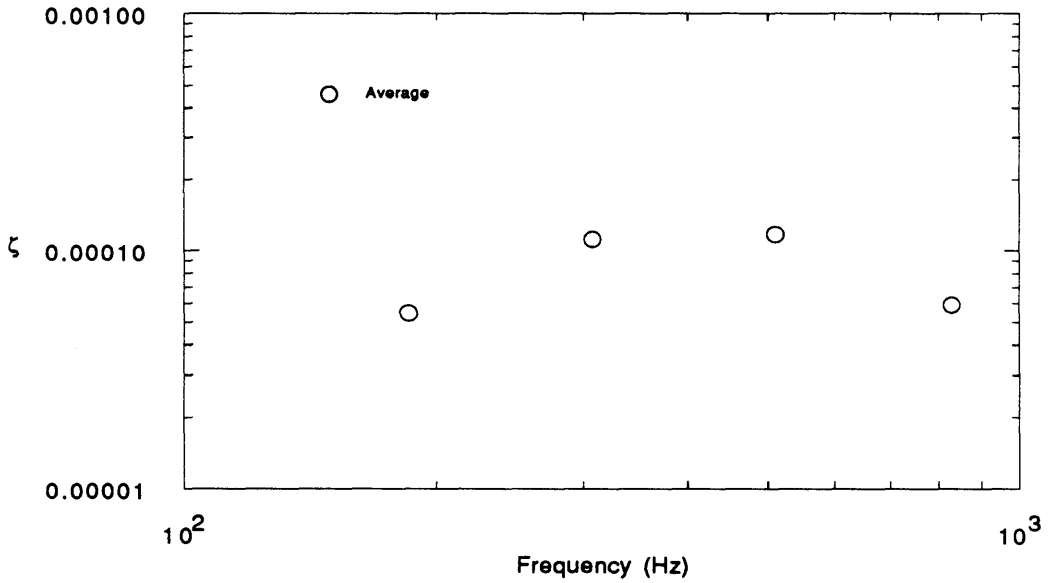

Figure 4.15 Average Small Strain Aluminum Tube Damping vs. Frequency

The damping ratios of the first mode of the 0.9 m aluminum tube, plotted against strain in Figure 4.16, show little dependence on strain up to 78.9 με with an average value given in Table 4.4. As one can see in Figure 4.16, at such high frequencies, the uncertainty due to noise is small, within the scatter in the data. However, since the average damping ratios are so

small, the correction due to air damping is noticeable, up to 21 % of the average. An increase in the damping ratio to 1.08×10^{-4}, shown by the point at 376 με, can be attributed to a combination of plasticity effects and aerodynamic drag. The contribution from drag, found using Equation 4.3 is roughly 1×10^{-5}. Since the damping of the tube exhibited little dependence on damping in the first mode, only two measurements of the second mode damping, at 1.1 and 11 με, were made to determine the frequency dependence of tube damping. The average damping for these two points are given in Table 4.4.

Results of the tests of the first mode of the 0.7 m aluminum tube in both air and vacuum are plotted in Figures 4.17 - 4.18. The damping ratios measured in air, shown in Figure 4.17, display a behavior nearly identical to that of the 0.9 m tube. With very little noise or scatter, the damping ratios measured in air show little dependence on strain up to 19.6 με, with an average value given in Table 4.4. An increase in damping is displayed by the point at 71.1 με up to a corrected value of 1.79×10^{-4}. Also given in Table 4.4 is the value of a single measurement of the damping ratio of the second mode of the tube.

An increase in damping was also shown in tests in vacuum at larger strain levels (Fig. 4.18). Like the aluminum bars, the damping ratios of the 0.7 m aluminum tube show a nearly linear increase with strain from 45.6 με to 553 με. A line fit to this portion of the curve has a slope of 0.639. The implied value of the dislocation density, obtained using Equation 4.5, is 2.94×10^{5} cm^{-2}, lower than the value found for the aluminum bars, but still within the typical bounds for metals.

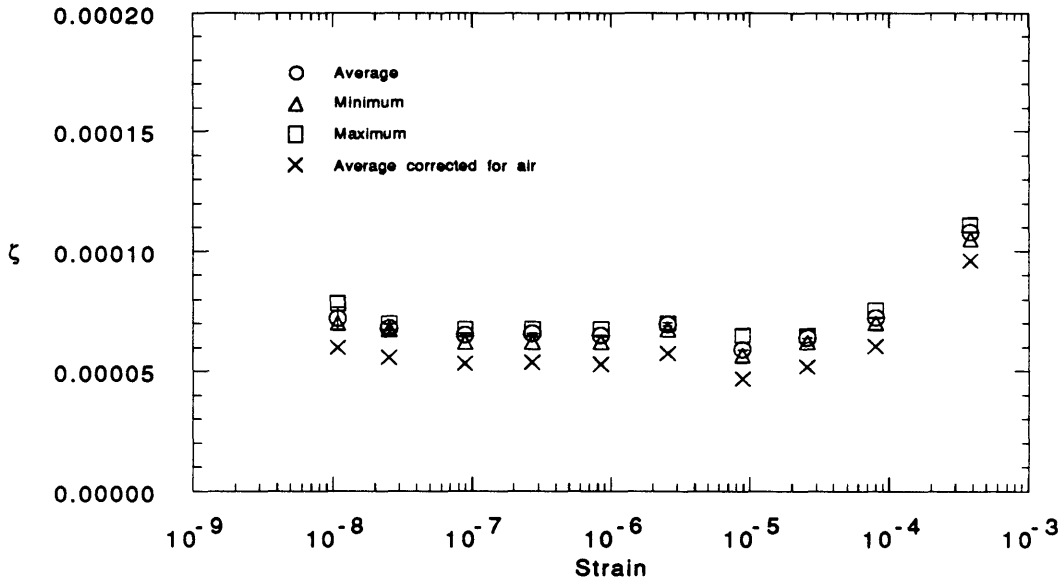

Figure 4.16 Damping in First Mode of 0.9 m Aluminum Tube in Air, f=185.1 Hz

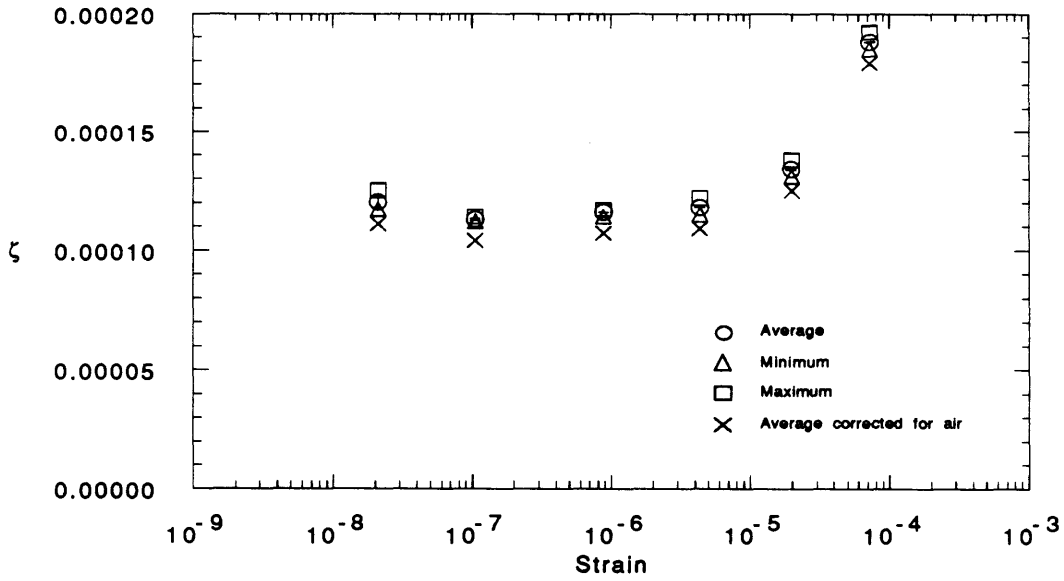

Figure 4.17 Damping in First Mode of 0.7 m Aluminum Tube in Air, f=308.1 Hz

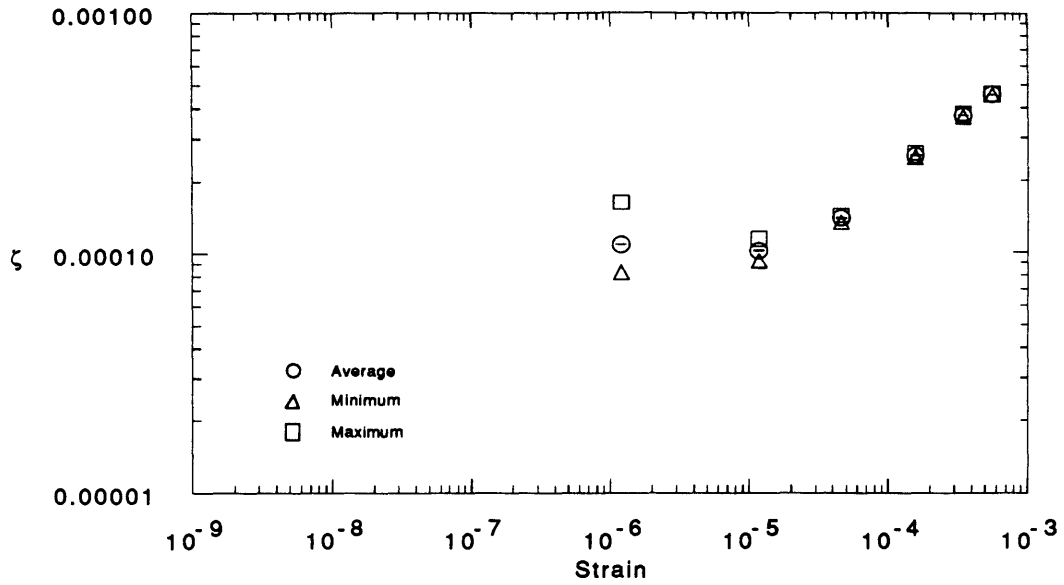

Figure 4.18 Damping in First Mode of 0.7 m Aluminum Tube in Vacuum, f=308.8 Hz

4.2.3 Graphite/Epoxy Bars with $[0]_{24}$ Layup

Tests of the $[0]_{24}$, or uniply Gr/Ep bars were performed to determine the damping behavior of graphite/epoxy bars with a rectangular cross section. These results were then compared with models of the damping of uniply laminates developed by Hashin [Ashton et al, 1969] and Adams and Bacon [1973]. A total of four modes from the two bars were tested in air in the small strain range. The averages of the corrected damping ratios obtained from these tests at low strain levels are summarized in Table 4.5. In Figures 4.19 - 4.22, the damping ratios from these tests are plotted against strain.

Table 4.5 Summary of Average Small Strain Damping From Uniply Gr/Ep Bars Corrected For Air

Test Specimen	Frequency (Hz)	Strain Independent Range	Corrected Average Damping Ratio, ζ
0.9 m Uniply bar	30.9	3.63 nε - 78.9 με	2.88×10^{-4}
0.9 m Uniply bar	83.5	.863 nε - 41.6 με	3.35×10^{-4}
0.7 m Uniply bar	56.9	2.46 nε - 238. με	2.56×10^{-4}
0.7 m Uniply bar	156.7	1.02 nε - 83.8 με	2.98×10^{-4}

In Figures 4.19 - 4.20, the damping ratios from the first and second modes of the 0.9 m long graphite/epoxy uniply bar are plotted vs. strain. The results show little scatter or uncertainty due to noise. Since the bars are relatively light, the effect of air is greater than that on the aluminum bars. Neither set of damping ratios show any dependence on strain at low strain levels and have average values given in Table 4.5.

The 0.7 m long bar displays a behavior similar to that of the 0.9 m bar (Figs. 4.21 - 4.22). The damping ratios of the first two modes show little dependence on strain at small strains, with average values given in Table 4.5. At strain levels from 10 με up, the damping ratios from the second mode show a slight upturn. The mechanism behind this increase is probably due to viscoelastic behavior of the matrix rather than movement of dislocations, as in the aluminum damping specimens.

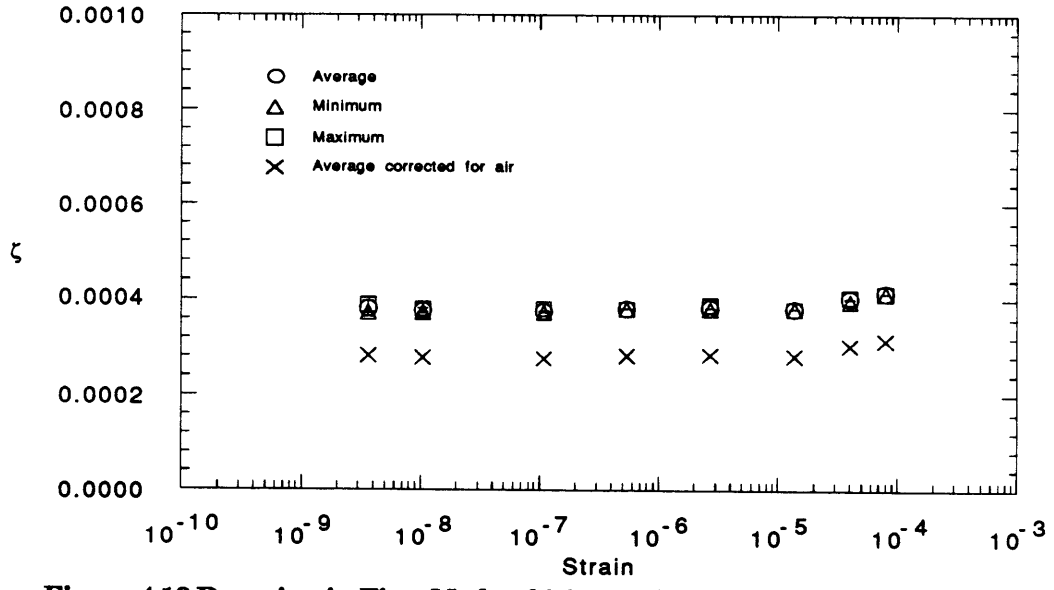

Figure 4.19 Damping in First Mode of 0.9 m Uniply Bar in Air, f=30.9 Hz

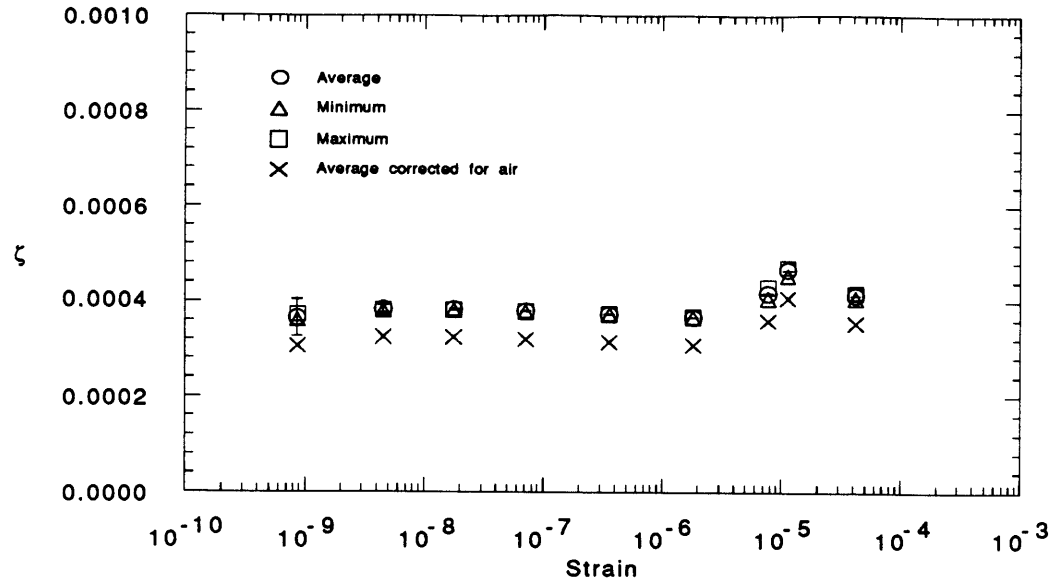

Figure 4.20 Damping in Second Mode of 0.9 m Uniply Bar in Air, f=83.5 Hz

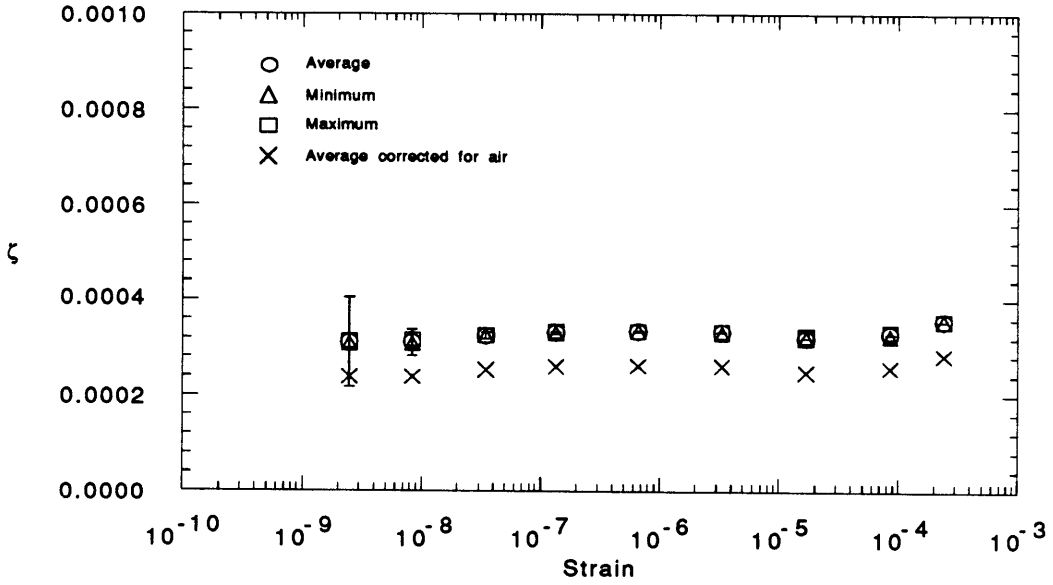

Figure 4.21 Damping in First Mode of 0.7 m Uniply Bar in Air, f=56.9 Hz

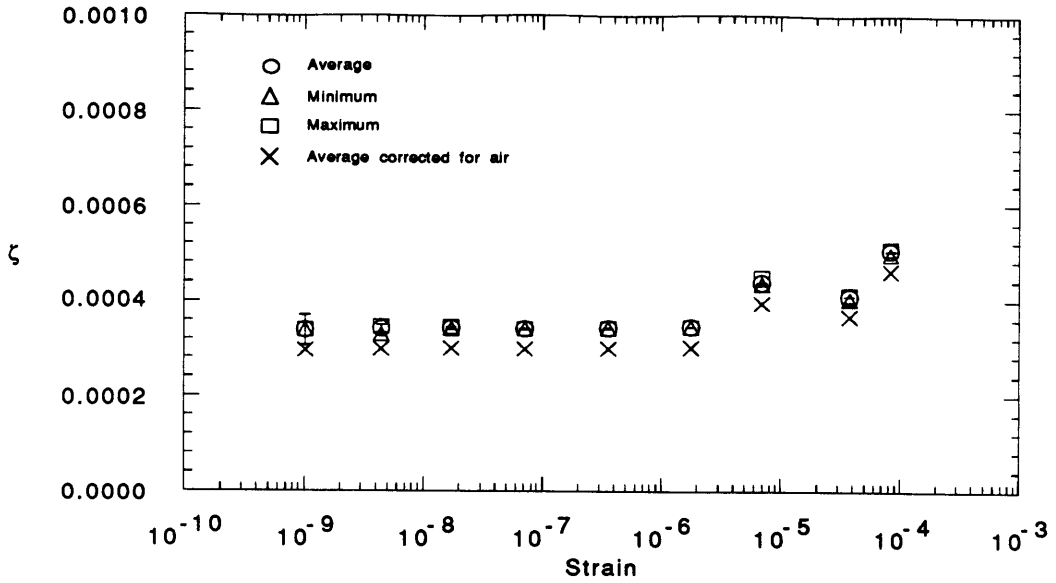

Figure 4.22 Damping in Second Mode of 0.7 m Uniply Bar in Air, f=156.7 Hz

Because of the simple geometry and layup of the uniply bars, comparisons of the small strain experimental results can be compared with the theoretical model of damping derived by Hashin [Ashton et al, 1969] and Adams and Bacon [Adams and Bacon, 1973]. The damping from this model has two parts -- one part due to axial vibration and one part due to shear, and is given by,

$$\zeta_t = \zeta_A + \zeta_S \qquad [4.6]$$

where ζ_A, the axial component [Ashton et al, 1969] is given by,

$$\zeta_A = \frac{\zeta_m}{\frac{E_f V_f}{E_m V_m} + 1} \qquad [4.7]$$

ζ_m is the damping ratio of the matrix, E_f the modulus of the fibers, V_f the volume fraction of the fibers, E_m the modulus of the matrix, and V_m is the volume fraction of the matrix. The shear component is given by,

$$\zeta_S = \frac{\zeta_{12} \int_0^{1/2} \left[\frac{\partial^3 w}{\partial x^3}\right]^2 dx}{\int_0^{1/2} \left[\frac{\partial^3 w}{\partial x^3}\right]^2 dx + \frac{10 G_{12}}{E_m h^2} \int_0^{1/2} \left[\frac{\partial^2 w}{\partial x^2}\right]^2 dx} \qquad [4.8]$$

where w is the lateral deflection of the bar, x is the distance from the end of the bar, l the length of the bar, G_{12} is the shear modulus of the laminate, h is the thickness of the bar, and ζ_{12} is the shear damping of the matrix. ζ_{12} is given by,

$$\zeta_{12} = \frac{\zeta_m(1+V_f)\left[(G+1)^2 + V_f(G-1)^2\right]}{\left[G(1+V_f)+1-V_f\right]\left[G(1+V_f)+1+V_f\right]}$$

where G is the ratio of the shear modulus of the fiber to the shear modulus of the matrix. Assuming a spatially sinusoidal mode shape and using the properties for the AS4/3501-6 graphite/epoxy bars [Roylance et al, 1983], the damping ratio is found to be nearly independent of frequency and strain, with a value of 1.92 x 10-4. The constants used to calculate this value are given in Appendix 4.

In Figure 4.23, the values of ζ from Equations 4.6 - 4.8 are plotted against frequency along with the average experimentally determined damping ratios tabulated in Table 4.5. The experimentally measured damping ratios, on the order of 10^{-4}, compare well with the theoretical values, within the limits of the reproducibility of the experiments. The experimentally measured values of ζ are nearly independent of frequency, as predicted by the model. Differences between the experimental and predicted damping ratios are probably due to two reasons. First, the values used to calculate the theoretical damping ratios may not precisely represent the properties of the bars tested -- the volume fractions or the matrix properties could be slightly different. Second, there may be slight differences between each of the bars due to manufacturing defects which are difficult to quantify.

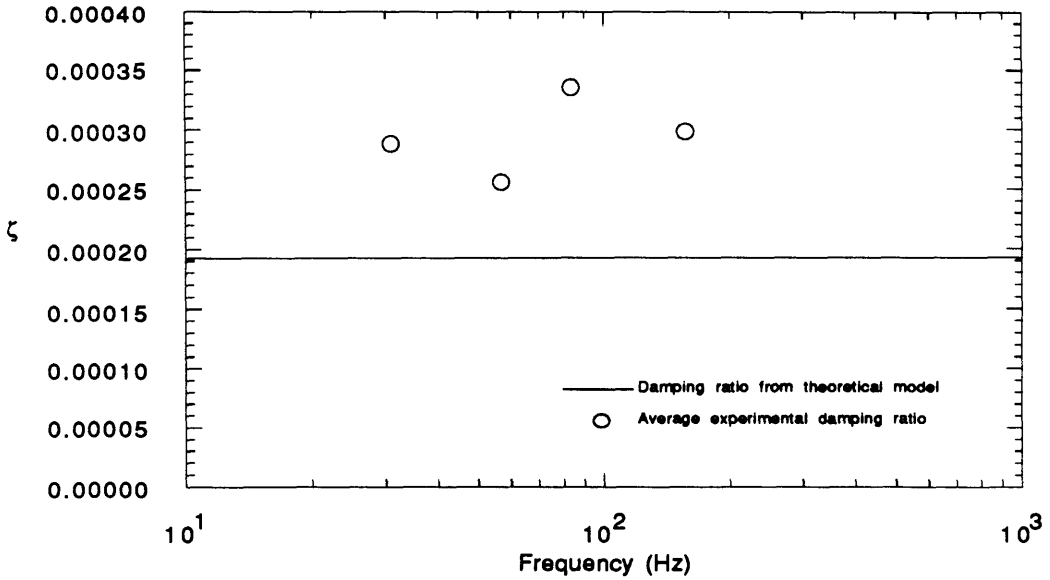

Figure 4.23 Average Uniply Graphite/Epoxy Bar Damping Ratio vs. Frequency

4.2.4 Graphite/Epoxy Bar With $[\pm 15]_{6s}$ Layup

Testing of the graphite/epoxy bars with a $[\pm 15]_{6s}$ layup, with a coefficient of thermal expansion of zero (0 CTE), was performed to characterize the damping of a graphite/epoxy laminate with a layup that might be used in an astronomical instrument. A total of four modes of the two bars were tested at small strains in air. Results were compared with results from the uniply bars to determine the relation between damping and layup. A summary of the averages of the corrected results is presented in Table 4.6.

Table 4.6 Summary of Average Small Strain Damping from $[\pm 15]_{6s}$ Gr/Ep Bars Corrected For Air

Test Specimen	Frequency (Hz)	Strain Independent Range	Corrected Average Damping Ratio, ζ
0.9 m 0 CTE bar	33.2	40.3 nε - 3.63 με	6.24×10^{-4}
0.9 m 0 CTE bar	90.8	.587 nε - 4.20 με	7.03×10^{-4}
0.9 m 0 CTE bar	287.5	3.08 nε - 162 με	1.11×10^{-3}
0.7 m 0 CTE bar	53.1	1.96 nε - 5.76 με	6.33×10^{-4}
0.7 m 0 CTE bar	145.0	.899 nε - 148 με	7.48×10^{-4}

Generally, the damping of the bars with the $[\pm 15]_{6s}$ layup, whose corrected averages are shown vs. frequency in Figure 4.24, is three to four times higher than that of the bars with the pure uniply layup. A comparison of the average damping of the first modes of the 0.9 m bars with different layups show that the bar with the $[\pm 15]_{6s}$ layup produces a damping ratio 3.9 times higher than the uniply bar. This increase is consistent with earlier work [Sheen, 1983], which has shown that damping ratio increases with the angle orientation of a laminate. Also consistent with previous results, the damping ratios of the bars appear relatively insensitive to frequency, with a slight increase in damping at high frequency.

In Figures 4.25 - 4.26, results from the tests of second and fourth modes of the 0.9 m long Gr/Ep bars with a $[\pm 15]_{6s}$ or 0 CTE layup are presented. At the smallest strains the uncertainty is significant -- as large as 4.20×10^{-4}, or 55% of the value of the damping ratio of the second mode. Like the damping of the uniply bars, the damping of the 0 CTE bars show little dependence on strain, with average values given in Table 4.6. Three measurements of the damping of the first mode of the 0.9 m bar, also shown in Table 4.6, are not shown as a separate plot against strain.

Shown in Figures 4.27 - 4.28 are the results from the tests of the first and second modes of the 0.7 m Gr/Ep bar. Displaying little uncertainty and inaccuracy, neither mode exhibits any change in damping with strain and have average values given in Table 4.6.

Tests of the 0.9 m long bar were also performed at larger strain levels in vacuum. The results of these tests are shown in Figure 4.29. The 0.9 m long $[\pm 15]_{6s}$ bar, shows only a small increase in damping at strains up to 1490 $\mu\varepsilon$.

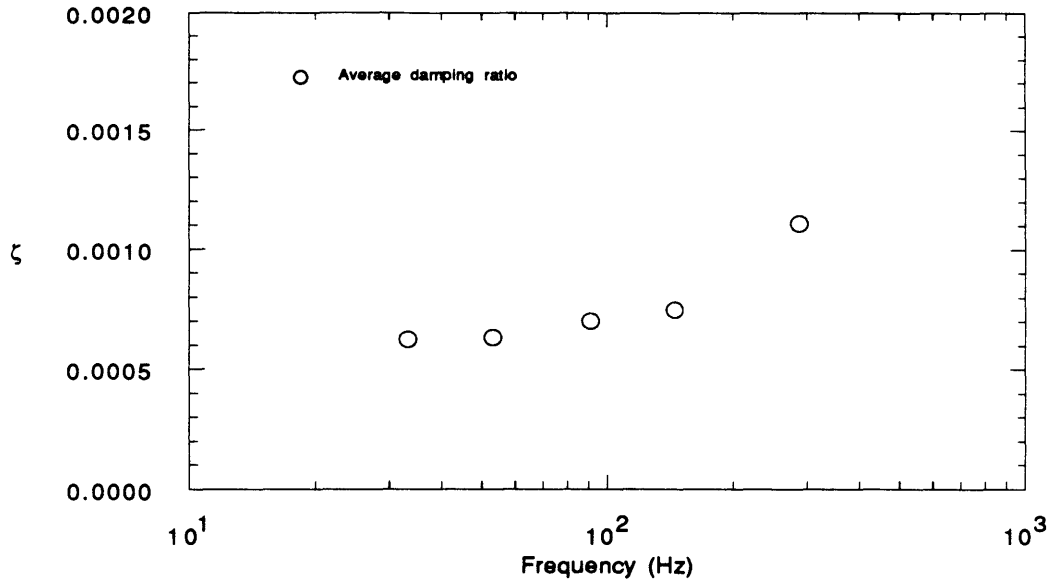

Figure 4.24 Average Damping Ratio of 0 CTE Gr/Ep Bars vs. Frequency

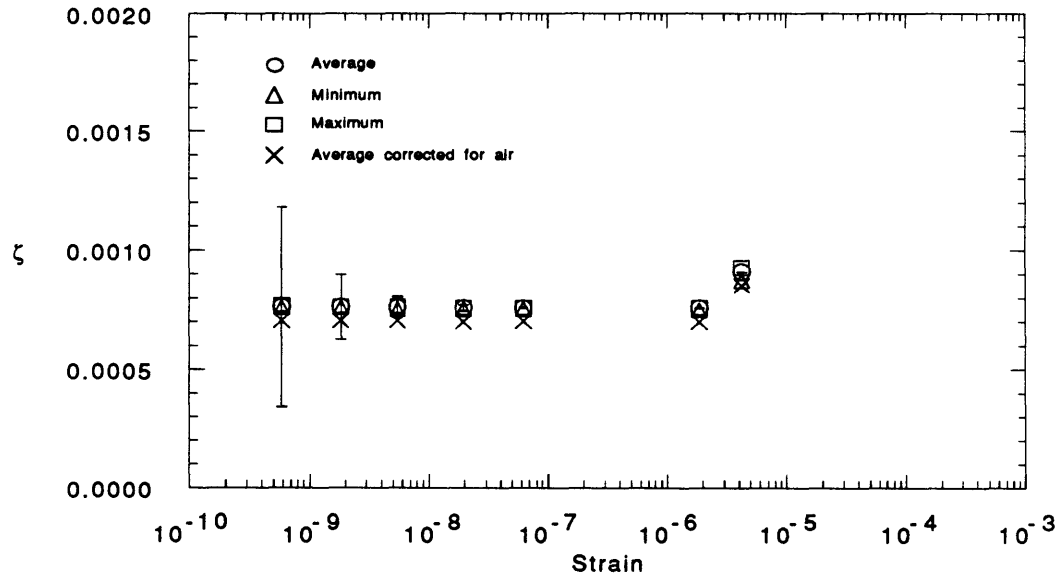

Figure 4.25 Damping in Second Mode of 0.9 m 0 CTE Gr/Ep bar in Air, f=90.8 Hz

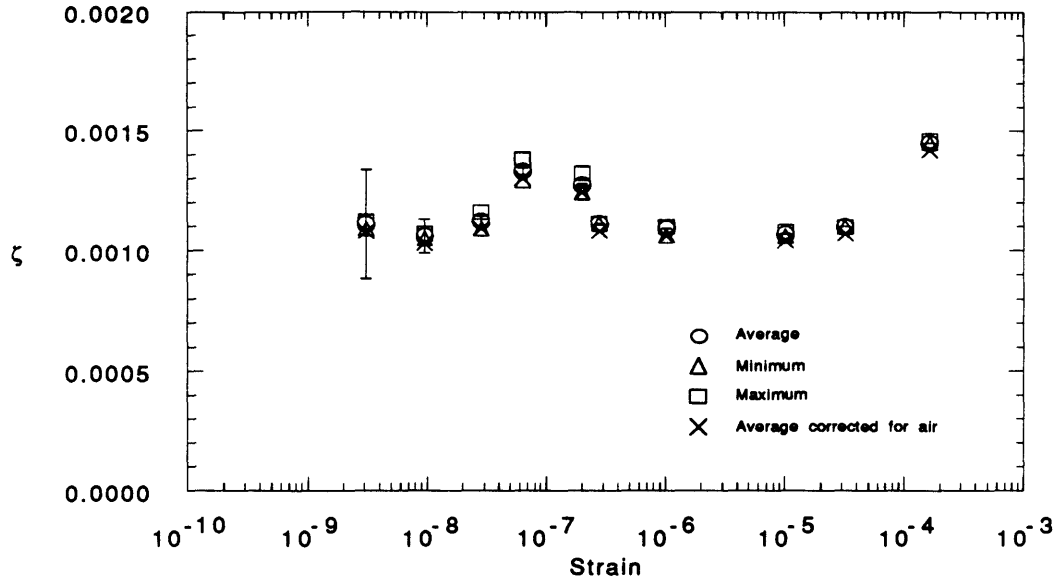

Figure 4.26 Damping in Fourth Mode of 0.9 m 0 CTE Gr/Ep Bar in Air, f=287.5 Hz

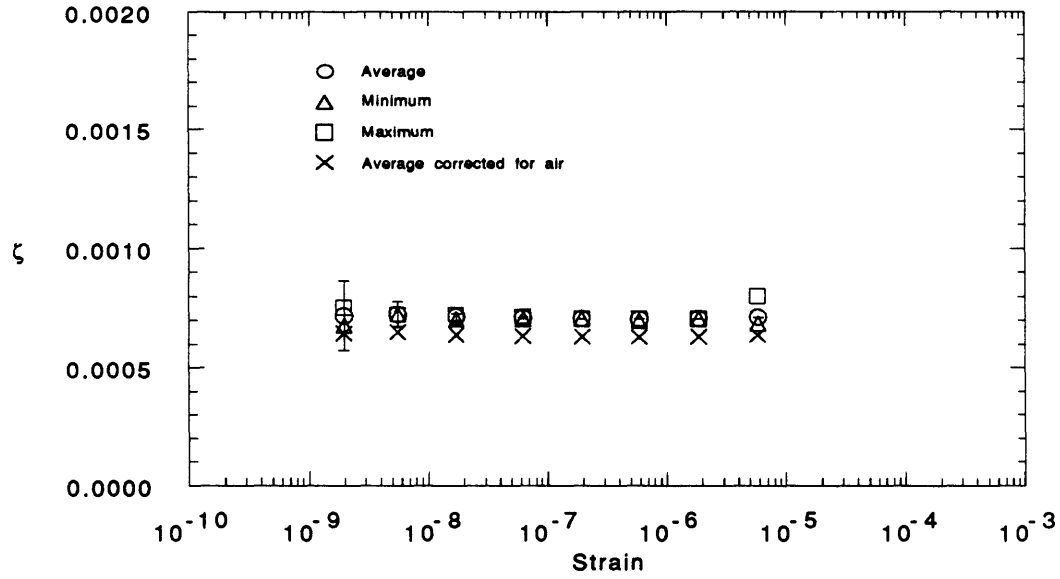

Figure 4.27 Damping in First Mode 0.7 m 0 CTE Gr/Ep Bar in Air, f=53.1 Hz

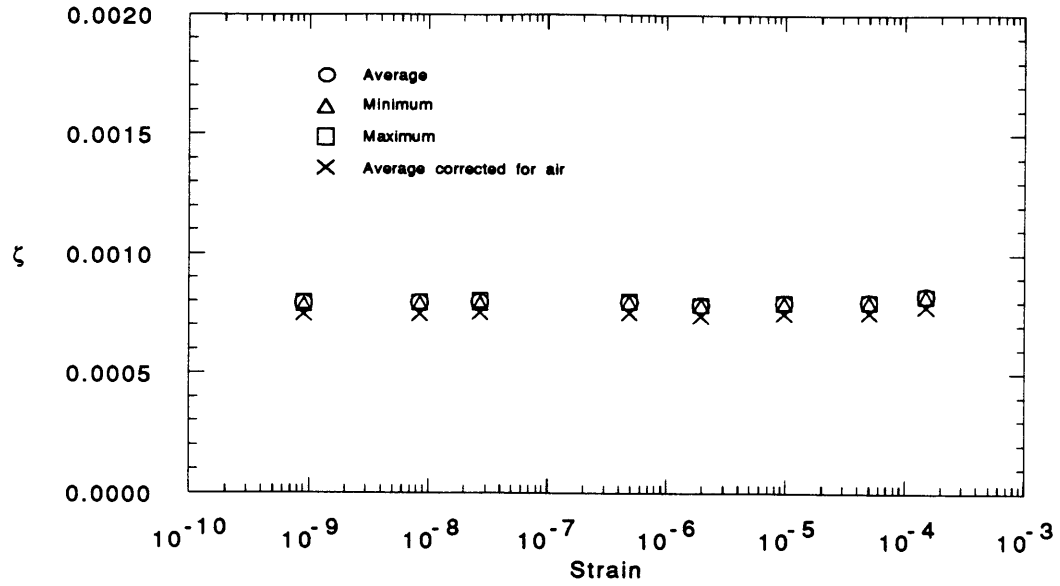

Figure 4.28 Damping in Second Mode of 0.7 m 0 CTE Gr/Ep Bar in Air, f=145.0 Hz

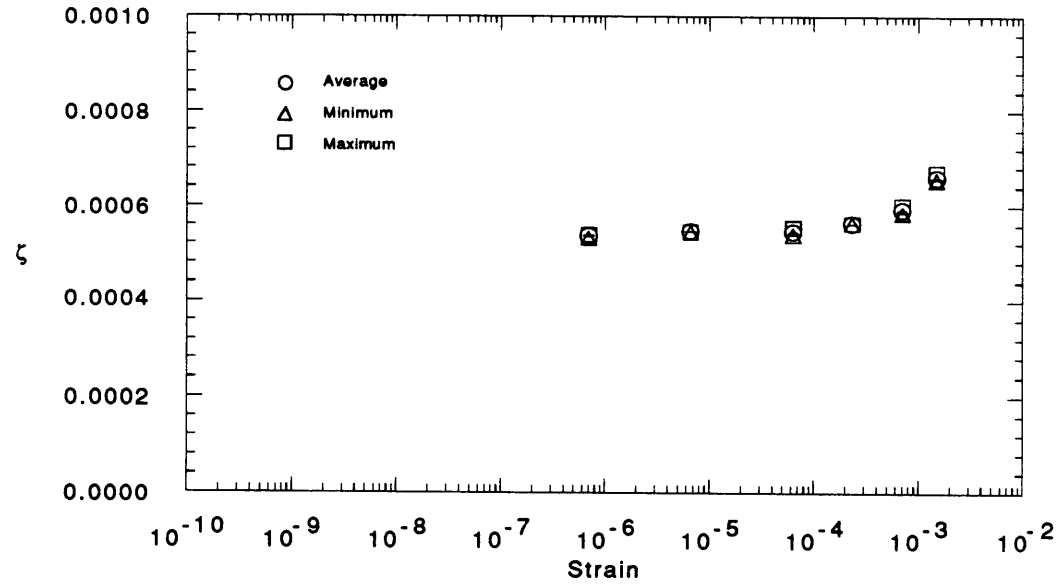

Figure 4.29 Damping in First Mode of 0.9 m 0 CTE Gr/Ep Bar in Vacuum, f=32.0 Hz

4.2.5 Graphite/Epoxy Tubes With $[\pm 15]_{3S}$ Layup

The two tubes with a $[\pm 15]_{3S}$ or 0 CTE layup were tested to determine the change in damping in a Gr/Ep laminate due to a change in geometry. Average damping ratios from the two tubes are given in Table 4.7. The results from each set of tests in air are plotted against strain and presented in Figures 4.30 - 4.31. Results from tests performed in vacuum are given in Figure 4.32.

Table 4.7 Summary of Average Small Strain Damping From $[\pm 15]_{3S}$ Gr/Ep Tubes Corrected For Air

Test Specimen	Frequency (Hz)	Strain Independent Range	Corrected Average Damping Ratio, ζ
0.9 m Gr/Ep tube	275.0	4.20 nε - 1.94 με	2.93×10^{-3}
0.7 m Gr/Ep tube	503.0	3.76 nε - 9.58 με	1.28×10^{-3}

Generally, the damping of the $[\pm 15]_{3S}$ tubes is higher than that of the bars with the same type of layup and twice the number of plies. A possible explanation for this increase is a higher matrix volume fraction for the tubes than for the bars due to differences in the manufacturing process. Since there are only two sets of measurements of damping ratios, the relation between damping and frequency cannot be clearly seen. It should be noted, however, that the measured damping in the $[\pm 15]_S$ Gr/Ep bars and tubes is of the same order of magnitude, within a factor of 2 or 3, whereas the damping in the aluminum bars and tubes is more than an order of magnitude appart. This suggests that the same loss mechanism is present in the Gr/Ep bars and tubes, but different loss mechanisms are present in the aluminum bars and tubes.

In Figure 4.30 the results from the tests of damping of the first mode of the 0.9 m tube are presented. Results show little scatter and uncertainty. For the first mode, with a low strain average given in Table 4.7, the damping shows a large increase to a value of ζ of 1.48×10^{-2} at 46.4 με. This increase starts at a slightly lower strain level than the results from the other material damping specimens and could be due to manufacturing defects. Predictions of the damping due to drag from Equation 4.3, show that the damping ratio due to air at 100 με is roughly 1×10^{-5}, eliminating drag damping as a possible explanation.

In Figure 4.31, the damping ratios obtained from the tests of the 0.7 m tube are plotted vs. strain. A moderate increase in damping with strain appears to begin at 9.58 με, roughly the same strain level at which the increase in damping of the 0.9 m tube begins. For strains below 3.76 nε to 9.58 με, the damping appears insensitive to strain with an average value given in Table 4.7.

The 0.7 m tube was also tested at larger strains in vacuum (Fig. 4.32). In the lower strain level, up to a strain of 100.6 με, the damping appears to be constant with an average value of 1.00 x 10-3, roughly the same as the value obtained in air. At larger strains, up to 596 με, the damping increases slightly with strain.

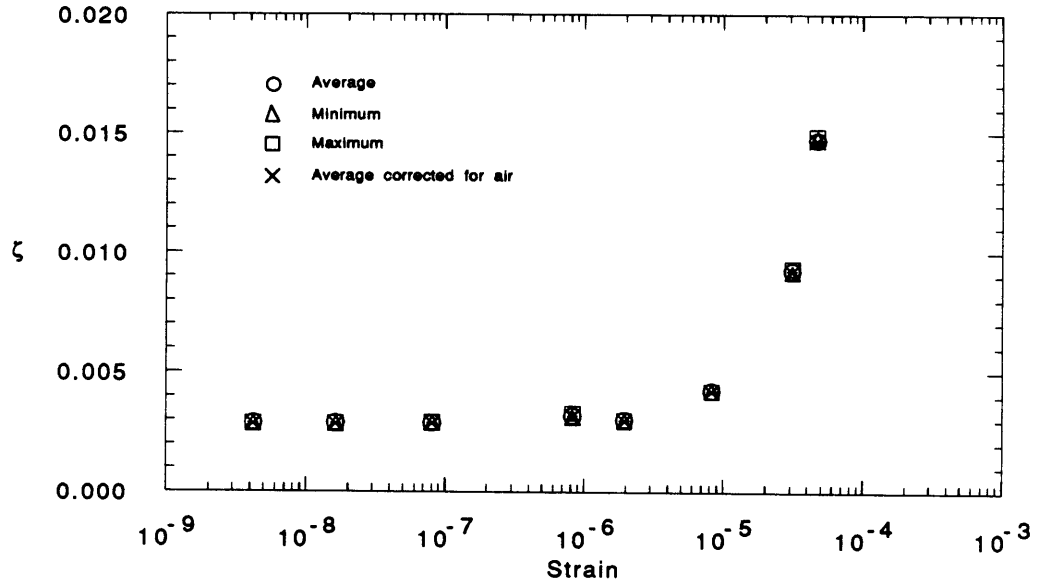

Figure 4.30 Damping in First Mode of 0.9 m $[\pm 15]_{3s}$ Gr/Ep Tube in Air, f=274.9 Hz

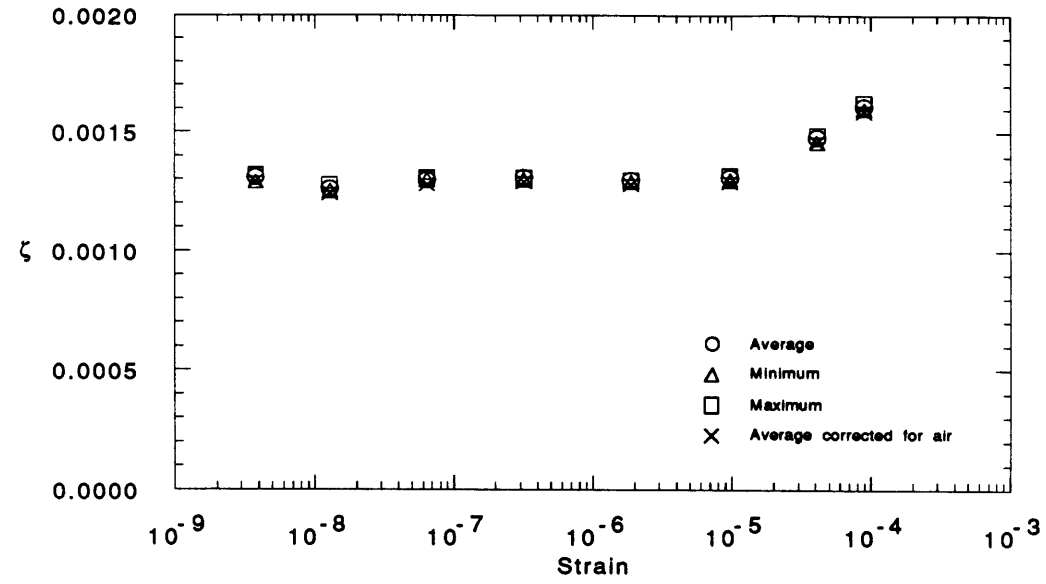

Figure 4.31 Damping in First Mode of 0.7 m $[\pm 15]_{3s}$ Gr/Ep Tube in Air, f=503.0 Hz

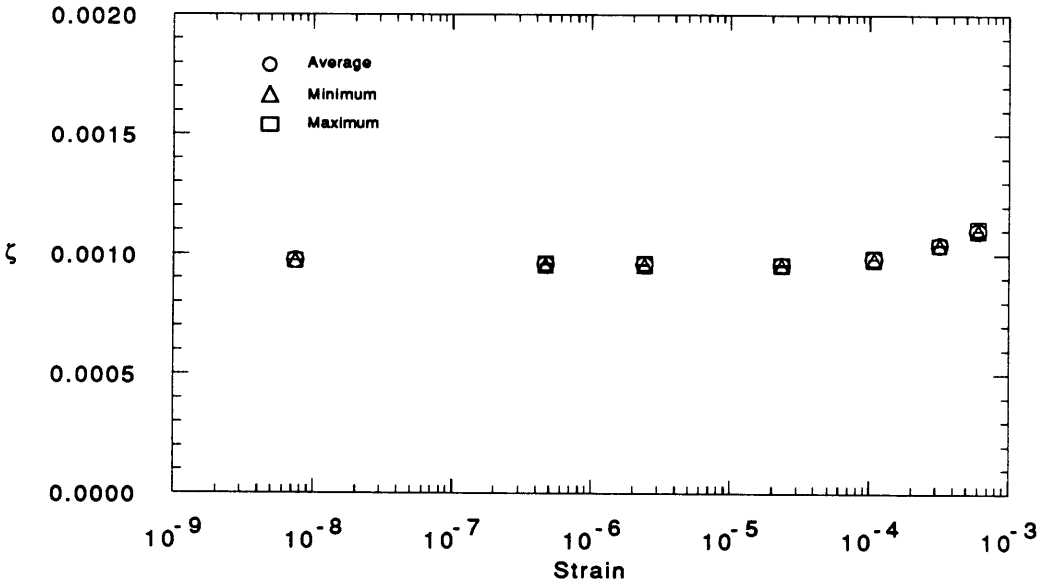

Figure 4.32 Damping in First Mode of 0.7 m $[\pm 15]_{3s}$Gr/Ep Tube in Vacuum, f=500.8 Hz

4.3 Structural Damping Results

To obtain values of structural damping ratios, three modes of the interferometer testbed were tested. The source of damping of the testbed was assumed to be due to two sources -- material damping and joint damping. Like the tests described in the previous section, separate tests were performed to determine damping at small strains below 1 με and large strains above 1 με. Because of limitations of the actuators used, large strain tests were limited to strains below 100 με. The averages of the small strain damping ratios from each mode are summarized in Table 4.8. Damping ratios found from each set of tests are plotted against strain in Figures 4.33 - 4.38. Because of the complicated geometry of the testbed, no corrections are made for air effects.

Table 4.8 Summary of Average Small Strain Damping From Testbed

Mode Number	Frequency (Hz)	Strain Independent Range	Average Damping Ratio, ζ
1	44.1	1.29 nε - .926 με	5.76×10^{-4}
2	40.0	2.02 nε - 1.79 με	7.16×10^{-4}
3	55.4	2.62 nε - 2.50 με	6.49×10^{-4}

In Figures 4.33 - 4.34, the damping ratios of the mode with the resonant frequency at 44.1 Hz, designated Mode #1 in Table 4.8, are plotted against strain. Figure 4.33 shows the damping obtained using the piezoelectric actuator at low strains. The damping ratio at the lowest strain level shows an uncertainty in ζ of 1.39×10^{-4} due to mechanical noise. With an average value of ζ of 5.76×10^{-4} over the small strain range (Table 4.8), the damping shows little variation with strain. Since the testbed is made up of aluminum tubes and joints, and the measured damping of the testbed is an order of magnitude larger than that found in the aluminum tubes, it can be inferred that the primary source of this loss is in the joints and attachments.

Figure 4.34 contains a plot of the damping ratios at larger strains, obtained using the DC motor as a proof mass actuator. The addition of the proof mass actuator caused a slight drop in the frequency of the mode to 43.9 Hz and also increased the noise and damping in the smallest achievable strain region (Fig. 4.34). With the proof mass actuator, the

lowest damping ratio is 6.42×10^{-4} compared to the small strain average of 5.76×10^{-4} given above in Table 4.8. Over a range of strain from 0.532 με to 26.0 με, the values of ζ increase to 7.69×10^{-4}. One of the causes of this increase is probably slight non-linearity in the attachments. Other causes could be aerodynamic and acoustic effects.

The results of the tests of the global truss mode with a resonant frequency of 40.0 Hz, designated Mode #2, are shown in Figure 4.35 - 4.36. Like the damping of Mode #1, the plot of damping vs. strain in the small strain region shown in Figure 4.36, displays little change in damping with strain. The average value of ζ over the small strain range from Table 4.8, is 7.16×10^{-4}. The damping ratios measured in the larger strain range (Fig. 4.36), from 0.275 με to 102 με, show an increase similar to that of Mode #1, from 8.65×10^{-4} to 1.07×10^{-3} at a slightly lower frequency, 38.9 Hz.

Damping from Mode #3, at 55.4 Hz, is shown in Figures 4.37 -4.38. The damping ratios from Mode #3 display the same behavior as Modes #1 and #2. At small strains, the damping ratios have an average value of 6.49×10^{-4} over the strain range given in Table 4.8. Tests of damping with the proof mass actuator, shown in Figure 4.38, display an increase in damping ratio from 1.03×10^{-3} at 0.381 με to 1.24×10^{-3} at 36.7 με with a drop in frequency from 55.4 Hz to 54.4 Hz.

As a result of these tests, it can be inferred that the damping of the interferometer precision truss is dominated by the loss at the joints and attachments. The average damping, ζ of the truss found using the piezoceramic actuator is on the order of 7×10^{-4}. Addition of the proof mass actuator caused a slight increase in damping.

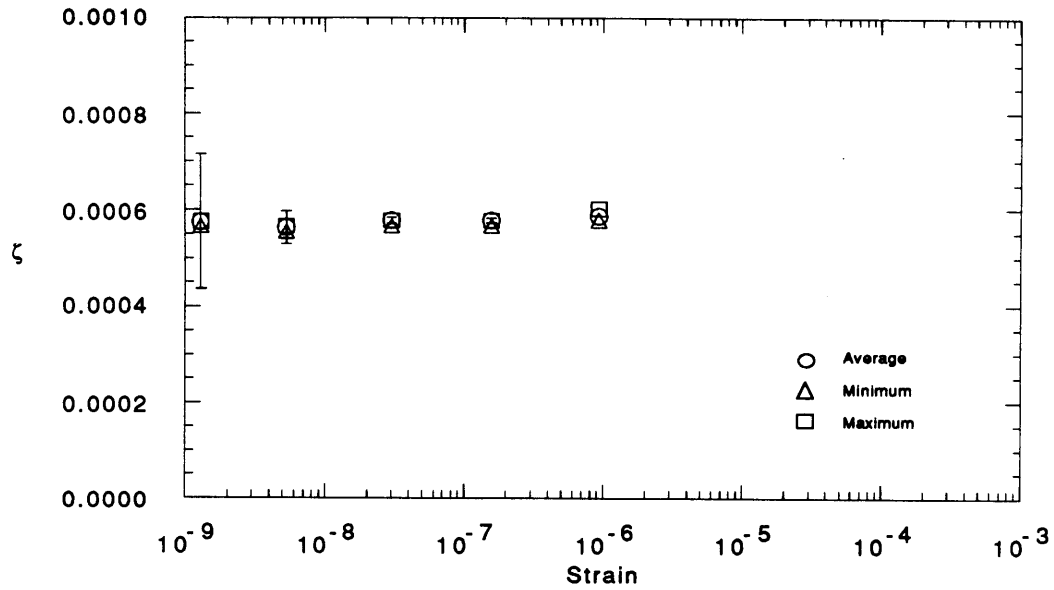

Figure 4.33 Damping in Mode #1 of Testbed, f=44.1 Hz, Small Strain Range

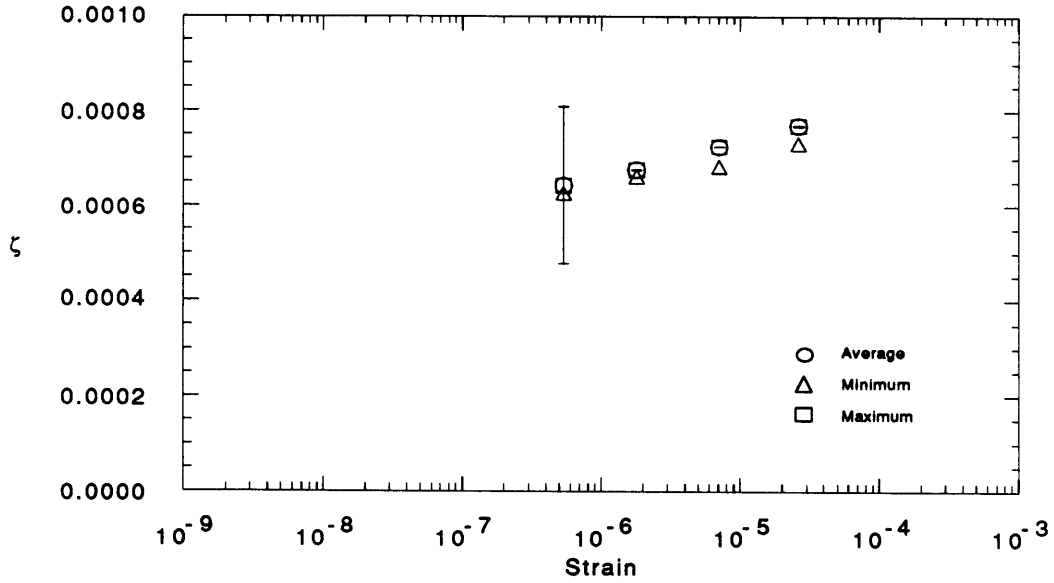

Figure 4.34 Damping in Mode #1 in Testbed, f=43.9 Hz, Large Strain Range

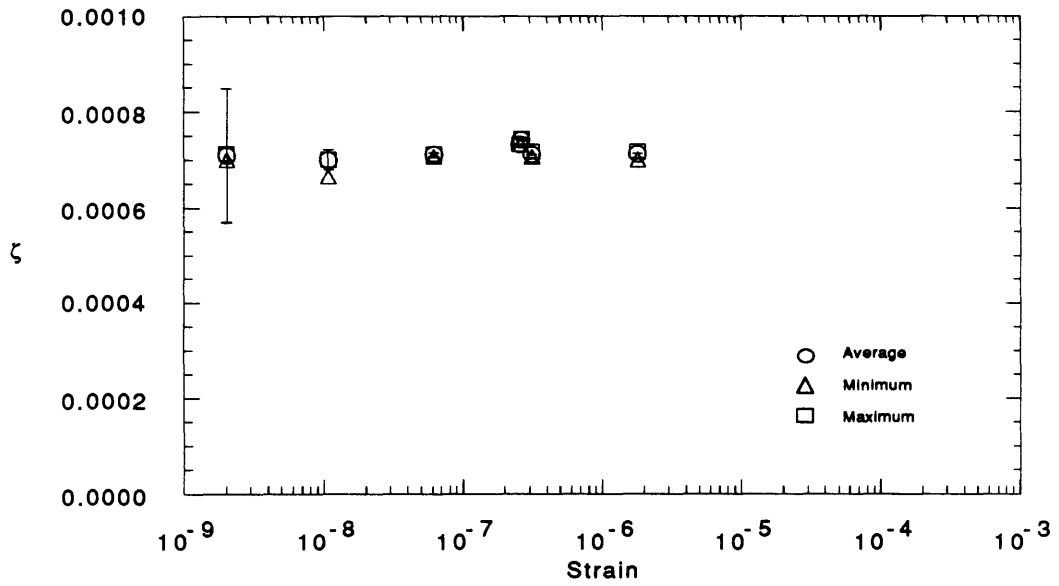

Figure 4.35 Damping in Mode #2 ofTestbed, f=40.0 Hz, Small Strain Range

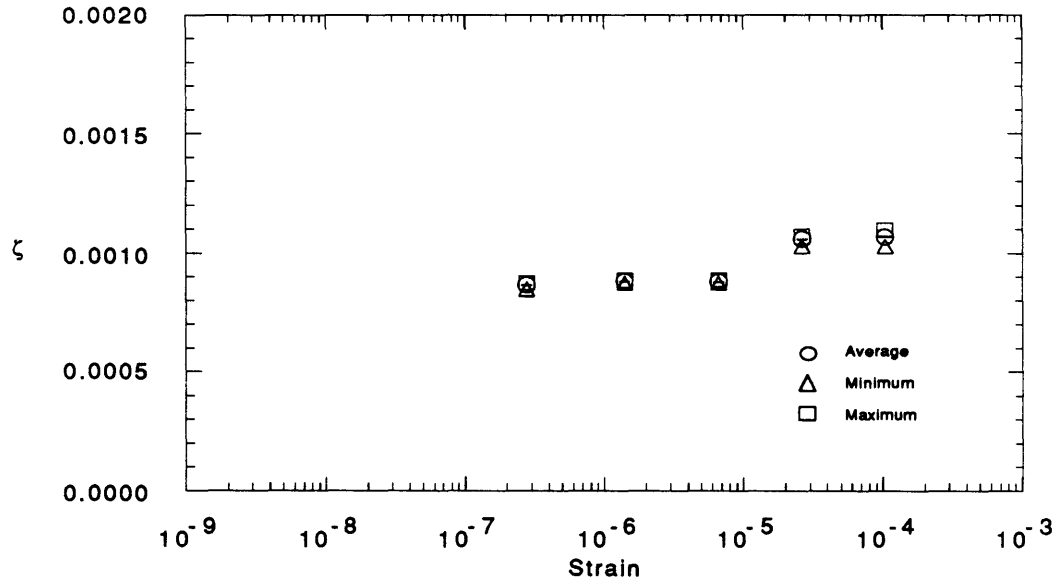

Figure 4.36 Damping in Mode #2 of Testbed, f=38.9 Hz, Large Strain Range

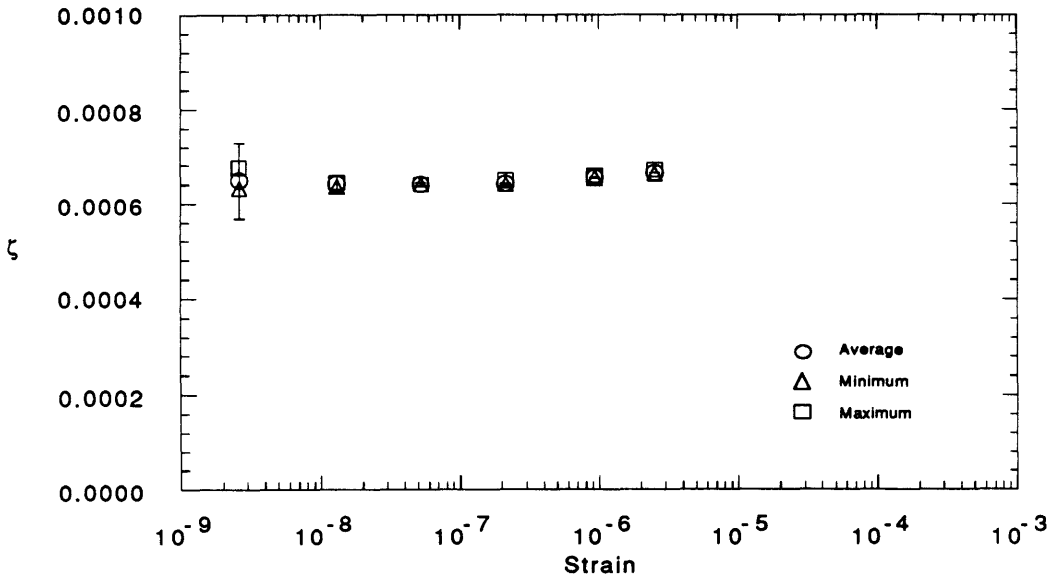

Figure 4.37 Damping in Testbed Mode #3, f=55.4 Hz, Small Strain Range

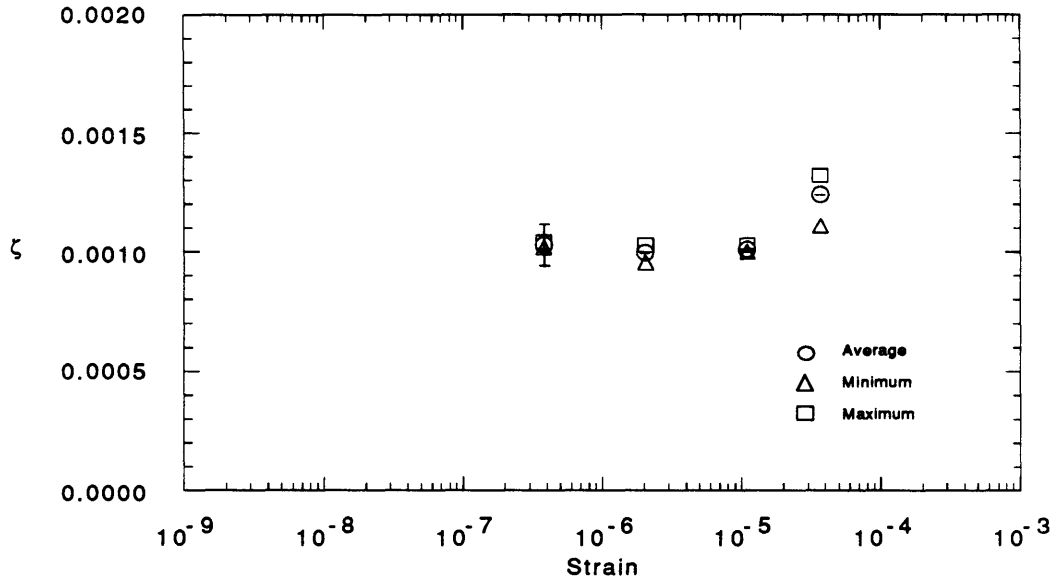

Figure 4.38 Damping in Testbed Mode #3, f=54.4 Hz, Large Strain Range

CHAPTER 5

CONCLUSIONS AND RECOMMENDATIONS FOR FUTURE WORK

Several conclusions can be drawn from the results of the experiments presented in Chapter 4 concerning both the material and structural damping tests. Results from both tests performed to characterize the behavior of material and structural damping, show that the behavior of damping can be divided into two distict regions. The bounds on these regions depend on the geometry of the test specimens. In the region of small strain, the damping is independent of strain and is constant down to 1 nε. In the region of large strain, damping increases with strain. The rate of damping increase with strain depends on both the material and geometry of the test specimens.

Damping of the aluminum bars and tubes shows little variation with strain level in the small strain region, from 1 nε to about 10 με. This asymptotic lower limit on damping for small strain can be predicted for transverse vibration of the aluminum bars with the thermoelastic model developed by Zener [Zener, 1948]. For transverse vibration of the aluminum tubes, the damping is more than an order of magnitude lower and is not correlated with a thermoelastic model. This implies that the damping of the aluminum tubes has a different origin than that of the bars. At larger strain levels, above 10 με, the damping of both the bars and tubes can be modeled using the dislocation model developed by Boser [Boser, 1983]. This model relates the dependence of damping on strain, to the dislocation density and lattice properties of metals.

The results from the material damping tests of the graphite/epoxy bars and tubes show that the damping of graphite/epoxy laminates also has an asymptotic lower limit in the small strain region, below 10 με. For laminates with uniply layups, and simple, rectangular geometries, this limit can predicted with models developed by Hashin [Ashton et al, 1969], and Adams and Bacon [Adams and Bacon, 1973]. These models relate the damping of a uniply laminate to the properties of the matrix. A change in geometry to a cylindrical cross section appears to have only a small effect on damping. This implies that, unlike the aluminum specimens, the same

loss mechanism is present in both the graphite/epoxy bars and tubes. This damping shows a weaker dependence on strain than the damping of the aluminum specimens in the large strain region, above 10 με.

Structural damping, measured from the precision interferometer truss, also shows an asymptotic lower limit in the small strain region, measured using the piezoelectric actuator, at least to 1 nε. In the large strain region, above 1 με, the damping obtained using the proof mass actuator, appears to depend on strain level. The low strain damping ratios obtained from the tests of three modes of the testbed are an order of magnitude greater than the damping ratios of the aluminum tube damping specimens. Since the testbed is constructed of tubes made from the same 6061-T6 aluminum as the aluminum tube damping specimens, this result implies that the primary source of the structural damping of the testbed is in the joints and attachments. Addition of the proof mass actuator to the structure causes a small increase in damping, showing that the damping of the testbed is sensitive to external instrumentation. This result may prove important to the behavior of the fully integrated interferometer instrumented with optical metrology and control hardware.

Another conclusion that can be inferred from the test results is that the instrumentation and methods developed for these experiments can be used to measure and actuate strains down to at least 1 nε. Limitations on the techniques used to measure damping are imposed by the limits of the sensors. Lower limits on the resolution of the piezoelectric sensors are due to mechanical and electrical noise, and not due to inherent noise of the sensors. Previous work [Forward, 1980], verified by the results down to 1 nε from this study, show that the piezoelectric sensors are capable of measuring strains down to at least 10 pε with improved amplification and noise isolation techniques.

One area that further work should be directed toward is the modeling of the damping of structures with more complicated geometries and layups than rectangular aluminum bars or uniply graphite/epoxy laminates. Even though the damping of the trasverse vibration of aluminum tubes is shown to have a lower limit, the mechanism causing the damping is not well understood causing the need for better models.

Another area that requires further study is the damping of fully integrated structures. Results from the tests of the structural damping of the interferometer testbed imply that external instrumentation may cause an increase in damping. Unlike the precision truss used in this study, a flight ready interferometer will include many optical collectors, electronic instrumentation, power supplies, and other external appendages. The dynamics of these appendages may dominate the behavior of the structure and the behavior of the damping of these external structures with strain may not have a simple asymptotic lower limit. Also, even though ground tests of precision optical instruments may show not aberrant behavior, these tests under gravity loading may not accurately represent the behavior of the instruments in space.

Finally, a study of a third source of damping due to external damping enhancement treatments should be performed. One example of these treatments are viscoelastic materials used in constrained and unconstrained layers which may be used on future optical instruments. At large strains, the damping due to these treatments is well understood. However, at the nanostrain levels required for the control of optical instruments, the damping may not behave in a predictable manner. Using the example of constrained viscoelastic damping treatments, the mechanism responsible for damping is shear of the viscoelastic layer. At small strain levels these shear mechanisms may no longer be present.

REFERENCES

Ashton, J.E., Halpin, J.C., Petit, P.H., 1969, Primer on Composite Materials: Analysis, Technomic Publishing Company, Stamford, CT.

Batchelor, G.K., 1967, An Introduction to Fluid Dynamics, Cambridge University Press, Cambridge.

Blevins, Robert D., 1977, Flow-Induced Vibration, Van Nostrand Reinhold Company, New York.

Blevins, Robert D., 1984, Formulas For Natural Frequency and Mode Shape, Robert E. Kreiger Publishing Company, Malabar, FL.

Boser, O., "Internal Friction due to Hysteretic Dislocation Motion in Solid Solution Crystals", Journal of Applied Physics, Vol. 54, May 1983.

Braginsky, V.B., Mitrofanov, V.P., Panov, V.F., 1985, Systems With Small Dissipation, The University of Chicago Press, Chicago, IL.

Craig, Roy R., 1981, Structural Dynamics - An Introduction to Computer Methods, John Wiley and Sons, New York.

Crawley, Edward F., Sarver, George L., Mohr, David G., "Experimental Measurements of Passive Material and Structural Damping For Flexible Space Structures", ACTA Astronautica, Vol. 10, No. 5-6, 1983.

Crawley, Edward, F., van Schoor, Marthinus C., "Material Damping in Aluminum and Metal Matrix Composites", Journal of Composite Materials, Vol. 21, June 1987.

Crawley, Edward F., Sigler, Jonathan, van Schoor, Martinus, "Prediction and Measurement of Joint Damping in Scaled Model Space Structures", MIT SSL 7-88, July 1988.

Forward, Robert L. "Picostrain Measurements With Piezoelectric Transducers", Journal of Applied Physics, Volume 51, November 1980.

Garba, John, "Survey of the State of the Art of Microdynamic Response of Structures - Preliminary Results", JPL Memorandum, November 30, 1988.

Granick, N., Stern, J.D., "Material Damping of Aluminum by a Resonant-Dwell Technique", NASA TND-2893, August 1965.

Hagood, N.W., von Flotow, A., "Structural Vibration Damping With Piezoelectric Materials Shunted by Passive Electrical Networks", Proceedings of Damping '89, February 8-10, 1989, W. Palm Beach, FL.

Hall, S., Results from a MATLAB model of the SERC Interferometer Testbed, Massachusetts Institute of Technology, 1990.

Hecht, Eugene, 1987, Optics, Addison-Wesley Publishing Company, Reading, MA.

Jones, Robert, M., 1975, Mechanics of Composite Materials, McGraw-Hill, New York.

Lagace, Paul A., Brewer, John C., Varnerin, Carl F., 1988, "TELAC Manufacturing Course Class Notes", MIT TELAC Report 88-4.

Lesieutre, George, A., "Damping in Unidirectional Graphite/Metal Composites and Material Design Potential", Proceedings of the ASME Vibrations Conference, Boston, MA, September 1987.

Lublin, Leonard, Results from an ADINA model of the SERC Interferometer Testbed, Massachusetts Institute of Technology, 1990.

Measurements Group, Inc., 1988, 2100 System Strain Gage Conditioner and Amplifier System Instruction Manual, Raleigh, NC.

Meirovitch, Leonard, 1986, Elements of Vibration Analysis, McGraw-Hill Book Company, New York.

Michelson, Peter F., Price, John C., Taber, Robert C., "Resonant Mass Detectors of Gravitational Radiation", Science, July 10, 1987.

Mohr, D.G., "Experimental Measurements of Material Damping of Aluminum and Graphite/Epoxy in Free-Fall With Tunable Excitation", MIT Space Systems Laboratory #11-82, June 1982.

Morgan, S.H., Nein, M.E., Davis, B.G., Hamilton, E.C., Roberts, D.H., Traub, W.A., "Concepts for Large Interferometers in Space" AIAA/SPE/OSA Technology for Space Astrophysics Conference: The Next 30 Years, AIAA Paper 82-1851.

Nowick, A.S., Berry, B.S., 1972, Anelastic Relaxation in Crystalline Solids, Academic Press, New York.

Piezo Systems, 1989, Piezoelectric Motor/Actuator Kit Manual, Cambridge, MA.

Ralls, Kenneth M., Courtney, Thomas, H., Wulff, John, 1976, An Introduction to Materials Science and Engineering, John Wiley and Sons, New York.

Roylance, Margaret E., Houghton, William W., Ghiorse, Seth R., "The Effect of Epoxide Purity and Thermal History on the Properties of a Tetrafunctional Epoxy Resin", Proceedings of the 28th National SAMPE Symposium and Exhibition, April 12-14, 1983, Anaheim, CA.

Sarver, George L., Crawley, Edward F, "Energy Transfer and Dissipation in Structures With Discrete Non-linearities", MIT SSL 25-87, November, 1987.

Senturia, Stephen D., Wedlock, Bruce D., 1975, Electronic Circuits and Applications, John Wiley and Sons, New York.

Taylor, John R., 1982, An Introduction to Error Analysis, Oxford University Press, Cambridge.

Traub, W.A, Gursky, H., "Coherent Arrays for Optical Astronomy in Space", Proceedings of the Seminar Active Optical Devices and Applications, Washington D.C., April 10-11, 1980.

Tsai, Stephen W., Hahn, H. Thomas, Introduction to Composite Materials, 1980, Technomic Publishing Company, Westport, CT.

United States Department of Defense, Military Standardization Handbook: Metallic Materials and Elements for Aerospace Vehicle Structures, MIL-HDBK-5C, Volume 1, September 15, 1976.

Zener, C., 1948, Elasticity and Anelasticity of Metals, University of Chicago Press, Chicago, IL.

APPENDIX 1

Summary of Data

Summary of Damping From 6061-T6 Al Bar Specimens
All results using unmodified bending motor in air except where noted
key:
• = test with modified bending motor
* = test in vacuum

Test Specimen	fn (Hz)	Strain	Predicted Damping Ratio	Average Damping Ratio	Minimum Damping Ratio	Maximum Damping Ratio	Error From Noise	Damping Ratio Due to Air	Avg. Corr. For Air
1.7 m al bar	6.172	9.68E-07	9.80E-04	1.24E-03	1.22E-03	1.29E-03	1.43E-07	7.08E-05	1.17E-03
1.7 m al bar	6.1735	1.60E-07	9.80E-04	1.21E-03	1.19E-03	1.24E-03	8.43E-07	7.08E-05	1.14E-03
1.7 m al bar	6.1752	4.39E-08	9.80E-04	1.29E-03	1.24E-03	1.31E-03	3.26E-06	7.08E-05	1.22E-03
1.7 m al bar	6.1756	1.33E-07	9.80E-04	1.19E-03	1.12E-03	1.24E-03	1.04E-05	7.08E-05	1.12E-03
1.7 m al bar	6.1739	4.28E-09	9.80E-04	1.25E-03	1.19E-03	1.27E-03	3.48E-05	7.08E-05	1.18E-03
1.7 m al bar	6.1744	1.42E-09	9.80E-04	1.28E-03	1.26E-03	1.29E-03	1.17E-04	7.08E-05	1.21E-03
1.7 m al bar	17.112	1.62E-06	9.49E-04	1.31E-03	1.26E-03	1.37E-03	3.79E-07	4.25E-05	1.27E-03
1.7 m al bar	17.126	4.39E-07	9.49E-04	1.34E-03	1.32E-03	1.37E-03	1.96E-06	4.25E-05	1.30E-03
1.7 m al bar	17.125	1.06E-07	9.49E-04	1.29E-03	1.26E-03	1.34E-03	8.02E-06	4.25E-05	1.25E-03
1.7 m al bar	17.126	3.29E-08	9.49E-04	1.32E-03	1.29E-03	1.34E-03	2.50E-05	4.25E-05	1.28E-03
1.7 m al bar	17.125	1.15E-08	9.49E-04	1.21E-03	1.20E-03	1.23E-03	6.99E-05	4.25E-05	1.17E-03
1.7 m al bar	17.124	3.52E-09	9.49E-04	1.24E-03	1.23E-03	1.26E-03	2.13E-04	4.25E-05	1.20E-03
1.7 m al bar	17.126	1.18E-09	9.49E-04	1.16E-03	1.14E-03	1.17E-03	7.12E-04	4.25E-05	1.12E-03
1.3 m al bar	9.348	1.19E-08	1.09E-03	1.45E-03	1.44E-03	1.48E-03	9.74E-06	5.76E-05	1.39E-03
1.3 m al bar	9.348	4.22E-09	1.09E-03	1.30E-03	1.23E-03	1.39E-03	2.45E-05	5.76E-05	1.24E-03
1.3 m al bar	9.348	1.30E-09	1.09E-03	1.34E-03	1.34E-03	1.34E-03	7.71E-05	5.76E-05	1.28E-03
1.3 m al bar	9.348	5.97E-07	1.09E-03	1.35E-03	1.34E-03	1.39E-03	1.27E-07	5.76E-05	1.29E-03
1.3 m al bar	9.349	2.89E-07	1.09E-03	1.36E-03	1.34E-03	1.39E-03	3.78E-07	5.76E-05	1.30E-03
1.3 m al bar	9.35	7.81E-06	1.09E-03	1.34E-03	1.34E-03	1.34E-03	1.44E-06	5.76E-05	1.28E-03
1.3 m al bar	25.835	3.82E-06	7.26E-04	9.37E-04	8.62E-04	9.60E-04	9.07E-08	3.46E-05	9.02E-04
1.3 m al bar	25.835	1.94E-06	7.26E-04	9.50E-04	9.41E-04	9.60E-04	2.20E-07	3.46E-05	9.15E-04
1.3 m al bar	25.83	6.73E-07	7.26E-04	9.47E-04	9.21E-04	9.60E-04	6.17E-07	3.46E-05	9.12E-04
1.3 m al bar	25.83	2.15E-07	7.26E-04	9.36E-04	9.21E-04	9.41E-04	1.93E-07	3.46E-05	9.01E-04
1.3 m al bar	25.829	6.82E-08	7.26E-04	9.55E-04	9.21E-04	9.80E-04	6.13E-06	3.46E-05	9.20E-04
1.3 m al bar	25.833	2.24E-08	7.26E-04	9.46E-04	9.21E-04	9.80E-04	1.84E-05	3.46E-05	9.11E-04

Test Specimen	fn (Hz)	Strain	Predicted Damping Ratio	Average Damping Ratio	Minimum Damping Ratio	Maximum Damping Ratio	Error From Noise	Damping Ratio Due to Air	Avg. Corr. For Air
1.3 m al bar	25.829	7.32E-09	7.26E-04	9.70E-04	9.41E-04	9.80E-04	6.14E-05	3.46E-05	9.35E-04
1.3 m al bar	25.829	2.22E-09	7.26E-04	9.69E-04	9.50E-04	9.88E-04	1.95E-04	3.46E-05	9.34E-04
1.3 m al bar	50.578	1.93E-06	4.08E-04	5.80E-04	5.73E-04	5.83E-04	3.18E-08	2.47E-05	5.55E-04
1.3 m al bar	50.584	1.34E-06	4.08E-04	5.83E-04	5.73E-04	5.92E-04	4.59E-08	2.47E-05	5.58E-04
1.3 m al bar	50.59	2.66E-07	4.08E-04	5.86E-04	5.83E-04	5.92E-04	3.30E-07	2.47E-05	5.61E-04
1.3 m al bar	50.589	1.24E-05	4.08E-04	5.86E-04	5.63E-04	5.92E-04	4.96E-06	2.47E-05	5.61E-04
1.3 m al bar	50.587	4.79E-06	4.08E-04	5.87E-04	5.83E-04	5.92E-04	1.29E-05	2.47E-05	5.62E-04
1.3 m al bar	50.584	6.35E-08	4.08E-04	5.87E-04	5.83E-04	5.92E-04	9.81E-07	2.47E-05	5.62E-04
1.3 m al bar	50.582	2.02E-08	4.08E-04	5.83E-04	5.83E-04	5.92E-04	3.07E-06	2.47E-05	5.58E-04
1.3 m al bar	50.586	6.35E-09	4.08E-04	5.92E-04	5.92E-04	5.92E-04	9.83E-06	2.47E-05	5.67E-04
1.3 m al bar	50.587	2.02E-09	4.08E-04	5.99E-04	5.92E-04	6.02E-04	3.10E-05	2.47E-05	5.74E-04
.9 m al bar	19.452	5.88E-06	8.94E-04	1.15E-03	1.15E-03	1.15E-03	2.10E-08	3.99E-05	1.11E-03
.9 m al bar	19.452	9.10E-07	8.94E-04	1.15E-03	1.13E-03	1.15E-03	1.34E-07	3.99E-05	1.11E-03
.9 m al bar	19.451	2.89E-07	8.94E-04	1.18E-03	1.15E-03	1.18E-03	4.38E-07	3.99E-05	1.14E-03
.9 m al bar	19.451	9.26E-08	8.94E-04	1.16E-03	1.13E-03	1.18E-03	1.36E-06	3.99E-05	1.12E-03
.5 m al bar	171.315	4.89E-06	1.26E-04	3.66E-04	3.61E-04	3.70E-04	1.24E-08	1.34E-05	3.53E-04
.5 m al bar	173.609	4.47E-06	1.24E-04	2.59E-04	2.50E-04	2.76E-04	1.00E-08	1.34E-05	2.46E-04
.5 m al bar	173.62	2.38E-07	1.24E-04	2.56E-04	2.53E-04	2.59E-04	1.77E-07	1.34E-05	2.43E-04
.5 m al bar	173.224	8.04E-08	1.24E-04	2.57E-04	2.56E-04	2.59E-04	1.54E-05	1.34E-05	2.44E-04
.5 m al bar	173.621	2.57E-08	1.24E-04	2.60E-04	2.59E-04	2.61E-04	1.69E-06	1.34E-05	2.47E-04
.5 m al bar	173.621	8.25E-09	1.24E-04	2.87E-04	2.84E-04	2.87E-04	6.14E-06	1.34E-05	2.74E-04
.5 m al bar	173.627	7.55E-07	1.24E-04	2.55E-04	2.53E-04	2.56E-04	5.61E-08	1.34E-05	2.42E-04
.5 m al bar	173.625	2.32E-06	1.24E-04	2.65E-04	2.61E-04	2.67E-04	1.91E-08	1.34E-05	2.52E-04
.5 m al bar	173.632	1.33E-05	1.24E-04	2.64E-04	2.64E-04	2.64E-04	3.31E-09	1.34E-05	2.51E-04
.5 m al bar	173.638	2.79E-05	1.24E-04	3.67E-04	3.65E-04	3.68E-04	2.15E-09	1.34E-05	3.54E-04
•1.3 m al bar	9.218	2.79E-06	1.09E-03	1.24E-03	1.23E-03	1.24E-03	5.20E-08	5.80E-05	1.18E-03
••1.3 m al bar	9.2395	6.08E-07	1.09E-03	1.05E-03	1.02E-03	1.10E-03	8.43E-07	0.00E+00	1.05E-03
••1.3 m al bar	9.237	1.34E-05	1.09E-03	1.04E-03	1.04E-03	1.09E-03	3.93E-08	0.00E+00	1.04E-03
••1.3 m al bar	9.2365	1.76E-04	1.09E-03	1.07E-03	1.04E-03	1.07E-03	7.43E-09	0.00E+00	1.07E-03
••1.3 m al bar	9.235	3.19E-04	1.09E-03	1.05E-03	1.06E-03	1.08E-03	3.03E-09	0.00E+00	1.05E-03
••1.3 m al bar	9.234	7.36E-05	1.09E-03	1.07E-03	1.04E-03	1.09E-03	1.77E-09	0.00E+00	1.07E-03
•.5 m al bar	58.092	4.61E-07	3.62E-04	7.24E-04	7.07E-04	7.41E-04	1.99E-07	2.31E-05	7.01E-04
••.5m al bar	58.24	1.51E-07	3.62E-04	5.96E-04	4.48E-04	6.72E-04	5.10E-07	0.00E+00	5.96E-04
••.5m al bar	58.198	6.26E-06	3.62E-04	6.14E-04	5.69E-04	6.55E-04	4.20E-07	0.00E+00	6.14E-04
••.5m al bar	58.159	3.98E-05	3.62E-04	6.88E-04	6.81E-04	6.90E-04	2.17E-09	0.00E+00	6.88E-04
••.5m al bar	58.142	9.64E-05	3.62E-04	7.78E-04	7.67E-04	8.02E-04	1.01E-09	0.00E+00	7.78E-04

Test Specimen	fn (Hz)	Strain	Predicted Damping Ratio	Average Damping Ratio	Minimum Damping Ratio	Maximum Damping Ratio	Error From Noise	Damping Ratio Due to Air	Avg. Corr. For Air
*•.5 m al bar	58.112	2.34E-04	3.62E-04	1.02E-03	1.02E-03	1.03E-03	5.66E-10	0.00E+00	1.02E-03
•.5 m al bar	57.98	2.26E-06	3.62E-04	6.27E-04	5.93E-04	6.70E-04	4.53E-08	2.31E-05	7.87E-04
*•.5 m al bar	58.158	7.07E-07	3.62E-04	8.10E-04	8.10E-04	8.10E-04	1.14E-07	0.00E+00	6.27E-04
*•.5 m al bar	58.128	9.07E-06	3.62E-04	6.99E-04	6.70E-04	7.22E-04	1.20E-08	0.00E+00	6.99E-04
*•.5 m al bar	58.031	4.90E-05	3.62E-04	9.08E-04	8.85E-04	9.36E-04	2.42E-09	0.00E+00	9.08E-04
*•.5 m al bar	57.968	1.38E-04	3.62E-04	1.16E-03	1.14E-03	1.18E-03	1.10E-09	0.00E+00	1.16E-03
*•.5 m al bar	57.925	2.15E-04	3.62E-04	1.39E-03	1.32E-03	1.49E-03	8.44E-10	0.00E+00	1.39E-03
*•.5 m al bar	57.68	6.07E-04	3.62E-04	2.98E-03	1.32E-03	3.03E-03	6.51E-10	0.00E+00	2.98E-03

Summary of Damping From 6061-T6 Al Tube Specimens

All results using unmodified bending motor in air except where noted

key:

• = test with modified bending motor

* = test in vacuum

Test Specimen	fn (Hz)	Strain	Average Damping Ratio	Minimum Damping Ratio	Maximum Damping Ratio	Error From Noise	Damping Ratio Due to Air	Avg. Corr. For Air
.9 m al tube	185.158	7.89E-05	7.24E-05	7.02E-05	7.56E-05	6.61E-10	1.21E-05	6.03E-05
.9 m al tube	185.156	2.55E-05	6.39E-05	6.21E-05	6.48E-05	1.74E-09	1.21E-05	5.18E-05
.9 m al tube	185.149	8.84E-08	6.52E-05	6.21E-05	6.75E-05	5.20E-07	1.21E-05	5.31E-05
.9 m al tube	185.147	2.70E-07	6.57E-05	6.21E-05	6.75E-05	1.72E-07	1.21E-05	5.36E-05
.9 m al tube	185.15	8.38E-07	6.48E-05	6.21E-05	6.75E-05	5.64E-08	1.21E-05	5.27E-05
.9 m al tube	185.153	2.53E-06	6.96E-05	6.75E-05	7.02E-05	6.79E-07	1.21E-05	5.74E-05
.9 m al tube	185.106	8.74E-06	5.89E-05	5.67E-05	6.48E-05	4.99E-09	1.21E-05	4.68E-05
.9 m al tube	185.079	3.76E-04	1.08E-04	1.05E-04	1.11E-04	2.05E-10	1.21E-05	9.59E-05
.9 m al tube	185.095	2.51E-08	6.79E-05	6.75E-05	7.02E-05	1.94E-06	1.21E-05	5.58E-05
.9 m al tube	185.097	1.08E-08	7.20E-05	7.02E-05	7.83E-05	4.72E-06	1.21E-05	5.99E-05
•.9 m al tube	510.324	1.11E-05	1.23E-04	1.20E-04	1.24E-04	2.85E-09	7.28E-06	1.16E-04
•.9 m al tube	510.324	1.10E-06	1.25E-04	1.25E-04	1.26E-04	2.90E-08	7.28E-06	1.18E-04
.7 m al tube	832.767	9.71E-08	1.61E-04	1.67E-04	1.79E-04	6.69E-07	5.70E-06	1.55E-04
•.7 m al tube	308.065	8.02E-06	1.61E-04	1.57E-04	1.64E-04	6.62E-09	9.37E-06	1.52E-04
•.7 m al tube	308.234	1.11E-06	1.17E-04	1.09E-04	1.27E-04	3.60E-08	9.37E-06	1.08E-04
*•.7 m al tube	308.826	1.20E-06	1.08E-04	8.26E-05	1.62E-04	2.79E-08	0.00E+00	1.08E-04
*•.7 m al tube	308.785	1.17E-05	1.02E-04	9.25E-05	1.14E-04	3.45E-09	0.00E+00	1.02E-04
*•.7 m al tube	308.718	4.56E-05	1.39E-04	1.33E-04	1.43E-04	1.07E-09	0.00E+00	1.39E-04
*•.7 m al tube	308.599	1.55E-04	2.54E-04	2.50E-04	2.60E-04	5.99E-10	0.00E+00	2.54E-04
*•.7 m al tube	308.455	3.43E-04	3.73E-04	3.69E-04	3.80E-04	4.15E-10	0.00E+00	3.73E-04
*•.7 m al tube	308.335	5.53E-04	4.57E-04	4.53E-04	4.59E-04	3.17E-10	0.00E+00	4.57E-04
•.7 m al tube	308.104	7.11E-05	1.88E-04	1.85E-04	1.92E-04	9.06E-10	9.37E-06	1.79E-04
•.7 m al tube	308.145	1.96E-05	1.34E-04	1.31E-04	1.38E-04	2.36E-09	9.37E-06	1.25E-04
•.7 m al tube	308.165	4.33E-06	1.18E-04	1.15E-04	1.22E-04	9.27E-09	9.37E-06	1.09E-04
•.7 m al tube	308.175	8.76E-07	1.16E-04	1.14E-04	1.17E-04	4.43E-08	9.37E-06	1.07E-04
•.7 m al tube	308.201	1.05E-07	1.13E-04	1.12E-04	1.14E-04	3.56E-07	9.37E-06	1.04E-04
•.7 m al tube	308.2	2.09E-08	1.20E-04	1.17E-04	1.25E-04	2.29E-06	9.37E-06	1.11E-04
•.7 m al tube	829.549	4.87E-07	6.46E-05	5.97E-05	7.18E-05	1.91E-08	5.71E-06	5.89E-05

Summary of Damping From AS4/3501 Graphite/Epoxy Bars
With [0]24 Layup

All results taken in air with unmodified bending motors except where noted

key:

• = test with modified bending motor

* = test in vacuum

Test Specimen	fn (Hz)	Strain	Predicted Damping Ratio	Average Damping Ratio	Minimum Damping Ratio	Maximum Damping Ratio	Error From Noise	Damping Ratio Due to Air	Avg. Corr. For Air
.9 m uniply bar	30.869	2.68E-06	1.92E-04	3.82E-04	3.80E-04	3.88E-04	3.04E-08	9.77E-05	2.84E-04
.9 m uniply bar	30.8695	5.36E-07	1.92E-04	3.80E-04	3.80E-04	3.80E-04	1.52E-07	9.77E-05	2.82E-04
.9 m uniply bar	30.8695	1.08E-07	1.92E-04	3.74E-04	3.72E-04	3.80E-04	7.37E-07	9.77E-05	2.76E-04
.9 m uniply bar	30.8695	1.04E-08	1.92E-04	3.76E-04	3.72E-04	3.80E-04	3.76E-06	9.77E-05	2.78E-04
.9 m uniply bar	30.87	3.63E-09	1.92E-04	3.80E-04	3.72E-04	3.88E-04	1.65E-05	9.77E-05	2.82E-04
.9 m uniply bar	30.8695	1.36E-05	1.92E-04	3.80E-04	3.80E-04	3.80E-04	6.00E-09	9.77E-05	2.82E-04
.9 m uniply bar	30.869	3.97E-05	1.92E-04	4.02E-04	3.96E-04	4.05E-04	2.18E-09	9.77E-05	3.04E-04
.9 m uniply bar	30.868	7.89E-05	1.92E-04	4.13E-04	4.13E-04	4.13E-04	1.12E-09	9.77E-05	3.15E-04
.9 m uniply bar	83.48	1.13E-05	1.92E-04	4.67E-04	4.55E-04	4.73E-04	4.00E-10	5.94E-05	4.08E-04
.9 m uniply bar	83.482	4.16E-05	1.92E-04	4.13E-04	4.07E-04	4.19E-04	9.42E-10	5.94E-05	3.54E-04
.9 m uniply bar	83.488	7.72E-06	1.92E-04	4.18E-04	4.07E-04	4.31E-04	5.10E-09	5.94E-05	3.59E-04
.9 m uniply bar	83.488	1.81E-06	1.92E-04	3.67E-04	3.65E-04	3.68E-04	1.94E-08	5.94E-05	3.08E-04
.9 m uniply bar	83.495	3.57E-07	1.92E-04	3.72E-04	3.71E-04	3.74E-04	9.95E-08	5.94E-05	3.13E-04
.9 m uniply bar	83.495	7.07E-08	1.92E-04	3.78E-04	3.77E-04	3.80E-04	5.12E-07	5.94E-05	3.19E-04
.9 m uniply bar	83.4945	1.77E-08	1.92E-04	3.82E-04	3.80E-04	3.83E-04	2.05E-06	5.94E-05	3.23E-04
.9 m uniply bar	83.495	4.54E-09	1.92E-04	3.83E-04	3.80E-04	3.83E-04	8.03E-06	5.94E-05	3.24E-04
.9 m uniply bar	83.492	8.63E-10	1.92E-04	3.64E-04	3.59E-04	3.71E-04	3.95E-05	5.94E-05	3.05E-04
.7 m uniply bar	56.8945	8.48E-05	1.92E-04	3.30E-04	3.25E-04	3.34E-04	2.86E-09	7.20E-05	2.58E-04
.7 m uniply bar	56.895	1.67E-05	1.92E-04	3.21E-04	3.21E-04	3.25E-04	1.42E-08	7.20E-05	2.49E-04
.7 m uniply bar	56.896	3.31E-06	1.92E-04	3.33E-04	3.30E-04	3.34E-04	7.43E-08	7.20E-05	2.61E-04
.7 m uniply bar	56.897	6.56E-07	1.92E-04	3.34E-04	3.34E-04	3.34E-04	3.73E-07	7.20E-05	2.62E-04
.7 m uniply bar	56.897	1.33E-07	1.92E-04	3.32E-04	3.30E-04	3.34E-04	1.83E-06	7.20E-05	2.60E-04
.7 m uniply bar	56.8965	3.44E-08	1.92E-04	3.25E-04	3.25E-04	3.25E-04	6.98E-06	7.20E-05	2.53E-04
.7 m uniply bar	56.8965	8.25E-09	1.92E-04	3.10E-04	3.08E-04	3.16E-04	2.84E-05	7.20E-05	2.38E-04
.7 m uniply bar	56.8965	2.46E-09	1.92E-04	3.10E-04	3.08E-04	3.13E-04	9.37E-05	7.20E-05	2.38E-04
.7 m uniply bar	56.8945	2.38E-04	1.92E-04	3.56E-04	3.56E-04	3.56E-04	1.10E-09	7.20E-05	2.84E-04
.7 m uniply bar	156.69	3.78E-05	1.92E-04	4.11E-04	4.05E-04	4.15E-04	1.03E-09	4.34E-05	3.68E-04
.7 m uniply bar	156.696	1.72E-08	1.92E-04	3.42E-04	3.41E-04	3.45E-04	2.18E-06	4.34E-05	2.99E-04
.7 m uniply bar	156.697	4.45E-09	1.92E-04	3.41E-04	3.29E-04	3.45E-04	7.19E-06	4.34E-05	2.98E-04

Test Specimen	fn (Hz)	Strain	Predicted Damping Ratio	Average Damping Ratio	Minimum Damping Ratio	Maximum Damping Ratio	Error From Noise	Damping Ratio Due to Air	Avg. Corr. For Air
.7 m uniply bar	156.695	1.02E-09	1.92E-04	3.38E-04	3.38E-04	3.38E-04	3.16E-05	4.34E-05	2.95E-04
.7 m uniply bar	156.702	6.96E-06	1.92E-04	4.40E-04	4.37E-04	4.50E-04	6.08E-07	4.34E-05	3.97E-04
.7 m uniply bar	156.7	1.76E-06	1.92E-04	3.45E-04	3.45E-04	3.45E-04	1.87E-08	4.34E-05	3.02E-04
.7 m uniply bar	156.701	3.54E-07	1.92E-04	3.41E-04	3.41E-04	3.41E-04	9.19E-08	4.34E-05	2.98E-04
.7 m uniply bar	156.702	7.11E-08	1.92E-04	3.41E-04	3.41E-04	3.41E-04	4.56E-07	4.34E-05	2.98E-04
.7 m uniply bar	156.665	8.38E-05	1.92E-04	5.06E-04	4.98E-04	5.11E-04	5.92E-10	4.34E-05	4.63E-04
•.9 m uniply bar	29.413	6.35E-07	1.92E-04	3.83E-04	3.83E-04	3.83E-04	1.45E-07	1.00E-04	2.83E-04
*•.9 m uniply bar	29.5014	1.13E-06	1.92E-04	2.13E-04	2.12E-04	2.15E-04	4.50E-08	0.00E+00	2.13E-04
*•.9 m uniply bar	29.5012	1.23E-05	1.92E-04	2.14E-04	2.12E-04	2.15E-04	4.20E-09	0.00E+00	2.14E-04
*•.9 m uniply bar	29.495	5.32E-05	1.92E-04	2.62E-04	2.41E-04	2.71E-04	1.22E-09	0.00E+00	2.62E-04
*•.9 m uniply bar	29.476	1.45E-04	1.92E-04	6.70E-04	6.61E-04	6.78E-04	1.44E-09	0.00E+00	6.70E-04
*•.9 m uniply bar	29.47	1.15E-04	1.92E-04	2.15E-03	2.14E-03	2.17E-03	4.83E-09	0.00E+00	2.15E-03
•.9 m uniply bar	29.432	2.10E-03	1.92E-04	4.25E-04	4.14E-04	4.40E-04	4.80E-08	1.00E-04	3.25E-04
*•.9 m uniply bar	29.5174	1.10E-06	1.92E-04	2.21E-04	2.14E-04	2.27E-04	4.78E-08	0.00E+00	2.21E-04
*•.9 m uniply bar	29.5109	8.29E-06	1.92E-04	2.67E-04	2.61E-04	2.71E-04	7.86E-09	0.00E+00	2.67E-04
*•.9 m uniply bar	29.495	2.68E-05	1.92E-04	4.06E-04	3.83E-04	4.33E-04	3.85E-09	0.00E+00	4.06E-04
*•.9 m uniply bar	29.428	5.01E-05	1.92E-04	1.19E-03	1.19E-03	1.19E-03	6.74E-09	0.00E+00	1.19E-03
•.9 m uniply bar	29.557	9.03E-06	1.92E-04	3.88E-04	3.81E-04	3.89E-04	1.03E-08	9.99E-05	2.88E-04
*•.9 m uniply bar	29.6436	1.56E-05	1.92E-04	2.16E-04	2.13E-04	2.19E-04	6.56E-09	0.00E+00	2.16E-04
•.9 m uniply bar	29.5346	7.94E-06	1.92E-04	4.31E-04	4.27E-04	4.34E-04	2.77E-08	9.99E-05	3.31E-04
*•.9 m uniply bar	29.617	3.77E-06	1.92E-04	2.62E-04	2.57E-04	2.68E-04	1.03E-08	0.00E+00	2.62E-04
*•.9 m uniply bar	29.6208	6.03E-06	1.92E-04	2.58E-04	2.58E-04	2.58E-04	6.68E-08	0.00E+00	2.58E-04
•.9 m uniply bar	29.4784	9.44E-07	1.92E-04	3.89E-04	3.85E-04	3.92E-04	2.13E-08	1.00E-04	2.89E-04
*•.9 m uniply bar	29.5648	4.42E-06	1.92E-04	2.27E-04	2.25E-04	2.30E-04	4.13E-08	0.00E+00	2.27E-04

Summary of Damping From AS4/3501 Graphite/Epoxy Bars
With [±15]6s Layup

All results taken in air with unmodified bending motors except where noted

key:

• = test with modified bending motor

* = test in vacuum

Test Specimen	fn (Hz)	Strain	Average Damping Ratio	Minimum Damping Ratio	Maximum Damping Ratio	Error From Noise	Damping Ratio Due to Air	Avg. Corr. For Air
.9 m 0 CTE bar	91.236	4.20E-06	9.09E-04	8.72E-04	9.27E-04	7.21E-08	5.69E-05	8.52E-04
.9 m 0 CTE bar	90.831	1.86E-06	7.57E-04	7.49E-04	7.60E-04	1.33E-07	5.70E-05	7.00E-04
.9 m 0 CTE bar	90.832	6.20E-08	7.59E-04	7.54E-04	7.60E-04	3.99E-06	5.70E-05	7.02E-04
.9 m 0 CTE bar	90.832	1.96E-08	7.57E-04	7.54E-04	7.60E-04	1.27E-05	5.70E-05	7.00E-04
.9 m 0 CTE bar	90.821	5.46E-09	7.61E-04	7.54E-04	7.65E-04	4.53E-05	5.70E-05	7.04E-04
.9 m 0 CTE bar	90.82	1.84E-09	7.62E-04	7.60E-04	7.65E-04	1.36E-04	5.70E-05	7.05E-04
.9 m 0 CTE bar	90.823	5.87E-10	7.62E-04	7.60E-04	7.71E-04	4.20E-04	5.70E-05	7.05E-04
.9 m 0 CTE bar	287.437	2.00E-07	1.27E-03	1.24E-03	1.32E-03	3.92E-06	3.20E-05	1.24E-03
.9 m 0 CTE bar	287.552	6.33E-08	1.33E-03	1.29E-03	1.38E-03	1.48E-05	3.20E-05	1.30E-03
.9 m 0 CTE bar	287.551	2.85E-08	1.12E-03	1.09E-03	1.16E-03	2.45E-05	3.20E-05	1.09E-03
.9 m 0 CTE bar	287.563	9.52E-09	1.06E-03	1.05E-03	1.07E-03	6.97E-05	3.20E-05	1.03E-03
.9 m 0 CTE bar	287.55	3.08E-09	1.11E-03	1.09E-03	1.12E-03	2.26E-04	3.20E-05	1.08E-03
.9 m 0 CTE bar	287.559	2.79E-07	1.11E-03	1.11E-03	1.11E-03	2.51E-06	3.20E-05	1.08E-03
.9 m 0 CTE bar	287.634	1.01E-06	1.09E-03	1.06E-03	1.10E-03	6.85E-07	3.20E-05	1.06E-03
.9 m 0 CTE bar	287.589	1.01E-05	1.07E-03	1.06E-03	1.08E-03	6.71E-08	3.20E-05	1.04E-03
.9 m 0 CTE bar	287.522	3.17E-05	1.10E-03	1.10E-03	1.10E-03	2.19E-08	3.20E-05	1.07E-03
.9 m 0 CTE bar	287.289	1.62E-04	1.45E-03	1.45E-03	1.46E-03	5.82E-09	3.20E-05	1.42E-03
.9 m 0 CTE bar	33.185	3.63E-06	7.34E-04	7.23E-04	7.53E-04	1.46E-10	9.43E-05	6.40E-04
.9 m 0 CTE bar	33.181	3.67E-07	7.19E-04	7.08E-04	7.23E-04	1.46E-06	9.43E-05	6.25E-04
.9 m 0 CTE bar	33.184	4.03E-08	7.01E-04	6.93E-04	7.08E-04	1.31E-05	9.43E-05	6.07E-04
.7 m 0 CTE bar	53.113	5.76E-06	7.12E-04	6.87E-04	8.00E-04	4.57E-08	7.45E-05	6.37E-04
.7 m 0 CTE bar	53.111	1.84E-06	7.06E-04	7.06E-04	7.06E-04	1.42E-07	7.45E-05	6.31E-04
.7 m 0 CTE bar	53.111	5.80E-07	7.05E-04	6.97E-04	7.06E-04	4.51E-07	7.45E-05	6.30E-04
.7 m 0 CTE bar	53.11	1.93E-07	7.06E-04	7.06E-04	7.06E-04	1.35E-06	7.45E-05	6.31E-04
.7 m 0 CTE bar	53.11	6.16E-08	7.09E-04	7.06E-04	7.16E-04	4.24E-06	7.45E-05	6.34E-04
.7 m 0 CTE bar	53.105	1.71E-08	7.14E-04	7.06E-04	7.25E-04	1.54E-05	7.45E-05	6.39E-04
.7 m 0 CTE bar	53.108	5.49E-09	7.25E-04	7.25E-04	7.25E-04	5.21E-05	7.45E-05	6.50E-04
.7 m 0 CTE bar	53.108	1.96E-09	7.19E-04	6.78E-04	7.53E-04	1.46E-04	7.45E-05	6.44E-04
.7 m 0 CTE bar	145.032	2.70E-08	7.97E-04	7.90E-04	8.03E-04	4.50E-06	4.51E-05	7.52E-04

Test Specimen	fn (Hz)	Strain	Average Damping Ratio	Minimum Damping Ratio	Maximum Damping Ratio	Error From Noise	Damping Ratio Due to Air	Avg. Corr. For Air
.7 m 0 CTE bar	145.058	8.99E-10	7.91E-04	7.86E-04	7.97E-04	1.40E-04	4.51E-05	7.46E-04
.7 m 0 CTE bar	145.038	8.44E-09	7.93E-04	7.90E-04	7.97E-04	1.42E-05	4.51E-05	7.48E-04
.7 m 0 CTE bar	145.045	4.85E-07	7.97E-04	7.97E-04	8.00E-04	2.49E-07	4.51E-05	7.52E-04
.7 m 0 CTE bar	145.043	1.94E-06	7.86E-04	7.86E-04	7.86E-04	6.13E-08	4.51E-05	7.41E-04
.7 m 0 CTE bar	145.042	9.66E-06	7.94E-04	7.90E-04	7.97E-04	1.24E-08	4.51E-05	7.49E-04
.7 m 0 CTE bar	145.034	4.92E-05	7.96E-04	7.93E-04	7.97E-04	2.44E-09	4.51E-05	7.51E-04
.7 m 0 CTE bar	145.03	1.48E-04	8.24E-04	8.21E-04	8.24E-04	8.39E-10	4.51E-05	7.79E-04
•.9 m 0 CTE bar	31.934	4.55E-06	6.90E-04	6.66E-04	7.13E-04	1.42E-07	9.61E-05	5.94E-04
*•.9 m 0 CTE bar	32.013	6.58E-06	5.46E-04	5.44E-04	5.47E-04	7.64E-08	0.00E+00	5.46E-04
*•.9 m 0 CTE bar	32.013	6.31E-05	5.45E-04	5.39E-04	5.55E-04	7.96E-09	0.00E+00	5.45E-04
*•.9 m 0 CTE bar	32.012	2.32E-04	5.63E-04	5.63E-04	5.63E-04	2.23E-09	0.00E+00	5.63E-04
*•.9 m 0 CTE bar	32.0085	6.99E-04	5.92E-04	5.86E-04	6.02E-04	7.80E-10	0.00E+00	5.92E-04
*•.9 m 0 CTE bar	32.001	1.49E-03	6.60E-04	6.56E-04	6.72E-04	4.17E-10	0.00E+00	6.60E-04
*•.9 m 0 CTE bar	32.013	6.94E-07	5.37E-04	5.31E-04	5.39E-04	7.14E-10	0.00E+00	5.37E-04
•.9 m 0 CTE bar	31.88	3.33E-06	8.04E-04	8.00E-04	8.15E-04	2.12E-07	9.62E-05	7.08E-04
•.9 m 0 CTE bar	31.888	1.24E-06	7.37E-04	7.37E-04	7.37E-04	5.50E-07	9.62E-05	6.41E-04

Summary of Damping From AS4/3501 Graphite/Epoxy Tubes With [±15]3s Layup

All results taken in air with unmodified bending motors except where noted

key:

• = test with modified bending motor

* = test in vacuum

Test Specimen	fn (Hz)	Strain	Average Damping Ratio	Minimum Damping Ratio	Maximum Damping Ratio	Error From Noise	Damping Ratio Due to Air	Avg. Corr. For Air
.9 m Gr/Ep tube	274.86	8.06E-08	2.89E-03	2.87E-03	2.91E-03	6.10E-09	3.04E-05	2.86E-03
.9 m Gr/Ep tube	274.9	1.63E-08	2.86E-03	2.84E-03	2.87E-03	6.04E-09	3.04E-05	2.83E-03
.9 m Gr/Ep tube	274.93	4.20E-09	2.86E-03	2.84E-03	2.87E-03	6.04E-09	3.04E-05	2.83E-03
.9 m Gr/Ep tube	274.81	1.94E-06	3.00E-03	2.98E-03	3.00E-03	6.34E-09	3.04E-05	2.97E-03
.9 m Gr/Ep tube	274.62	8.17E-06	4.23E-03	4.22E-03	4.24E-03	8.96E-09	3.04E-05	4.20E-03
.9 m Gr/Ep tube	272.98	3.08E-05	9.24E-03	9.15E-03	9.33E-03	1.98E-08	3.05E-05	9.21E-03
.9 m Gr/Ep tube	272.2	4.64E-05	1.47E-02	1.48E-02	1.49E-02	3.18E-08	3.06E-05	1.47E-02
.9 m Gr/Ep tube	272.74	8.23E-07	3.19E-03	3.13E-03	3.29E-03	6.00E-09	3.05E-05	3.16E-03
.7 m Gr/Ep tube	502.97	3.17E-07	1.31E-03	1.30E-03	1.31E-03	8.25E-10	2.25E-05	1.29E-03
.7 m Gr/Ep tube	502.96	6.39E-08	1.30E-03	1.30E-03	1.31E-03	8.19E-10	2.25E-05	1.28E-03
.7 m Gr/Ep tube	502.95	1.28E-08	1.26E-03	1.25E-03	1.28E-03	7.94E-10	2.25E-05	1.24E-03
.7 m Gr/Ep tube	502.94	3.76E-09	1.31E-03	1.29E-03	1.32E-03	8.25E-10	2.25E-05	1.29E-03
.7 m Gr/Ep tube	502.93	1.87E-06	1.30E-03	1.29E-03	1.30E-03	8.17E-10	2.25E-05	1.28E-03
.7 m Gr/Ep tube	502.87	9.58E-06	1.31E-03	1.30E-03	1.32E-03	8.23E-10	2.25E-05	1.29E-03
.7 m Gr/Ep tube	502.68	4.03E-05	1.48E-03	1.46E-03	1.49E-03	9.33E-10	2.25E-05	1.46E-03
.7 m Gr/Ep tube	502.42	8.82E-05	1.61E-03	1.60E-03	1.63E-03	1.02E-09	2.25E-05	1.59E-03
•.7 m Gr/Ep tube	499.52	1.08E-06	9.85E-04	9.85E-04	9.85E-04	6.29E-10	2.26E-05	9.62E-04
*•.7 m Gr/Ep tube	500.77	4.65E-07	9.58E-04	9.53E-04	9.63E-04	6.09E-10	0.00E+00	9.58E-04
*•.7 m Gr/Ep tube	500.78	2.39E-06	9.57E-04	9.53E-04	9.63E-04	6.08E-10	0.00E+00	9.57E-04
*•.7 m Gr/Ep tube	500.76	2.31E-05	9.54E-04	9.53E-04	9.58E-04	6.06E-10	0.00E+00	9.54E-04
*•.7 m Gr/Ep tube	500.73	1.06E-04	9.82E-04	9.78E-04	9.83E-04	6.24E-10	0.00E+00	9.82E-04
*•.7 m Gr/Ep tube	500.63	3.16E-04	1.04E-03	1.04E-03	1.04E-03	6.61E-10	0.00E+00	1.04E-03
*•.7 m Gr/Ep tube	500.55	5.96E-04	1.10E-03	1.10E-03	1.11E-03	6.99E-10	0.00E+00	1.10E-03
*•.7 m Gr/Ep tube	500.74	7.40E-09	9.73E-04	9.73E-04	9.73E-04	6.18E-10	0.00E+00	9.73E-04

Summary of Damping From Interferometer Testbed
All results using bending motor actuator except where noted
key:
• = test using DC motor
† = test using bending motor with DC motor still attached

Test Specimen	fn (Hz)	Strain	Average Damping Ratio	Minimum Damping Ratio	Maximum Damping Ratio	Error From Noise
testbed	44.118	9.26E-07	5.86E-04	5.78E-04	6.01E-04	2.03E-07
testbed	44.121	1.57E-07	5.77E-03	5.66E-04	5.77E-04	4.79E-06
testbed	44.126	3.01E-08	5.77E-04	5.66E-04	5.77E-04	6.30E-06
testbed	44.125	5.27E-09	5.63E-04	5.55E-04	5.66E-04	3.42E-05
testbed	44.125	1.29E-09	5.75E-04	5.66E-04	5.75E-04	1.39E-04
•testbed	43.87	5.32E-07	6.42E-04	6.26E-04	6.42E-04	1.66E-04
•testbed	43.87	1.79E-06	6.75E-04	6.61E-04	6.75E-04	1.20E-07
•testbed	43.858	7.01E-06	7.25E-04	6.83E-04	7.25E-04	2.96E-08
•testbed	43.834	2.60E-05	7.69E-04	7.31E-04	7.69E-04	9.06E-09
testbed	39.999	1.79E-06	7.12E-04	7.00E-04	7.18E-04	1.27E-07
testbed	40.003	3.12E-07	7.10E-04	7.06E-04	7.18E-04	7.37E-07
testbed	40.004	6.15E-08	7.10E-04	7.06E-04	7.12E-04	3.72E-06
testbed	40.004	2.54E-07	7.31E-04	7.31E-04	7.31E-04	9.33E-07
testbed	40.005	1.07E-08	7.00E-04	6.65E-04	7.00E-04	2.11E-05
testbed	40.008	2.60E-07	7.41E-04	7.31E-04	7.44E-04	9.27E-07
testbed	40.008	2.02E-09	7.09E-04	7.00E-04	7.13E-04	1.39E-04
•testbed	38.876	1.39E-06	8.81E-04	8.74E-04	8.87E-04	2.07E-07
•testbed	38.882	2.75E-07	8.65E-04	8.48E-04	8.74E-04	1.04E-06
•testbed	38.858	6.56E-06	8.79E-04	8.74E-04	8.88E-04	4.18E-08
•testbed	38.798	2.60E-05	1.06E-03	1.03E-03	1.07E-03	9.35E-09
•testbed	38.763	1.02E-04	1.07E-03	1.03E-03	1.10E-03	3.45E-09
†testbed	38.85	3.60E-08	1.14E-03	1.12E-03	1.15E-03	9.95E-06
†testbed	38.83	2.60E-07	1.05E-03	1.04E-03	1.06E-03	1.29E-06
testbed	55.398	2.50E-06	6.65E-04	6.63E-04	6.72E-04	8.57E-08
testbed	55.403	9.31E-07	6.55E-04	6.54E-04	6.59E-04	2.29E-07
testbed	55.408	2.14E-07	6.43E-04	6.41E-04	6.50E-04	9.86E-07
testbed	55.408	5.25E-08	6.41E-04	6.41E-04	6.41E-04	3.98E-06
testbed	55.41	1.31E-08	6.42E-04	6.36E-04	6.45E-04	1.63E-05
testbed	55.411	2.62E-09	6.49E-04	6.32E-04	6.77E-04	8.10E-05
•testbed	54.446	3.81E-07	1.03E-03	1.02E-03	1.04E-03	8.66E-05

Test Specimen	fn (Hz)	Strain	Average Damping Ratio	Minimum Damping Ratio	Maximum Damping Ratio	Error From Noise
•testbed	54.406	2.03E-06	9.95E-04	9.56E-04	1.03E-03	1.40E-07
•testbed	54.374	1.09E-05	1.01E-03	1.00E-03	1.03E-03	2.83E-08
•testbed	54.3	3.67E-05	1.24E-03	1.11E-03	1.32E-03	1.29E-08
†testbed	54.402	2.10E-07	1.10E-03	1.08E-03	1.12E-03	1.66E-06
†testbed	54.468	2.84E-08	9.75E-04	9.64E-04	9.91E-04	1.05E-05

APPENDIX 2

DERIVATION OF VISCOUS DAMPING ON AN OSCILLATING RECTANGULAR BAR

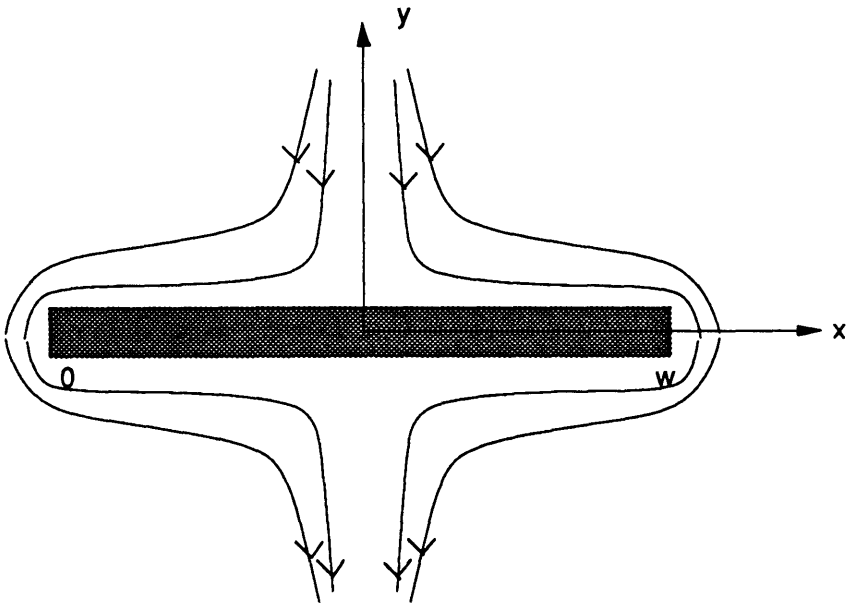

Figure A2.1 - Flow Around An Oscillating Bar

One of the major external factors affecting the measurement of the damping of oscillating bar in air, shown in Figure A2.1, is the damping due to friction in the viscous damping layer. In this section, the expression describing the viscous damping on an oscillating bar with a rectangular cross section is derived. This derivation is based on the formulation presented by Batchelor, in Section 5.13 of An Introduction to Fluid Dynamics, [Batchelor, 1977] of the damping on an oscillating cylinder. The solution assumes that there is no mean flow imposed on the fluid, that the vorticity is zero, that there is no separation of the flow, that the thickness of the boundary layer, δ is much smaller than the length of the bar, and on the order of,

$$\delta = \sqrt{\frac{2\nu}{\omega}} \qquad [A2.1]$$

where ν is the kinematic viscosity of the fluid, and ω is the frequency of vibration [Batchelor, 1977] . This expression for δ comes from the solution of flow in an oscillating boundary layer. In the derivation of the damping force on an oscillating cylinder, Batchelor finds that the average rate of dissipation caused by the boundary layer per unit area is given by,

$$\int_0^{\infty} \frac{\mu U^2}{\delta^2} e^{-2y/\delta} dy = \frac{\mu U^2}{2\delta} \qquad [A2.2]$$

where μ is the viscosity, U is the relative velocity of the fluid in the boundary layer, and y is the distance normal to the boundary. To find the rate of dissipation for the entire body per unit length, Equation A2.2 can be integrated over the surface. This rate of dissipation is equal to the rate of work that the bar has to do against the viscous force, F, which is $1/2U_0F$ where U_0 is the maximum velocity over one cycle. Equating the work done by the bar with the rate of dissipation gives,

$$\frac{1}{2}U_oF = \frac{\mu}{2\delta}\int U^2 ds \qquad [A2.2]$$

To find the damping force, the expression for the relative flow velocity in the boundary layer is needed. The velocity in the boundary layer can be approximated by the solution for an elliptical cross section described by,

$$\frac{x^2}{a^2} + \frac{y^2}{b^2} = 1$$

where a is half the width, w/2 and b is half the thickness, t/2. Assuming that the velocity in the boundary normal to the bar is zero, the expression for the velocity is given by,

$$|U| = \frac{U_o(a+b)\sin(\upsilon+\alpha)}{\sqrt{a^2\sin^2\upsilon + b^2\cos^2\upsilon}} \qquad [A2.3]$$

where $x=a\cos\upsilon$ and υ goes from 0 at $x = 0$ to $\upsilon = \pi$ at $x = w$, and α is the angle of attack of the bar. For a flat plate approximated with an elliptic cross section with no thickness (b=0) and $\alpha = \pi/2$, Equation A2.3 gives an infinite $|U|$ at the edges, thus causing the need for finite thickness in the elliptical approximation. Substituting Equation A2.3 into A2.2 and integrating over the surface gives,

$$\frac{1}{2}U_oF = \frac{\mu}{2\delta}\int \frac{U_o^2(a+b)^2\sin^2(\upsilon+\alpha)}{a^2\sin^2\upsilon + b^2\cos^2\upsilon} dx \qquad [A2.4]$$

Assuming $\alpha = \pi/2$, $\sin(\upsilon + \alpha) = \cos\upsilon$. Substituting this into A2.4, gives,

$$\frac{1}{2}U_oF = \frac{\mu U_o^2(a+b)^2}{2\delta}\int \frac{\cos^2\upsilon}{a^2\sin^2\upsilon + b^2\cos^2\upsilon} dx \qquad [A2.5]$$

Using the parametric substitution, x = acosυ, Equation A2.5 can be expressed in terms of υ only -- dx = -asinυdυ. The velocity in the boundary layer, as described by A2.3, is symmetric on all four portions of the bar. Assuming that the friction at the edges is much smaller than the friction over the top and bottom surfaces, the plate can be split into four parts (Fig. A2.2). To simplify the integration in A2.5, symmetry can be used. Integrating Equation A2.5 over region 1, and multiplying by four to obtain the force over the entire bar,

$$\frac{1}{2}U_oF = \frac{-4\mu U_o^2(a+b)^2}{2\delta}\int_0^{\pi/2}\frac{\cos^2\upsilon\sin\upsilon}{a^2\sin^2\upsilon + b^2\cos^2\upsilon}d\upsilon \qquad [A2.6]$$

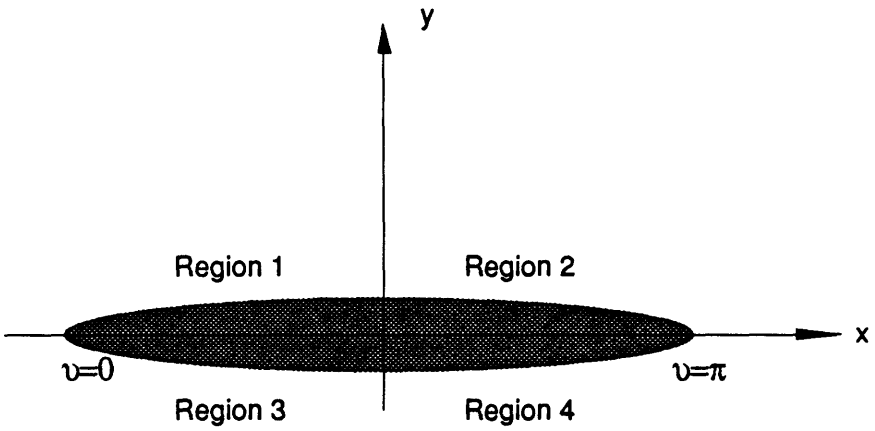

Figure A2.2 Division of the Surface of the Elliptical Approximation of the Bar into Four Regions

Substituting the dimensions of the bar, a=12.7 mm, b=1.6 mm, and integrating Equation A2.6 numerically gives,

$$\frac{1}{2}U_oF = -\frac{0.058\mu U_o^2}{\delta} \qquad [A2.7]$$

which gives the rate of energy dissipation.

To find the equivalent viscous damping, the expression,

$$\zeta = \frac{\Delta E}{4\pi E} \qquad [A2.8]$$

can be used where ΔE is the energy dissipated per cycle and E is the average energy of the bar [Blevins, 1977]. ΔE per unit length can be found by integrating Equation A2.7 over one cycle,

$$\Delta E = \int_0^T \frac{1}{2}U_0F dt = \frac{0.058\mu U_o^2 T}{\delta}$$

where T is the period of oscillation. Using $T=2\pi/\omega$, this expression can be written as,

$$\Delta E = \frac{0.116\mu U_o^2}{\delta\omega} \qquad \text{[A2.9]}$$

The average total energy per length of the oscillating bar is given by,

$$E = \frac{1}{2} A\rho_s U_o^2 \qquad \text{[A2.10]}$$

where A is the cross sectional area of the bar, A=wt, and ρ_S is the density of the bar. Substituting Equations A2.9 and A2.10 into A2.8, gives a damping ratio for the rectangular bars, which can be written in the form,

$$\zeta = 9.13\left(\frac{\rho}{\rho_s}\right)\sqrt{\frac{2\nu}{\omega w^2}} \qquad \text{[A2.11]}$$

using the substitution for the viscosity $\mu=\rho\nu$ and the expression for the thickness of the boundary layer, Equation A2.1. So, the damping is independent of the amplitude of vibration of the bar, and depends only on the frequency and the material properties of the fluid and bar.

The expression for the viscous damping on a bar can be compared with the equivalent expression for the viscous damping on a tube [Batchelor, 1977],

$$\zeta = 2\left(\frac{\rho}{\rho_s}\right)\sqrt{\frac{2\nu}{\omega D^2}} \qquad \text{[A2.12]}$$

where D is the diameter of the tube. As expected, the viscous damping on a bar is greater than the damping of a tube.

APPENDIX 3

CALCULATION OF UNCERTAINTY IN DAMPING DUE TO MEASUREMENT NOISE

The damping ratio, ζ for a system can be calculated using,

$$\zeta = \frac{\Delta\omega}{2\omega_n} = \frac{\omega_2 - \omega_1}{2\omega_n} \qquad [A3.1]$$

where ω_1 and ω_2 are the frequencies of the two half-power points and ω_n is the resonant frequency of the mode of interest. An uncertainty in the amplitude measurements used to find the half power points causes an error in frequency which, as can be seen in Equation A3.1, causes an uncertainty in damping. Assuming that these uncertainties in frequency are independent and random, the uncertainty in damping [Taylor, 1982] is given by,

$$\delta\zeta = \frac{\sqrt{\delta\omega_1^2 + \delta\omega_2^2}}{2\omega_n} \qquad [A3.2]$$

where $\delta\omega_1$ and $\delta\omega_2$ are the derived uncertainties in frequencies of the half power points and $\delta\zeta$ is the uncertainty in the damping ratio. To find the uncertainty in the frequency of each half-power point, the relationship between the measured amplitudes and frequencies is needed. For a second order system with harmonic excitation of the form,

$$\ddot{x} + 2\zeta\omega_n\dot{x} + \omega_n^2 x = \omega_n^2 A\cos\omega t$$

where x is the response, and A is the magnitude of the excitation, this relationship is given by,

$$x = \frac{A}{\sqrt{\left[1 - \left(\frac{\omega}{\omega_n}\right)^2\right]^2 + \left(\frac{2\zeta\omega}{\omega_n}\right)^2}} \qquad [A3.3]$$

where ω is the frequency of excitation. An error in ω depends on the slope of the response curve given in Equation A3.3. An error in x, δx, for a lightly damped system with a narrow, sharp response peak causes a small error in frequency. To find slope of the response curve, Equation A3.3 can be differentiated to get,

$$\frac{\partial x}{\partial \omega} = -\frac{2A\left[-\left[1-\left(\frac{\omega}{\omega_n}\right)^2\right]\left(\frac{\omega}{\omega_n}\right)+\left(2\zeta^2\omega\right)\right]}{\left[\left[1-\left(\frac{\omega}{\omega_n}\right)^2\right]^2+\left(\frac{2\zeta\omega}{\omega_n}\right)^2\right]^{3/2}}$$

which shows that the slope decreases with increasing damping. From this expression, the error in frequency due to an error in measured response, δx, can be found to be,

$$\delta\omega = \delta x \frac{-\left[\left[1-\left(\frac{\omega}{\omega_n}\right)^2\right]^2+\left(\frac{2\zeta\omega}{\omega_n}\right)^2\right]^{3/2}}{2A\left[-\left[1-\left(\frac{\omega}{\omega_n}\right)^2\right]\left(\frac{\omega}{\omega_n}\right)+\left(2\zeta^2\omega\right)\right]} \qquad \text{[A3.4].}$$

The uncertainty in frequency, $\delta\omega$ can found by substituting the measured damping ratio and frequencies into Equation A3.4. In turn, the uncertainty in damping ratio, $\delta\zeta$, can be found by substituting $\delta\omega_1$ and $\delta\omega_2$ into Equation A3.2.

APPENDIX 4

CONSTANTS USED IN MODELS OF DAMPING

In Chapter 4, theoretical models of the damping of the aluminum bars and the uniply Gr/Ep bars were given. The constants used in each of these models are presented below [Roylance et al, 1983], [Ralls et al, 1976], [Tsai and Hahn, 1980], [U.S. DOD, 1976].

Equation 4.4

$$\zeta = \frac{\alpha^2 E T}{2C\rho}\left[\frac{\omega\tau}{1+\omega^2\tau^2}\right],$$

$$\frac{1}{\omega_r} = \tau = \frac{h^2 C}{\pi^2 k}$$

Quantity	Symbol	Value for 6061-T6 Aluminum
Coefficient of Thermal Expansion	α	23.261×10^{-6} °K^{-1}
Modulus of Elasticity	E	6.83×10^{10} Pa
Specific Heat Per Mass	C	962.96 J/kg°K
Mass Density	ρ	2712.6 kg/m^3
Thermal Conductivity	k	166.15 W/m°K

Equation 4.5

$$\zeta = \frac{4}{\pi}\frac{n_d bL}{F^2}\varepsilon,$$

$$F = \left[c\sqrt{1-c}\left(|A|(1+|Q|)/32\pi\right)\right]$$

Quantity	Symbol	Value for 6061-T6 Aluminum
Burger's Vector	b	2.86×10^{-7} mm
Dislocation Segment	L	3×10^{-2} mm
Solute Concentration	c	2%
Strength of Solute Atoms	$\|A\|(1+\|Q\|)$	1.61

Equations 4.7 - 4.8

$$\zeta_A = \frac{\zeta_m}{\frac{E_f V_f}{E_m V_m} + 1}$$

$$\zeta_S = \frac{\zeta_{12}\int_0^{1/2}\left[\frac{\partial^3 w}{\partial x^3}\right]^2 dx}{\int_0^{1/2}\left[\frac{\partial^3 w}{\partial x^3}\right]^2 dx + \frac{10G_{12}}{E_m h^2}\int_0^{1/2}\left[\frac{\partial^2 w}{\partial x^2}\right]^2 dx}$$

Quantity	Symbol	Value for AS4/3501 Gr/Ep
Modulus of Elasticity of Fiber	E_f	2.34 x 1011 Pa
Fiber Volume Fraction	Vf	0.6
Modulus of Elasticity of Matrix	E_m	1.4 x 108 Pa
Damping Ratio of Matrix	ζ_m	0.35
Matrix Volume Fraction	V_m	0.4
Shear Modulus	G_{12}	6×10^9 Pa